Structural characterisation of the prokaryotic sodium channel C-terminal domain

Structural Characterisation of the Prokaryotic Sodium Channel C-Terminal Domain

PhD Thesis

Wayne Miller

`

Declaration of Authenticity of Work

The work herein presented is the work of candidate, except where otherwise specified.

Signed

`

Abstract

Since the discovery of the first prokaryotic voltage gated sodium channel (Nav) in 2001, prokaryotic Navs have been a high priority target for structural study. Prokaryotic Navs are of interest as a model system due to their homology to eukaryotic Navs, which are high value drug development targets for their roles in pain perception and neural function. While prokaryotic Navs have function and pharmacology distinct from their eukaryotic homologues, understanding their structure holds implications for drug development and for understanding diseases stemming from neuronal dysfunction. However, Navs have historically been challenging targets for structural study, resisting attempts at crystallisation until recently. In this study, expression, purification, and characterisation of a chimera of the NavBh channel and the ligand gating RCK domain from the prokaryotic potassium channel MthK has been performed. It was hypothesised that the addition of the RCK domain would improve the channel's crystallisation potential, and create a ligand gated Nav for functional characterisation. Electrophysiological studies demonstrated that the RCK domain was capable of gating NavBh, however the chimera had reduced solubility, indicating that this chimeric fusion was not an ideal target for structural study due to low purification yields.

Following this, and in light of recent studies that suggested the structure of the prokaryotic Nav C-terminus had a role in channel function, structural analysis of the C-terminus of a prokaryotic Nav homologue cloned from *Bacillus alcalophilus* has been performed. Synchrotron radiation circular dichroism analysis of serial C-terminal truncations demonstrated the structure of the NsvBa C-terminus consists of a helical region connected to the channel pore by a disordered neck region, despite conflicting bioinformatics predictions. This offers further support for the hypothesis that in functional Navs, the C-terminus consists of a disordered neck region connecting a coiled-coil to the base of the pore, which acts as a spring to assist in channel gating and inactivation.

`

Acknowledgements

I would like to thank Dr Andreas O'Reilly for initial design of the NavBh-RCK construct. Dr Andrew Miles and Dr Jose Luis-Lopez for performing the SRCD measurements, and help with analysis. Dr Claire Bagnéris, who provided primers for the truncations of NsvBa. Dr Andrew Powl, for help with protein purification and electrophysiology.

Our collaborators at the University of Southampton who worked with us on the electrophysiology, Dr Hywel Morgan, Dr Maurits de Planque, Dr Shimul Saha, and Dr Sumit Kalsi.

Our collaborators at University College London who performed the measurements and analysis for the CW-EPR and DEER-EPR spectroscopy Dr Chris Kay, and Dr Enrico Salvadori.

Dr Mat Jennions, for setting up and monitoring the LCP crystallisation trials at the Membrane Protein Laboratory, at the Diamond Synchrotron facility.

Dr Paul DeCaen of Harvard, for providing the original NsvBa construct.

Professor Bonnie Wallace, for her guidance and supervision.

`

Table of Contents

Declaration of Authenticity of Work 2
Abstract 3
Acknowledgements 4
List of Figures 8
List of Tables 10
List of Abbreviations 11
Chapter 1: Introduction to Voltage Gated Sodium Channels 12
1.1 Early Structural Work 13
1.2 Function and Dysfunction of Eukaryotic Navs 16
Overview of the Action Potential 16
Muscle Navs 17
Pain Perception Navs 17
Neuronal Navs 18
Nav Modulators 19
1.3 Introduction to Prokaryotic Navs 21
1.4 Crystal Structures of Prokaryotic Navs 22
Structural Overview 22
General Structural Features 24
The Voltage Sensor 25
The Selectivity Filter 26
The C-Terminus 27
Fenestrations 28
1.5 Electrophysiology of Prokaryotic Navs 29
1.6 Previous Work with NavBh 30
1.7 Introduction to MthK 31
1.8 The Chimeric Fusion Construct NavBh-RCK 33
1.9 Introduction to NsvBa 35
Investigation of the NsvBa C-Terminus 35
1.10 Aims and Objectives 36
Aims 36
Objectives 37
Chapter 2: Review of Techniques 39
2.1 Methods for the Recombinant Expression and Purification of Membrane Proteins from Bacterial Cell Culture 39
Cloning 39
Expression 40

`

Cell Disruption and Membrane Isolation....43
Membrane Solubilisation....43
Affinity Chromatography....44
Size Exclusion Chromatography....46
2.2 Methods for the Assay of Voltage Gated Ion Channel Functionality....47
Introduction....47
Electrophysiology....47
Ion Conductance Microscopy....57
Ion Flux and Voltage Measurement Methods....57
2.3 Circular Dichroism and Synchrotron Radiation Circular Dichroism....58
2.4 Electron Paramagnetic Resonance Spectroscopy....60
Chapter 3: Methods and Materials....63
3.1 Cloning....63
3.2 Polymerase Chain Reaction Overlap Extension Cloning and Mutagenesis....63
3.3 Expression, Cell Disruption, and Membrane Harvesting....64
3.4 Membrane Solubilisation and Purification....64
3.5 Sodium Dodecyl Sulphate Poly-Acrylamide Gel Electrophoresis and Western Blotting....65
3.6 Gluteraldehyde Crosslinking....65
3.7 Synchrotron Radiation Circular Dichroism Spectroscopy....66
3.8 Bioinformatics and Modelling....66
3.9 Electrophysiology....67
3.10 Proteoliposome Reconstitution of NavBh-RCK....68
3.11 Continuous Wavelength and Double Electron-Electron Resonance Electron Paramagnetic Resonance Spectroscopy....68
3.12 Crystallisation Trials....69
Chapter 4: Investigation of the NavBh-RCK Chimeric Construct....70
4.1 Overview....70
4.2 Expression and Purification of NavBh-RCK....70
Initial Expression Trials....70
Expression and Purification of NavBh-RCK M107I....73
Optimisation of NavBh-RCK and NavBh-RCK M107I Purification....74
4.3 SRCD Spectroscopy of NavBh-RCK....79
4.4 Crystallisation Trials of Low-Concentration NavBh-RCK and NavBh-RCK M107I..83
4.5 Electrophysiology of NavBh-RCK....83
4.6 Expression and Purification of NavBh128-RCK....85
Structural Alignment of NavBh128-RCK and MthK....87

`

Expression and Purification of NavBh128-RCK 87
4.7 Electrophysiology of NavBh128RCK 88
4.8 Co-Expression of NavBh128-RCK Constructs With the Soluble RCK Domain 90
4.9 Electrophysiology of NavBh128-RCK M107I Co-expressed With the Soluble RCK Domain 92
4.10 NsvBa-RCK and NavMs-RCK 92
4.11 Modelling of the Nav-RCK Linker Region 93
4.12 Conclusions 96
Chapter 5: Structural Investigation of NsvBa 98
5.1 Overview 98
5.2 Expression and Purification of NsvBa 99
5.3 *In Silico* Investigations of NsvBa C-Terminal Structure 99
5.4 Homology Modelling of the NsvBa C-Terminus 100
5.5 Expression and Purification of NsvBa C-Terminal Truncations 101
5.6 SRCD Spectroscopy of NsvBa C-Terminal Truncations 105
5.7 EPR Spectroscopy of the NsvBa C-Terminus 106
5.8 Introduction of the DDT Binding Site to NsvBa 109
5.9 NsvBa Crystallisation Trials 112
5.10 Conclusions 112
Chapter 6: Discussion and Future Work 113
6.1 Purification and Solubility of NavBh-RCK Constructs 113
6.2 Electrophysiology of NavBh-RCK 113
6.3 Homology Modelling of an Open and Closed Nav-RCK 115
6.4 Expression and Purification of NsvBa 118
6.5 SRCD Spectroscopic Analyses of the NsvBa C-Terminus 119
6.6 EPR Spectroscopic Studies of the NsvBa C-Terminus 120
6.7 Introduction of DDT Binding Site into NsvBa 121
6.8 Future Work 122
Further Investigations of the NavBh-RCK Fusion Chimera 122
Further Investigations of NsvBa 123
Appendix 125
References 135

`

List of Figures

Figure 1: Eukaryotic and Prokaryotic Nav Topology. 12
Figure 2: Phylogeny of Prokaryotic Navs. 21
Figure 3: Models of Nav Structures. 23
Figure 4: Comparison of Open and Closed Nav Pores. 24
Figure 5: Structures of the Nav Voltage Sensor and Pore. 26
Figure 6: Structure of the Nav C-Terminus. 27
Figure 7: Electrophysiology of the NavBh Pore in a Synthetic Lipid Bilayer. 30
Figure 8: Crystal Structures of MthK. 32
Figure 9: Diagrammatic Representation of Wild Type MthK and NavBh, and of the Chimeric Fusion Construct NavBh-RCK. 34
Figure 10: Diagrammatic Representations of MthK RCK Domain Oligomerisation. 35
Figure 11: Flowchart Diagram for Setup of the Four Primary Types of Patch Clamp Recording Configurations. 50
Figure 12: Diagram of the Methods for the Formation of Planar Lipid Bilayers Within Apertures 53
Figure 13: Example CD Reference Spectra. 59
Figure 14: Diagrammatic Representation and Alignment of NavBh-RCK Constructs. 71
Figure 15: Expression Trials of NavBh-RCK Constructs. 72
Figure 16: Comparison of Nickel IMAC Purification of N- and C-Terminal Hexahistidine Tagged NavBh-RCK. 73
Figure 17: NavAb-RCK Model 74
Figure 18: SDS-PAGE and Western Block of IMAC Purification of NavBh-RCK. 75
Figure 19: Comparison of NavBh-RCK Gel Filtration With and Without $CaCl_2$. 76
Figure 20: Gel Filtration of Ni IMAC Purified and Concentrated NavBh-RCK M107I 77
Figure 21: Comparison of NavBh-RCK Gel Filtration With and Without $CaCl_2$. 78
Figure 22 : SRCD Analysis of NavBh-RCK and NavBh-RCK M107I in the Presence of $CaCl_2$ and EDTA. 80
Figure 23: Gel Filtration of Ni IMAC Purified and Concentrated NavBh-RCK M107I 81
Figure 24: Thermal Denaturation SRCD of NavBh-RCK M107I in the Presence and Absence of $CaCl_2$. 82
Figure 25: Electrophysiology of NavBh-RCK in a Synthetic Lipid Bilayer. 84
Figure 26: Sequence Alignment of MthK and NavBh. 85
Figure 27: Mthk and NavMs Pore Structural Alignment, and NavMs-RCK Model. 86
Figure 28: Gel Filtration of NavBh128-RCK. 88
Figure 29: Electrophysiology of NavBh128-RCKK in a Synthetic Lipid Bilayer. 89
Figure 30: Purification of NavBh128-RCK M107I Co-Expressed With Soluble RCK. 90
Figure 31: Electrophysiology of NavBh128-RCK M107I Co-Expressed With Soluble RCK. 91
Figure 32: Expression Trials of NsvBa-RCK and NavMs-RCK. 92
Figure 33: RCK Gating Ring Structures With the Pore-RCK Linker Resolved. 94
Figure 34: Homology Modelling of the Pore-RCK Linker Region in Nav-RCK Models. 95
Figure 35: *Ab Initio* Modelling of Residues Not Resolved By Homology Modelling of the Pore-RCK Linker Region in Nav-RCK Models. 96
Figure 36: Alignment NsvBa with structurally characterised C-termini. 98
Figure 37: Gel Filtration of IMAC purified NsvBa. 99
Figure 38: Predictions for Secondary Structure of the NsvBa C-Terminus. 100
Figure 39: Homology Models of the NsvBa C-Terminus. 101

`

Figure 40: Diagram, Expression and Gel Filtration of NsvBa C-Terminal Truncations..102
Figure 41: Investigation of NsvBa Aggregation.....103
Figure 42: SRCD Analysis of NsvBa Truncations.....104
Figure 43: Thermal Unfolding SRCD Spectroscopic Analyses of NsvBa 138 C-Terminal Truncations.....105
Figure 44: Expression and Purification of NsvBa Cysteine Mutants for DEER-EPR. 106
Figure 45: EPR Spectroscopy of NsvBa265 229C. 108
Figure 46: Mutagenesis of WT NsvBa, and NsvBa138-265.....110
Figure 47: SRCD of NsvBa138-265 DDT S5/S6, With and Without DDT.....111
Figure 48: Superdex 200 10/300, Gel Filtration Calibration. 128
Figure 49: High Tension Measurements of NavBh-RCK M107I Thermal Unfolding experiments. 131
Figure 50: Mass Spectrometry of the NsvBa265 Pore.....132

`

List of Tables

Table 1: Amino Acid Sequences of the Chimeric Nav-RCK Constructs. 125
Table 2: List of Constructs and Primers. 127
Table 3: Conditions Screened for NavBh-RCK Spin Column Concentration. 129
Table 4: Conditions Screened for Concentration Attempts of NavBh-RCK Constructs.129
Table 5: Crystallisation Screening of NavBh-RCK M107I and NavBh128-RCK M107I...130
Table 6: List of Crystallisation Trials for NsvBa Constructs. 134

`

List of Abbreviations

BLM	black lipid membranes
Cav	voltage gated calcium channel
CD	circular dichroism
CW-EPR	continuous wavelength electron paramagnetic resonance
DDM	n-dodecyl β-d-maltoside
DDT	dichlorodiphenyltrichloroethane
DEER-EPR	double electron-electron resonance – electron paramagnetic resonance
DM	dodecyl maltoside
DTT	dithiothreitol
EDTA	ethylenediaminetetraacetic acid
FPLC	fast protein liquid chromatography
IEC	ion exchange chromatography
IMAC	immobilised metal affinity chromatography
KcsA	Potassium channel cloned from *Streptomyces lividans*
Kv	voltage gated potassium channel
LCP	lipid cubic phase
LDAO	lauryldimethylamine-oxide
MthK	Potassium channel cloned from *Methanobacterium thermoautotrophicum*
Nav	voltage gated sodium channel
NavAb	Nav cloned from *Arcobacter butzleri*
NavAe	Nav cloned from *Alkalilimnicola ehrlichei*
NavBh	Nav cloned from *Bacillus halodurans*
NavCt	Nav cloned from *Caldalkalalibacillus thermarum*
NavMs	Nav cloned from *Magnetococcus* sp.(strain MC-1)
NavRh	Nav cloned from *alphaproteobacterium Rickettsiales* sp *HIMB114*
NsvBa	Non-selective voltage gated channel, cloned from *Bacillus alcalophilus*
OE-PCR	polymerase chain reaction overlap extension cloning
pI	isoelectric point
PE	1-palmitoyl-2-oleoyl-sn-glycero-3-phosphoethanolamine
PG	1-palmitoyl-2-oleoyl-sn-glycero-3-phospho-(1'-rac-glycerol)
RCK	regulator of conductance of potassium
SDS-PAGE	sodium dodecyl sulphate poly-acrylamide gel electrophoresis
SEC	size exclusion chromatography
SRCD	synchrotron radiation circular dichroism
TRIS	tris(hydroxymethyl)aminomethane
WT	wild type

`

Chapter 1: Introduction to Voltage Gated Sodium Channels

Voltage gated sodium channels (Navs) and other voltage gated ion channels are a sub-family of the larger tetrameric ion channel super-family, which includes voltage gated calcium and potassium channels (Cavs and Kvs), TRP channels, and cyclic nucleotide-gated channels (Koishi et al. 2004). Each subunit (or subdomain) of the tetramer is composed of six transmembrane helices denoted S1-S6, with the S5-S6 helices forming the pore, and the S1-S4 helices composing a peripheral voltage sensor (Figure 1). Eukaryotic Navs and Cavs have a pseudotetrameric structure, in which the channel protein is composed of a single approximately 260 kDa α subunit with four homologous subdomains, whereas their prokaryotic homologues consist of a homotetramer.

In eukaryotes the α subunits can associate with one or more β subunits, accessory proteins which modulate but are not required for channel activity. Mammalian β subunits are type one transmembrane proteins which associate

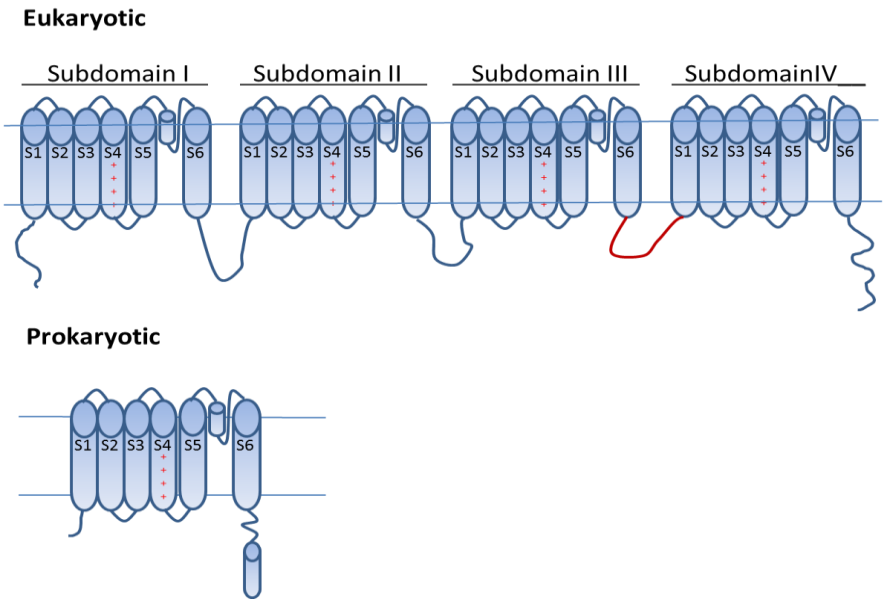

Figure 1: Eukaryotic and Prokaryotic Nav Topology.
Pseudotetrameric 24 transmembrane helix eukaryotic Nav (top) and homotetrameric six transmembrane helix prokaryotic Nav (bottom). Helices are labelled S1-S6, charged arginine residues within the voltage sensor S4 helix are denoted with a red +. The linker region between subdomain III and subdomain IV in eukaryotic Navs in which the inactivation loop is known to reside is denoted in red.

`

covalently (β1 and β3) or non-covalently (β2 and β4), composed of an extracellular N-terminal signal peptide and immunoglobulin domain, a transmembrane domain, and an intracellular C-terminal domain (Hanlon & Wallace 2002). In addition to distinct α subunit genes, α subunit splice variants have been identified, indicating a role for alternative splicing in the variation of Nav structure and function. In Nav1.5, in which splicing has been studied extensively, nine different splice variations have been identified (Schroeter et al. 2010). Further post translational modification such as glycosylation(Cronin et al. 2003) and phosphorylation (Scheuer 2011) have also been demonstrated to be modifiers of channel activity. It is this incredible variety of subtle alteration and modification of Nav structure that allows for the complex and intricate network of neural function, responsible for muscle contraction, system regulations, and both basic and higher cogitative function.

1.1 Early Structural Work

The role of Navs in the propagation of electrical signals was first identified in the work of Hodgkin and Huxley, in which voltage clamp experiments on the giant squid axon laid the foundation for our understanding of neuronal function (Hodgkin & Huxley 1990). Electrophysiological studies further developed these models; however it was biochemical work that led to Nav identification, purification and characterisation. The discovery of neurotoxins with high binding affinity for Navs and the development of solubilisation and purification techniques for membrane proteins lead to the purification of the first sodium channel via labelling with a photo-active derivative of scorpion toxin (Beneski & Catterall 1980). This discovery was immediately followed by the tetrodotoxin binding based purification of a sodium channel from the electric eel electroplax (Agnew et al. 1980), part of the organ responsible for the eel's ability to discharge an electric shock, in which Navs are highly abundant. Further work allowed for the incorporation of purified Navs into lipid bilayers, in which their role as sodium channels and their voltage dependence was studied by ion flux assays (Rosenberg et al. 1984). However, it wasn't until the determination of the sequence of the eel electroplax sodium channel, via isolation and cloning from cDNA expression libraries (Noda et al. 1986) that structural work began.

Initial attempts at modelling secondary and tertiary structure based on this primary sequence were fairly accurate even before any experimentally determined

`

secondary structural data had been published. Six transmembrane α helices were predicted in each of four homologous subdomains. The last two helices (S5-S6) in each subdomain were predicted to form the pore, and the S4 helix was predicted to be involved in voltage sensing. Early experimental elucidation of the structure of the pore built upon the previous toxin binding studies, and both tetrodotoxin and saxotoxin were thought to block the channel by binding to the extracellular opening of the pore, and thus one of the first approaches was try to determine the site of toxin binding. A mutagenesis based approach revealed four amino acids, one in each loop between the S5 and S6 of each of the four subdomains, termed the DEKA motif, necessary for tetrodotoxin/saxotoxin sensitivity, as well as sodium conductance (Terlau et al. 1991), indicating that in addition to toxin sensitivity these residues were involved in ion selectivity. The role of these residues as the selectivity filter was confirmed by replacement of this DEKA motif with the corresponding EEEE motif from Cavs, which resulted in a calcium specific channel (Heinemann et al. 1992).

The predicted S4 helices attracted immediate attention due to the presence of the conserved four fold repeat motif of a positively charged residue, typically arginine, followed by two hydrophobic residues. Early models suggested these charged residues to be the basis of voltage sensitivity, proposing that the S4 helix would slide outward and rotate in response to membrane depolarisation, and that this movement would initiate a change in conformation of the pore via the mechanical linkage of S4-S5 linker (Guy & Seetharamulu 1986; Shrivastava et al. 2004). Initial mutagenesis based experiments in both Navs and Kvs demonstrated that neutralisation of these charged residues reduced the steepness of voltage dependent gating, supporting their predicted function in voltage sensing (Logothetis et al. 1992). However, the presence of these charged residues in a helix predicted to have a transmembrane conformation introduced new obstacles, as the presence of these charged residues in the lipid bilayer would be thermodynamically unfavourable. Several highly conserved, negatively charged residues in the S1-S3 helices offered a possible solution to this problem, and initial models suggested that these negatively charged residues would interact with the positively charged residues within the S4 to stabilise it in the lipid bilayer. Mutagenesis studies in both Kv1.2 and the prokaryotic channel from *Bacillus halodurans* (NavBh) have offered support for this hypothesis, demonstrating that the mutation of these negatively charged residues alter the resting state of the channel, as

`

shown by a shift in the steady state activation curves of gating (Miles et al. 2003) (Lee et al. 2005; Paldi & Gurevitz 2010). Subsequent structures prokaryotic Navs have offered further support for this model.

Early biochemical experiments also suggested a role for phospholipids in stabilization of the Nav voltage sensor, as specific lipid mixes were required for reconstitution of channel activity and toxin binding (Hartshorne et al. 1985; Tamkun et al. 1984). Additionally, phospholipids co-purify with prokaryotic sodium channels (D'Avanzo et al. 2013), and were co-crystallised interacting with the voltage sensor and around the hydrophobic regions of Kv1.2/2.1 chimeric structure (Long et al. 2007), and there is mounting evidence for the role of the negatively changed phospholipid in stabilisation of the charged S4 residues in the lipid bilayer (Schmidt et al. 2006; Xu et al. 2008; Zheng et al. 2011).

While it is generally agreed that the S4 helix is the primary voltage sensor whose movement is responsible for the electromechanical coupling of membrane potential and channel gating, how it does so wasn't immediately clear. Initial work suggested that the S4 helix would turn and slide towards the extracellular side of the membrane in response to membrane depolarisation (Guy & Seetharamulu 1986). The positively charged arginine residues in the S4 would sequentially form electrostatic interactions with negatively charged residues in the S1, S2 and S3 helices as the S4 turned and slid, stabilising these charged residues during the motion. The first experimental support for this model was provided in a series of mutagenesis and modification experiments, in which mutation of arginine residues in the S4 helix to cysteine and subsequent modification with sulfhydryl reagents allowed measurements of intra- and extra-cellular availability of these residues as a function of membrane depolarisation. These experiments demonstrated that the S4 becomes more accessible extracellularly and less intracellularly to modification with the sulfhydryl reagents as the membrane depolarised (Yang and Horn, 1995, Yang et al., 1996). Surprisingly, these results suggested that a much smaller than expected area of the S4 was exposed to the lipid bilayer, leading to the hypothesis that there are hydrophobic cavities within which the S4 moves, and serve to focus the membrane around the voltage sensor. The discovery and later crystallisation of independent voltage sensor proton channels, and the demonstration of an ion leak through the voltage sensor when the charged arginine residues are mutated (Sasaki et al. 2006; Starace &

`

Bezanilla 2004; Takeshita et al. 2014) offers support for this model, demonstrating the presence an aqueous channel through the voltage sensor. Modelling of interactions between the lipid bilayer and the voltage sensor further support this hypothesis, suggesting that bilayer deformation around the charged residues may have a focusing effect on the electrostatic field (Bond & Sansom 2007). Further refinement of the Kv1.2 structure offered a mechanism for how this focussing effect could occur, revealing the presence of a hydrophobic layer of residues in the voltage sensor only 10Å thick, which sequence analysis shows to be >90% conserved in the Kv family (Chen et al. 2010). It is expected that this hydrophobic region plays a role in focusing the membrane, reducing the distance required to translocate the gating charges across the electric field, from the previously expected translocation of up to 15-25Å, to a much more modest <10Å. In addition, the Kv1.2 structure also demonstrated that S4 helix could actually take the form of a 3_{10} helix, and models suggested that this would align the arginine residues such that a rotation of the S4 wouldn't be required (Chakrapani et al. 2010; Artimo et al. 2012) This hypothesis was later confirmed in the NavAb and NavRh crystal structures, which have the S4 in a 3_{10} helix conformation, with all of the charged arginine residues on the same face of the helix.

1.2 Function and Dysfunction of Eukaryotic Navs

Overview of the Action Potential

At the cellular level the electrical charge that nerve function is based on is the result of a gradient of charged ions across the cell membrane, most frequently Na^+, Ca^{2+}, and K^+. In excitable cells such as in neurons, muscle, and endocrine tissue, a ligand gated ion channel opens upon binding a neurotransmitter causing a local flux of sodium ions. This change in concentration of negatively charged ions causes movement in a positively charged helix in the voltage sensor of voltage gated ion channels, such as Navs. This electromechanical coupling opens the channel, resulting in additional inward flux of sodium ions, further depolarising the membrane, and causing more voltage gated channels to open, propagating the electrical signal. Within milliseconds of activation the channel is then inactivated by a physical blockage of the pore by an inactivation loop. The membrane is then repolarised by ion transporters and the channel resets to its resting state, ready to repeat the process.

`

While much of the successful structural work on voltage gated ion channels has been performed in prokaryotic channels, it is important to remember that much of the driving force behind the work is a desire to understand the structure the function and dysfunction of eukaryotic Navs. Analysis of the human genome has revealed nine different α subunits and four different β subunits, displaying a variety of different tissue expression profiles and activities. Of the nine α subunits two in particular, Nav1.5 and Nav1.7, have generated much interest for their roles in human biology.

Muscle Navs

Nav1.5 is widely described as the cardiac channel. First cloned from rat cardiac muscle, and shown to be primarily expressed there (Rogart et al. 1989), it has since been the subject of extensive study. Identification and mapping of mutations in humans afflicted with inherited long QT syndrome (Qing Wang et al. 1995; Q Wang et al. 1995) were the first studies to confirm the role of Nav1.5 in human cardiac disorders. Since then Nav1.5 has been implicated in a number of inherited cardiac disorders, including ventricular arrhythmia, impaired cardiac conduction, sudden infant death syndrome, as well as other forms of arrhythmic susceptibility (Amin et al. 2010).

Nav1.4 is expressed primarily in skeletal muscle (Trimmer et al. 1989), and is the primary channel involved in the initiation of muscle contraction in response to nerve stimuli. The first indications that Navs were involved in muscle channelopathies were from observations of ionic conductance of biopsied muscle of individuals with myotonia or periodic paralysis, (Adrian & Bryant 1974; Lehmann-Horn et al. 1983) disorders characterised by prolonged muscle relaxation times following contraction (Platt & Griggs 2009). Subsequent isolation and characterisation of Nav1.4 mutations in patients with these disorders revealed that in most cases the mutations interfered with inactivation, preventing complete inactivation in myotonia, and over-stabilising the inactivated state in periodic paralysis (Platt and Griggs, 2009). Particularly interesting in light of the recent discoveries of voltage gated proton channels composed of a single voltage sensor, are the finding that mutations causing ion leaks through the voltage sensor are the cause of hypo-periodic paralysis (Sokolov et al. 2007; Struyk & Cannon 2007; Struyk & Cannon 2008; Sokolov et al. 2008)

Pain Perception Navs

`

Nav1.7 is the primary channel involved in the perception of pain. Originally isolated and cloned from rabbit schwann cells (Belcher et al. 1995), it was shown to be expressed primarily in sensory and sympathetic ganglia (Klugbauer et al. 1995). In humans, mutations of Nav1.7 were shown to be the cause of several types of inherited erythromelalgia (Yang et al. 2004; Cummins et al. 2007). Following shortly on these discoveries mutations leading to a non-functional or truncated Nav1.7 were identified as the cause of inherited congenital insensitivity to pain (Cox et al. 2006; Ahmad et al. 2007; Goldberg et al. 2007). More recently, patients with Nav1.7 loss of function mutations displaying congenital insensitivity to pain were also shown to be anosmic, lacking a discernible sense of smell, and further experiments in mice demonstrated that Nav1.7 is required for synaptic transfer in the olfactory glomerulus (Weiss et al. 2011). Curiously, Nav1.7 null mutant mice die at approximately post-natal day 15 (Nassar et al. 2004), and it has been speculated that this may be linked to the lack of olfaction. Nav1.8 and Nav1.9 have also been shown to potentially have a role in nociception, nav1.8 null mice display decreased pain-related behaviours (Akopian et al. 1999), and a several different studies implicate Nav1.9 in inflammatory pain, but not neuropathic pain (Cummins et al. 2007)

Neuronal Navs

Nav 1.1, 1.2, 1.3 and 1.6 have been demonstrated to be primarily channels of the central nervous system. All have been shown to be expressed in neurons, and Nav1.6 has been shown to be the primary Nav at the nodes of Ranvier (Black et al. 1996; Caldwell et al. 2000; Beckh et al. 1989). Despite their >70% identity at the amino acid level, knockout in mice of any one of these channels has been shown to be lethal, suggesting that each plays a distinct, non-overlapping role (Catterall et al. 2008). Mutation of Nav1.1 has been found in multiple inherited epileptic disorders, originally identified in mice (Burgess et al. 1995; Kearney et al. 2001) and later confirmed in humans via screening patients with inherited autosomal epilepsy (Escayg et al. 2001; Catterall et al. 2010). Contrasting with the prevalent mutations of Nav1.1, mutations in Nav 1.2, 1.3, and 1.6 associated with disorders are surprisingly rare, although this may potentially reflect a bias in patient screening rather than the rate of occurrence (Catterall et al. 2010). Missense mutation of Nav1.2 have been identified in patients with generalised epilepsy with febrile seizures, and in patients with benign

`

neonatal-infantile seizures, and a truncated Nav1.2 mutation was found in a patient with intractable epilepsy and mental decline (Misra et al. 2008). A Nav1.3 mutation was identified in one patient with treatment resistant epilepsy (Holland et al. 2008). Nav1.6 mutations have been tested primarily in the mouse model, where point mutations can cause ataxic gait and tremor, and behavioural abnormalities indicative of increased anxiety (Meisler & Kearney 2005; McKinney et al. 2008; Papale et al. 2009). Loss of function mutations typically result in death at post-natal day 15 (García et al. 1998), however a predicted loss of function Nav1.6 mutation has been identified in a human patient with ataxia (Trudeau et al. 2006). Missense mutations of Nav1.1, 1.2, and 1.3 have also been associated with autism, further supporting evidence for their role in neural function and behaviour (Weiss et al. 2003; Morrow et al. 2008). Of particular interest are studies which examine the interactions of mutations in multiple channels; demonstrating a cumulative effect in which the overall electrophysiological properties of a cell are a result of more than a single gene. In some cases, this can result in a mutation of a second channel rescuing the phenotype of the first, somehow restoring a balance, and in other cases results in a cumulative effect much worse than either mutation alone (Kearney et al. 2006; Martin et al. 2007; Glasscock et al. 2007; Catterall et al. 2008).

Nav Modulators

Toxins

Naturally occurring toxins evolved by plants and animals for defence or hunting have been a successful source for identification of Nav interacting compounds. Structural research in particular has made extensive use of tetrodotoxin, isolated from puffer fish, and saxotoxin, isolated from marine dinoflagellates, and further structural research has utilised Nav binding toxins isolated from tarantula, scorpion, and marine cone snails. Some of these compounds have offered promise in medical application, (England & De Groot 2009). Unfortunately, the evolutionary advantage of toxins that affect multiple isoforms, which are harder to evolve resistance against and are effective against a wider range of species, has meant that naturally occurring toxins and their derivatives or analogues have limited medical applications. Many non-specific synthetic Nav modulators have found use as local anaesthetics, such as lidocaine and procaine. Local application of these anaesthetics

`

helps prevent undesired side effects resulting from interactions with other channel isoforms, as most Navs are tissue specific. In addition, these modulators specifically interact with and stabilise open and inactivated channels, but have a much lower affinity for channels in the resting state (Courtney et al. 1978; Chernoff 1990). Thus, they act strongly in the rapidly firing nerves involved in pain and neural function, but less so in slower firing muscle tissue nerves, a property exploited by many of the available Nav interacting analgesics and anti-convulsants. However, modulation of specific Navs by compounds targeting unique structural features of the different isoforms offers incredible potential for drug development. The science of pharmacology is reaching the stage where instead of high throughput screening of compound libraries, drugs may soon be designed and developed at the molecular level against specific targets *in silico*. However, precise targeting requires extensive knowledge of structural differences in the Nav family, and will require high resolution structural determination of the different channel isoforms, their splice variants, their post translational modifications, and their interactions with the β subunit before such an approach can be successful.

Insecticides

Several classes of insecticides target Navs. The pyrethroids, analogues of the pyrethrin toxin isolated from chrysanthemum, as well as dichlorodiphenyltrichloroethane (DDT) have both been shown to stabilise the open states of the Navs. This results in extended or continuous nerve firing and hyper-excitability, leading to paralysis and death. Modelling of the Nav-insecticide interaction in housefly predicts the binding site to be located in a hydrophobic cavity of the subdomain II S4-S5 linker and S5-S6 helices, accessible to the lipid bilayer (O'Reilly et al. 2006; O'Reilly et al. 2014). This is supported by electrophysiological experiments in which mutations of key residues in this region are found to confer pyrethroid resistance (Du et al. 2009; Usherwood et al. 2007). Elucidation of the mechanics of Nav activation will be required to better understand the mechanism of pyrethroid activation, and will likely lead to the development of strategies to combat the evolution and spread of pyrethroid resistance in insect populations. Interestingly, mutations conferring increased resistance to pyrethroids in insects have been found in which mutated residue is changed to the homologous residue of the human Navs, but

`

while humans and other non-insect animals have increased resistance, pyrethroids have been shown to have significant toxicity in humans (Shafer et al. 2005), raising questions about the differing mechanisms of pyrethroid action in insects and other animals.

1.3 Introduction to Prokaryotic Navs

Starting with the sequencing of the *Bacillus halodurans* genome, from which the first prokaryotic sodium channel NavBh was cloned (Ren et al. 2001), a superfamily of voltage gated channels has been identified, with members from a variety of bacteria (Figure 1), mostly extremophiles (Koishi et al. 2004). Prokaryotic Navs generally have only 20-25% identity to mammalian Navs, however their hydrophobicity profiles and predicted topologies made them an attractive substitute for Eukaryotic Navs, despite their proposed biological roles in motility, chemotaxis, and pH homeostasis, rather than in electrical signalling (Koishi et al. 2004; Ito et al. 2004; Fujinami et al. 2009).

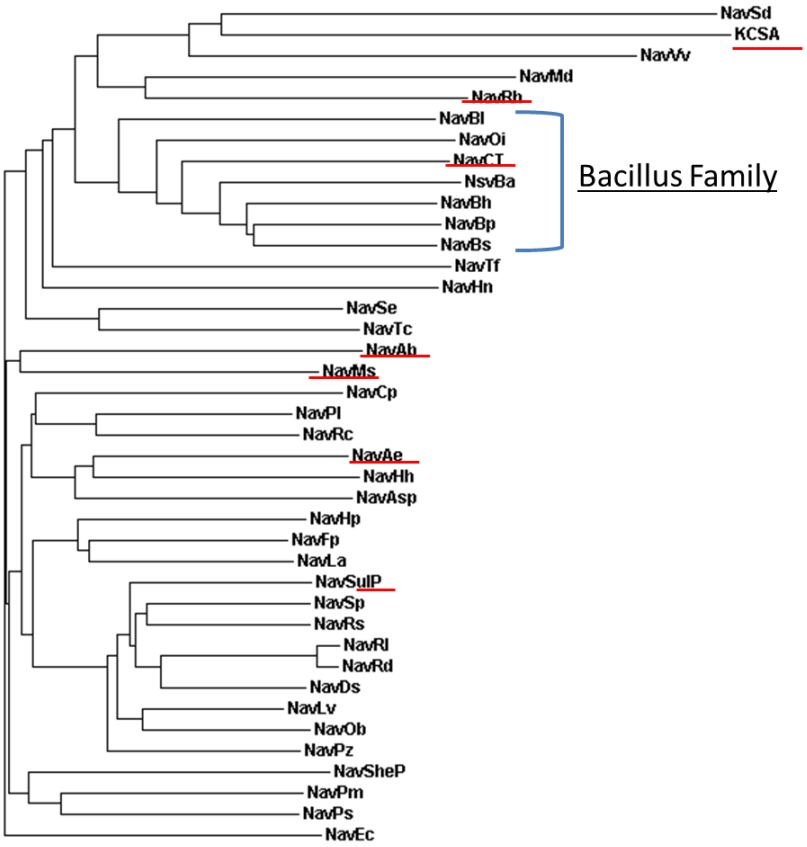

Figure 2: Phylogeny of Prokaryotic Navs.
Generated using Clustal Omega. Navs with published structures are underlined in red, and the Bacillus family, including the archetypal NavBh, is denoted in the bracket. KcsA is included as an out-group.

`

Additionally, their homotetrameric nature, smaller size, and easier expression and purification make them significantly more amenable to structural research that eukaryotic Navs.

Electrophysiology studies have shown NavBh to have a rate of inactivation, 10-100x slower than eukaryotic homologs, which is unsurprising given it lacks the fast inactivation gate found in the linker between subdomains III and IV (Ren et al. 2001). Subsequent study has demonstrated that neither the N-terminal nor the C-terminal intracellular regions are involved in slow activation, and the process is likely mediated via a pore based mechanism (Pavlov et al. 2005). Curiously, prokaryotic Navs are insensitive to many blockers of eukaryotic sodium channels, such as tetrodotoxin, with pharmacology more typical of Cavs than eukaryotic Navs. From an evolutionary perspective this isn't surprising, as Nav channels appear to have diverged from Cavs (Ren et al. 2001; Goldin 2002). Despite these differences, prokaryotic Navs remain an excellent model system to gain structural insight into eukaryotic Navs.

1.4 Crystal Structures of Prokaryotic Navs

Structural Overview

It wasn't until 2011 that the first crystal structure of a Nav was published (Payandeh et al. 2011). Prior to that, all of our knowledge of Nav three dimensional structure came from the single particle analysis cryo-electron microscopy structure of the Nav from electric eel at 19Å (Sato et al. 2001), and from homology modelling based upon potassium channel structures. KcsA (Doyle et al. 1998) and MthK (Jiang et al. 2002) were two of the first ion channels to have crystal structures determined, yielding some insight into the open and closed states of channel pores. Neither of these channels are voltage gated, and insight into the possible structure of the voltage sensor required crystallisation of a homologous voltage gated potassium channel, the first of which was the KvAP channel (Jiang et al. 2003), followed by structures of the mammalian Shaker channel (Long et al. 2005), and a chimera of Kv1.1/1.2 (Long et al. 2007). These potassium channels were used extensively for homology modelling of sodium channels (Shafrir et al. 2008a; Shafrir et al. 2009; Shafrir et al. 2008b) , and many of the assumptions based upon these models were later confirmed by the crystal structures. To date, structures of five prokaryotic Navs have been published (Figure 3).

`

Three similar structures of NavAb from *Arcobacter butzleri,* the first of which contained cysteine mutations in the S6 helix, the second a wild type, and the third containing

NavAb 3RVY	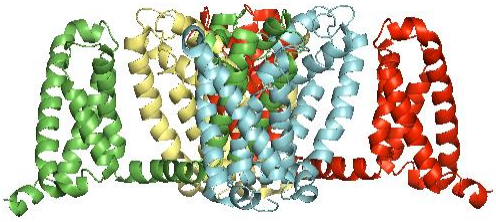	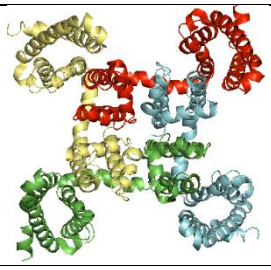
NavRh 4DXW	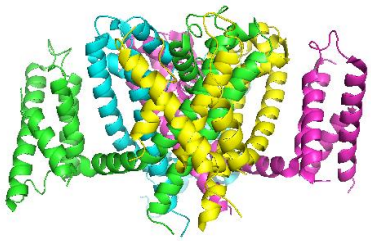	
NavCt 4BGN	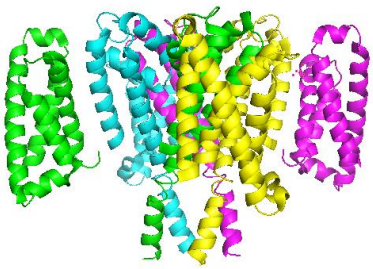	
NavMs 3ZJZ (with MD model of C-terminus)	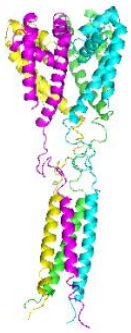	
NavAe 4LTO	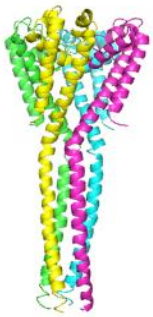	

Figure 3: Models of Nav Structures.
Side view (middle column) and top down view (right column). PDB IDs are listed under channel names (left column). Images are coloured by chain, and were generated in Pymol.

`

mutations within the selectivity filter rendering it calcium selective (Payandeh et al. 2012; Tang et al. 2014; Payandeh et al. 2011) have been published. A single structure of NavRh from *alphaproteobacterium Rickettsiales* sp *HIMB114* is available (Zhang et al. 2012). Structures of the NavMs pore from *Magnetococcus* sp.(strain MC-1) (McCusker et al. 2012; Bagnéris et al. 2013; Bagnéris et al. 2014), and the NavAe pore from *Alkalilimnicola ehrlichei* (Shaya et al. 2014) have also been published, both of which were expressed and crystallised as the pore-only constructs, without voltage sensors. In addition, a 9Å electron crystallography structure of the NavCt channel from *Caldalkalalibacillus thermarum* has also been published (Tsai et al. 2013).

General Structural Features

These prokaryotic Nav structures largely confirm the basic proposed features of Nav structure based on homology modelling, while elucidating on many of the details, and allowing a more in depth analysis of structural features. Of particular interest are the different conformations in which the different prokaryotic sodium channels have been crystallised.

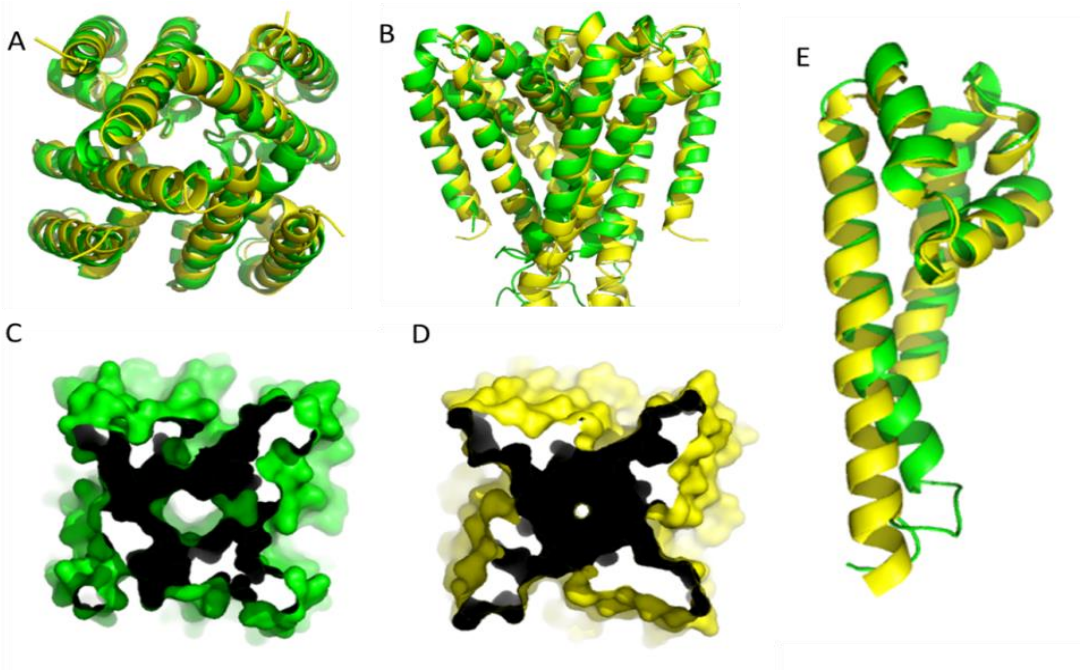

Figure 4: Comparison of Open and Closed Nav Pores.
Side view (A) and intracellular view (B) of the NavMs (PDB ID 3ZJZ) pore in green, overlaid with the NavAb pore extracted from the full length channel structure (PDB ID 3RVY) in yellow. C, D) NavMs pore and NavAb pore surface rendering, cutaway at the narrowest point of the pore, demonstrating the open and closed pores. E) Overlay of the NavAb and NavMs monomers, demonstrating the kink in the S6 helix. Images generated in Pymol.

`

The first structure of NavAb is in a dimer-of-dimers conformation in what is thought to be an activated but closed conformation, whereas the second two NavAb structures are thought to be in inactivated states- in a much more dramatic dimer of dimer configuration, in which one pair of S6 helices have collapsed inwards, and the other pair has shifted outwards. This causes the collapse of the activation gate and selectivity filter, and it is thought this may be the mechanism of channel inactivation. Similar to NavAb, NavRh also is seen in an inactivated conformation. The NavAe pore structure, which lacks the voltage sensor, is also found in a closed conformation, but is noteworthy as it is the only sodium channel structure with a crystallographically resolved C-terminus thus far. The NavMs pore is the only available structure in an open conformation, allowing the identification of a 25° rotation around a threonine residue within the S6 helix as the mechanism for channel opening resulting in an iris like motion, widening at the intracellular end of the channel as compared to the available closed Nav structures (Figure 4) It should be noted that this threonine residue is one turn down from the previously hypothesised glycine hinge of NavBh (O'Reilly et al. 2008; Kellenberger et al. 1997; Zhao, Yarov-Yarovoy, et al. 2004), however NavMs notably lacks a comparable site. In addition to the crystal structure, EPR spectroscopy has allowed for the modelling of the C-terminus of NavMs (Bagnéris et al. 2013), which in striking contrast to the long helical neck region of NavAe, contain a large region of disorder linking the channel to a coiled coil. This disordered region is more in line with the results of circular dichroism spectroscopic studies of the NavBh C-terminus (Powl et al. 2010).

The Voltage Sensor

In both the NavAb and NavRh structures, the voltage sensors are found in an activated conformation, based upon their interaction with a conserved extracellular negative charge cluster, despite the pore being closed. In the voltage sensor, the arginine gating charges are found to make stabilising hydrophilic interactions between helices, confirming previous work suggesting the presence of such interactions, as well as the presence of hydrophobic interactions which are expected to seal the voltage sensor against ion leakage. The structure has also confirmed the previously hypothesised presence of a 3.10 helix in the S4 (Figure 5A,B), allowing the four voltage sensing arginine residues to align in a straight line, and translocate without requiring a

`

twisting motion. Additionally, it should be noted that each voltage sensor is closely associated with the pore of the neighbouring subunit, possibly enforcing concerted gating among the four subunits.

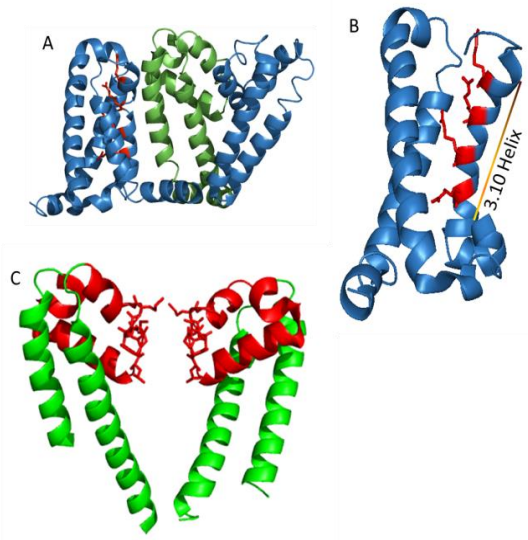

Figure 5: Structures of the Nav Voltage Sensor and Pore.
A) Structure of the NavAb (PDB ID 3RVY) voltage sensor, with adjacent and connected pore. Voltage sensing arginine residues are in red. B) Cutaway view as in A, rotated to better demonstrate the location 3_{10} helix which aligns the voltage sensing arginine residues. C) The S5, S6, and selectivity filter of the NavMs pore. The transmembrane helices are shown in green, the loop between S5 and S6 and selectivity filter loop in red, and side chains are shown for the LESWS selectivity filter motif. Images generated in Pymol.

The Selectivity Filter

Previous work with the Nav selectivity filter had discerned its sequence and general location, and modelling based upon potassium channel structures lead to a general hypothesis of its function. However the Nav crystal structures reveal several key differences. In the potassium channels, the selectivity filter is formed by the backbone carbonyls in the ion selectivity filter, and no intermediary water molecules are involved. Potassium ions are first stripped of their hydrating waters before passing through the channel (Zhou et al. 2001). This is in contrast to what is observed in sodium channel structures, in which the top of the selectivity filter is formed by the side chains of four conserved glutamate residues at the extracellular mouth of the pore (Figure 5C). This site is of a sufficient diameter to fit a sodium ion with two or more coordinating water molecules. This suggests that in contrast to potassium selectivity filter the sodium channel conducts sodium ions in a hydrated state, and an electron density that is likely a hydrated sodium ion found within the NavMs structure further support this hypothesis (C. Naylor, personal communication.

Molecular dynamics simulations have further elucidated the mechanism of sodium conductance. Initial simulations of ion movements within the closed NavAb

`

structure found a series of four ion binding sites within the selectivity filter, and were able to observe hydrated sodium ions moving in between them (Boiteux et al. 2014; Furini & Domene 2012; Ke et al. 2013; Chakrabarti et al. 2013). It wasn't until the publication of the open pore NavMs structure that MD simulations were able to observe conductance, demonstrating the presence of five separate ion occupancy sites (Ulmschneider et al. 2013). Additionally, sites two and three/four found in the MD simulations correspond to the density found within the NavMs structure posited to be sodium ions, as well as to what a calcium ion found at the outermost site in NavAe.

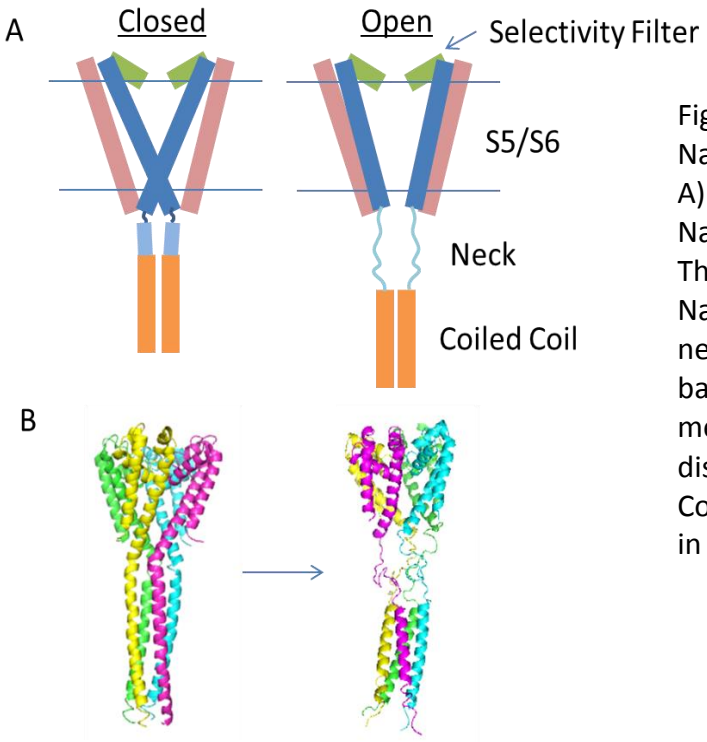

Figure 6: Structure of the Nav C-Terminus. A) Schematic diagram of a Nav pore and C-terminus. The closed conformation NavAe structure has a helical neck the NavMs model based on DEER-EPR measurements has a disordered neck. B) Corresponding structures, as in Figure 3

The C-Terminus

Thus far two structural models including the Nav C-terminus have been published. The C-terminus of NavAe is resolved in the crystal structure (Shaya et al. 2014), and the NavMs C-terminus has been modelled from DEER-EPR measurements (Bagnéris et al. 2013) (Figure 6). As expected from sequence based prediction, the latter part of the C-terminus takes the form of a coiled coil separated from the channel by a region of disorder containing a region of conserved charged residues required for channel expression (Powl et al. 2010). However this disordered region seems to be unusually short in NavAe in comparison to the NavMs C-terminus, and this is supported by truncation analysis of NavBh, and disorder prediction of other homologues (Powl et al. 2010), which also demonstrate this larger region of disorder.

`

It has been hypothesised that this disordered region is involved in channel opening and closing, acting as a spring or tether. This would allow the S6 helices to splay apart, as opposed to the more structured connection region found in the non-conducting NavAe. This more ordered region likely explains why the C-terminus was able to be resolved in NavAe but in no other sodium channel to date. It also explains why the NavAe channel was found to conduct only when this region was mutated to introduce a larger disordered region, suggesting that the rigid structure in this region is preventing the wild type channel from opening. This, combined with the Double Electron-Electron Resonance – Electron Paramagnetic Resonance (DEER-EPR) measurements made of the NavMs C-terminus, leads to the hypothesis that this region undergoes a structural transformation as part of gating (Figure 6A). While closed, the neck region remains in a stable, helical state, but the dilatation at the lower end of the pore due to gating would disrupt the helical structure of the neck region, forcing it to assume a disordered state. This hypothesis requires further investigation, and validation thereof will be particularly difficult, as there are no available ligands which can be used to directly control the conformational state of prokaryotic sodium channels.

Fenestrations

First seen in the NavAb structure, fenestrations have been found in all sodium channels crystallised thus far. These fenestrations provide hydrophobic access to the pore, and are thought to be how many of the hydrophobic drugs and toxins gain access to the pore after partitioning into the membrane. In mammalian brain and cardiac Navs structure-function studies have identified residues at the fenestration homologous to F203, which was identified as controlling drug access to the pore (Qu et al. 1995; Ragsdale et al. 1994). It was first suggested that these fenestrations would close as the channel opens, however in the open structure of the NavMs pore the fenestrations are found to be even larger than in the closed NavAb structure (McCusker et al. 2012). Of note is that in the NavAb structure, a phosphatidylcholine molecule is resolved in the fenestration, whereas in NavMs a HEGA10 detergent molecule is resolved in the same location. This is explained simply enough by the fact that NavAb was crystallised in lipid bicelles, whereas NavMs was crystallised in detergent micelles, as well as the differing charges within the binding pocket. To date

`

only NavMs and NavAb have been crystallised at a sufficient resolution to observe anything in this pocket, however further evidence can be seen from molecular dynamics simulations, in which the fenestrations were found to rapidly fill with one or more phospholipid fatty acid chains from the bilayer (Ulmschneider et al. 2013; Amaral et al. 2012; Boiteux et al. 2014).

1.5 Electrophysiology of Prokaryotic Navs

Electrophysiological characterisation of prokaryotic sodium channels began with the discovery of NavBh, (Ren et al. 2001), and despite publication of crystal structures of other homologues, NavBh still remains the best functionally characterised. Initial characterisation in Chinese hamster ovary cells demonstrated voltage dependence and sodium selectivity similar to eukaryotic Navs, however inactivation and recovery kinetics were found to be slower than in eukaryotic channels (Ren et al. 2001). NavBh has also been characterised by the patch clamp method in African green monkey kidney cells (Kuzmenkin et al. 2004), human embryonic kidney cells (Chahine et al. 2004), and insect cells (Gamal El-Din et al. 2014). NavBh and other prokaryotic Navs demonstrate a pharmacology distinct from that of eukaryotic Navs, and are insensitive to tetrodotoxin, as well as many of the other drugs and insecticides known to interact with eukaryotic sodium channels (Ren et al. 2001). The pore blocker drug mibefradil has been shown to block currents in NavBh , and more recently other prokaryotic Navs have been shown to be sensitive to the same hydrophobic pore-blocking class of drugs (Bagnéris et al. 2014; Raghuraman et al. 2014; McCusker et al. 2011). The halogenated ethers isoflurane, and sevoflurane also inhibit NavBh conductance (Ouyang et al. 2007; Barber et al. 2014).

Some of the early electrophysiological work on NavBh focused on characterisation of mutants to determine the importance of specific residues in selectivity (Yue et al. 2002), as well as in gating and inactivation (Kuzmenkin et al. 2004). Investigation of residues within the pore and selectivity filter determined that inactivation was a property attributable to the pore, and not the amino terminus as in Eukaryotic Navs (Pavlov et al. 2005). This was later supported by the crystal structure of NavAb, in which the part of the pore is collapsed inward suggesting an inactivated state (Tsai et al. 2013). NavBh conduction has also been investigated in synthetic lipid bilayers with the nystatin mediated fusion method, although this has been used

`

primarily as a proof-of-concept study (Studer et al. 2011). A NavBh pore-only construct, in which the voltage sensor has been removed has also been characterised in planar lipid bilayers by the Wallace Lab, in collaboration with the De Planque group at the University of South Hampton (Powl, unpublished data, Figure 7). In this system, NavBh has a symmetric IV curve, with single channel conductance of approximately 5pA. In this system the NavBh pore-only construct also displays an extremely low P_0, or open probability, as without any method of activating the channel only random, isolated opening events can be observed.

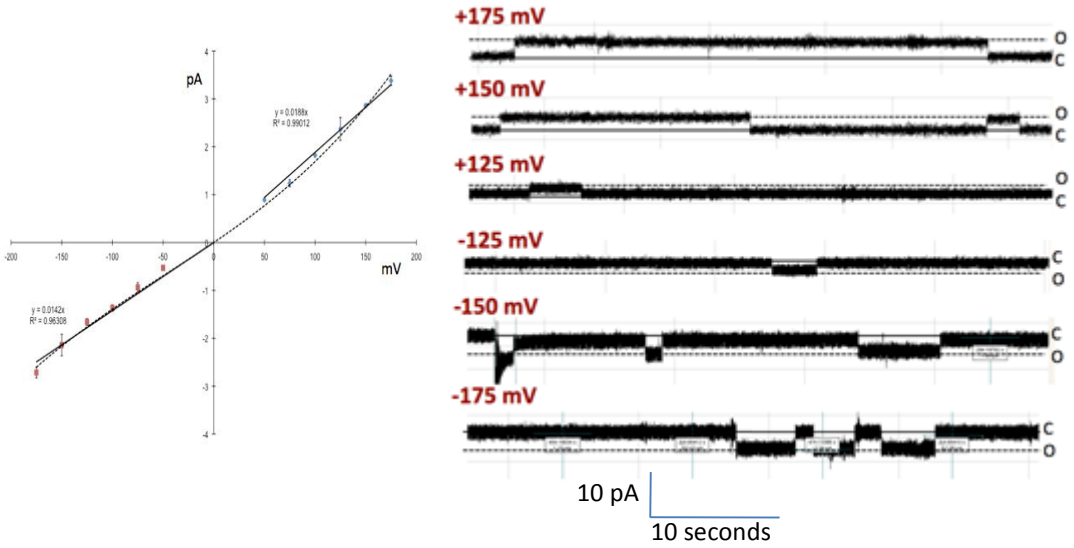

Figure 7: Electrophysiology of the NavBh Pore in a Synthetic Lipid Bilayer.
IV curve(left), and single channel traces (right) of the NavBh pore in planar lipid bilayers, 0.5M NaCl. Experiments performed by Dr Andrew Powl in collaboration with the de Planque group at the University of Southampton, unpublished work.

Later work in NavSulP also demonstrated the role of the C-terminus in accelerating inactivation (Irie et al. 2012), and in NavMs truncation of the C-terminus was found to delay significantly delay inactivation as compared to the wild type (Bagnéris et al. 2013).

Electrophysiological characterisation has also been attempted on all crystallised homologues, however it should be noted that of the channels crystallised, only NavMs displays appreciable currents without modifications to the wild type channel. NavAe required the introduction of several glycine residues to disrupt the helical structure in its C-terminus (Shaya et al. 2014). NavAb conducts, but only weakly, whereas NavRh was not found to conduct in all system tried.

1.6 Previous Work with NavBh

`

As discussed previously NavBh from *Bacillus halodurans* was the first prokaryotic Nav cloned (Ren et al. 2001). While it has not been a cooperative target for crystallisation, it has been well characterised electrophysiologically by the whole cell patch clamp method, and structurally characterised by spectroscopic methods. Previous work in the Wallace Lab developed expression and purification protocols for NavBh capable of obtaining milligram quantities of the protein, as well as demonstrating its tetrameric oligomerisation, and unusually high thermal stability (Nurani et al. 2008). Circular dichroism studies have demonstrated a primarily helical secondary structure, and a C-terminus consisting of a helical region predicted to be a coiled-coil connected to base of the pore by a disordered neck region (Powl et al. 2012). Further work investigated the role of specific residues and regions in thermal stability (O'Reilly et al. 2011; O'Reilly et al. 2008; Cronin et al. 2003; Nurani et al. 2008; Powl et al. 2012). Other groups have focussed on homology modelling approaches utilising the structures of the prokaryotic potassium channels of KcsA and MthK, eukaryotic Kvs, and more recently with the structures of prokaryotic Navs (Paldi & Gurevitz 2010; Kuzmenkin et al. 2004; Shafrir et al. 2008b; Zhao et al. 2004; Blanchet & Chahine 2007; Yarov-Yarovoy et al. 2012; DeCaen et al. 2008; Yarov-yarovoy et al. 2011; Barber et al. 2012). While such investigations are of valuable, they are not a substitute for a high resolution structure.

1.7 Introduction to MthK

MthK is a prokaryotic, tetrameric, two transmembrane helix potassium channel, and was one of the first available crystal structures of an ion channel (Jiang et al. 2002). MthK is ligand-gated by calcium via the RCK domain, which is a large multimeric domain, which has been crystallised independently of the pore in several different configurations and oligomeric forms (Dong et al. 2005; Kuo et al. 2007; Yuan et al. 2011; Jiang et al. 2002; Ye et al. 2006; Derebe et al. 2011; Smith et al. 2013; Pau et al. 2011; Smith et al. 2012). As part of MthK, the RCK domain dynamically forms an octomeric ring, in which four subunits are expressed as part of the primary MthK sequence, and four additional soluble subunits are expressed from the secondary start codon M107 (Figure 10, Figure 8). This octomeric ring is dynamically formed and regulated by calcium binding, and pH (Kuo et al. 2007). Upon calcium binding ring forms and the flexible interfaces open with a clamshell-like motion, causing the entire

`

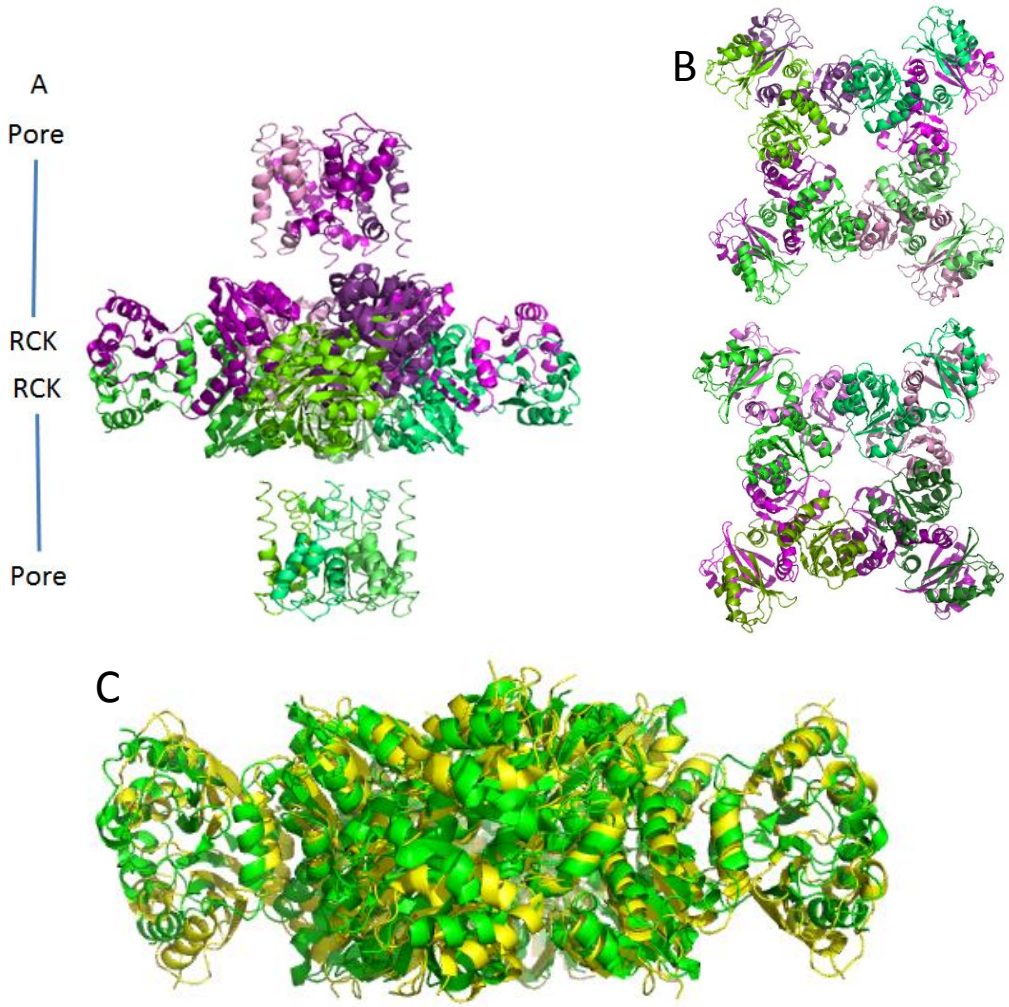

Figure 8: Crystal Structures of MthK.
A) Side view of the MthK crystal structure, in which the M107 secondary start codon has been mutated to an isoleucine (PDB ID# 3RBZ), demonstrating the back to back configuration in which the octomeric gating ring is formed of two Pore-RCK tetramers rather than one tetramer and four soluble RCK subunits. The two tetramers are coloured in purple, and green, and each chain of the tetramer is shade differently, in order to demonstrate the pore-RCK pairing. B) View of the RCK gating ring as in A (top), and crystal structure of the closed RCK gating ring (PDB ID# 2fy8) (bottom). C) Overlay of open (yellow) and closed (green) RCK domain crystal structures from B, side view.

gating ring to expand, which opens the pore via the covalently bound RCK subunits (Chakrapani & Perozo 2007). pH has been shown capable of locking the RCK domains in different conformations, at an acidic pH the soluble RCK domains become insensitive to calcium, and are locked in an inactive dimeric conformation. At an alkaline pH, they are sensitive to calcium, and tend to form the octomeric gating ring (Dong et al. 2005).

`

The RCK domain occurs in several different contexts as part of different proteins. First as a single C-terminal domain that also expresses a soluble subunit from a secondary start codon, as in MthK. This soluble protein expressed from the second start codon is found both in monomeric and dimeric forms in solution, and is capable of dimerising with other soluble RCK subunits, or with those covalently bound to the channel. The RCK domain can also be found either as a two C-terminal tandem domains connected by a disordered linker, such as in the eukaryotic BK channel, or prokaryotic GSuK channel (Yuan et al. 2010; Kong et al. 2012), or as two non-tandem domains, one at the N-terminus, and the other at the C-terminus of a protein, as in Trk and Ktr proteins (Cao et al. 2013; Vieira-Pires et al. 2013).

It should be noted that for the MthK crystal structure, it was the M107I mutant which was crystallised. This mutation changes the secondary start codon from which the soluble RCK subunits are expressed to an isoleucine. As a result, the octomeric gating ring in the crystal structure is formed of the four RCK domains covalently bound to one MthK pore coming together with the covalently bound RCK domains from a second MthK pore, in a back to back formation (Figure 10, Figure 8). It should be noted that this forms the normal flexible/fixed face interactions for the octomeric RCK gating ring, and is not a crystal contact. The RCK domain does however, contribute to many of the contacts within the MthK crystal.

1.8 The Chimeric Fusion Construct NavBh-RCK

Two possible explanations for lack of previous success with NavBh in crystallisation trials are the lack of exposed charged residues outside the hydrophobic transmembrane regions of the protein, and the inherent flexibility of the channel's C-terminus. Based on structural prediction and homology modelling, NavBh has only small, mostly uncharged loops connecting the transmembrane helices, and a flexible C-terminus with exposed residues likely to form crystal contacts in a detergent solubilised environment. The channels conformational flexibility likely also contributes to its inability to form stable, well-ordered crystals. At the inception of this project, MthK and KcsA were the two classical examples of prokaryotic ion channels with crystal structure. KcsA has a helical C-terminus, and has been crystallised with anti-KcsA fragment antibodies providing additional soluble surface area for crystal contact

`

formation (Uysal et al. 2009; Zhou et al. 2001). MthK has a C-terminus consisting of a large, soluble ligand gating domain (Jiang et al. 2002). It is thought that the presence of an ordered, soluble domain was of aid to crystallisation in both channels, providing residues for crystal contacts outside the detergent micelle surrounding the hydrophobic transmembrane regions of the channel. As antibodies against NavBh were not readily available, the NavBh C-terminus was replaced with the regulator of conductance of potassium (RCK) domain from MthK, in order to create the chimeric fusion construct NavBh-RCK (Figure 9).

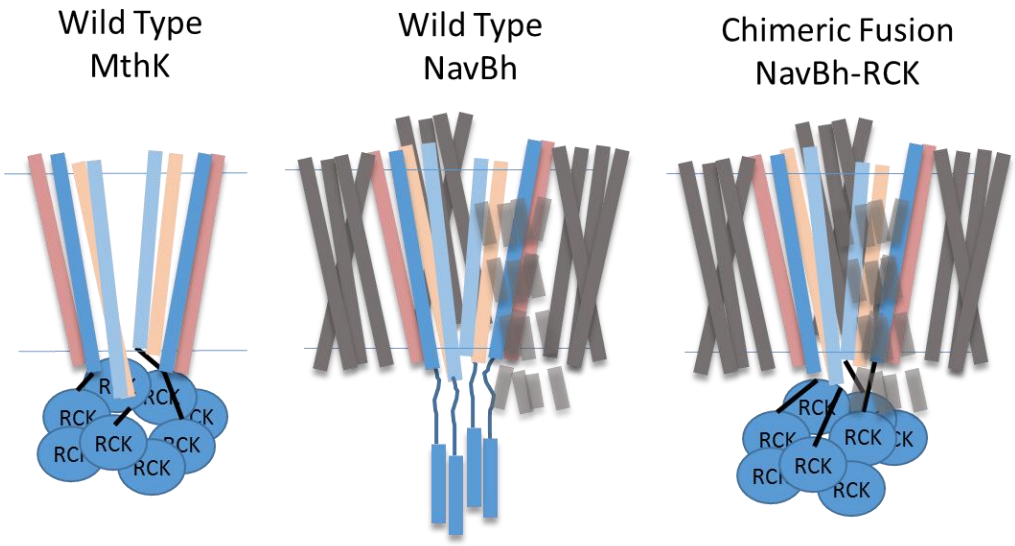

Figure 9: Diagrammatic Representation of Wild Type MthK and NavBh, and of the Chimeric Fusion Construct NavBh-RCK.
The chimeric fusion construct was created by replacing the NavBh C-terminus with the RCK domain from MthK. Pore forming helices are shown in blue and pink, and the voltage sensor helices S1-S4 of NavBh are shown in grey, with dashed and offset helices denoting voltage sensors offset from the cross section. It should be noted that the secondary start codon from which the soluble RCK domains are expressed is kept intact in the construct, unless otherwise noted.

The RCK domain was chosen as it has been shown to readily crystallise as a soluble separate protein, as well as covalently bound to the MthK pore. Additionally, the RCK domain gates the MthK channel in response to calcium binding, which should allow for the creation of a ligand gated Nav. The ability to control the conformation of the channel should also aid crystallisation by allowing for better homogeneity of sample. It should also provide a useful tool for functional characterisation studies.

Previous chimeric approaches have had some success with ion channels, resulting in the Kv1.2/2.1 chimeric structure (Long et al. 2007), and the Nak/NavSulP chimeric structure (Irie et al. 2012), however despite the crystallisation of multiple

`

channels with an RCK domain (Jiang et al. 2002; Kong et al. 2012; Cao et al. 2013; Vieira-Pires et al. 2013), none have utilised the addition of an RCK domain as part of a chimeric strategy to improve crystallisation prospects.

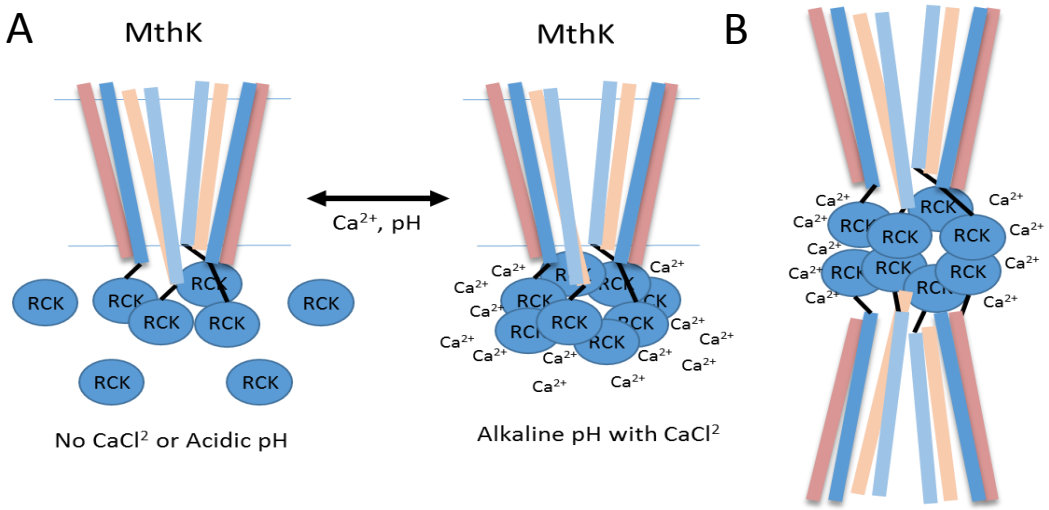

Figure 10: Diagrammatic Representations of MthK RCK Domain Oligomerisation. A) MthK dynamically forms the octomeric gating ring in response to calcium and pH. At acidic pH, the soluble RCK units are insensitive to calcium, but in the presence of calcium at an alkaline pH, the octomeric gating ring forms, with four covalently bound RCK subunits, and four soluble subunits expressed from a secondary start codon within MthK. B) Diagrammatic representation of the MthK crystal structure, in which the octomeric gating ring is formed from the covalently bound RCK subunits from two separate tetramers, and no soluble subunits are present.

1.9 Introduction to NsvBa

A close homologue of NavBh has recently been functionally characterised (DeCaen et al. 2014). Despite sharing >60% sequence identity with NavBh, the channel was found to be non-selective due to a mutation in the selectivity filter and thus is designated NsvBa, as a non-selective voltage gated channel, cloned from *Bacillus alcalophilus*. The high identity with NavBh makes it a particularly interesting target for structural study, as many of residues characterised in NavBh are conserved, which would allow for structural insight into their function if a crystal structure can be obtained.

Investigation of the NsvBa C-Terminus

Despite the series of high resolution Nav crystal structures published recently, in only one of these structures is the C-terminus resolved. As previously discussed, recent work has suggested the possibility that the Nav C-terminus undergoes a

`

structural transition from helical to disorder as part of gating (see page 29, The C-terminus, and Figure 6). Preliminary bioinformatics analysis of NsvBa predicted the C-terminal neck region of NsvBa to be both disordered and helical, suggesting that it may be stable in both helical and disordered conformations. Using a homology modelling approach two possible structural models for NsvBa were developed, based on the NavMs and NavAe structures. SRCD of serial truncations was then performed to determine the secondary structural percentages of NsvBa within the C-terminal neck region, allowing us to determine that in NsvBa the neck region is disordered, allowing validation of the NavMs based homology model.

1.10 Aims and Objectives

Aims

At the inception of this project no crystal structure of a prokaryotic sodium channel had been determined, despite a decade since the initial discovery of NavBh. The Wallace group and others had attempted to crystallise NavBh but with no success. While the crystallisation of integral membrane proteins has historically been challenging due to their hydrophobicity requiring a detergent micelle in order to maintain the protein in a water soluble state, the NavBh C-terminus in particular may interfere with the formation of well-ordered crystals due to its previously discussed disorder and flexibility. Truncation of the C-terminus has not previously been successful at promoting the formation of well ordered, 3D crystals, likely due to the lack of exposed residues capable of forming crystal contacts elsewhere in the protein; as the loops connecting the transmembrane helices are short and mostly uncharged.

In this study, the replacement of the NavBh C-terminus with the large, soluble RCK domain from MthK has been performed, with the primary aim of increasing its crystallisation prospects by replacing a flexible region with a more rigid domain, and providing additional residues known to form crystal contacts. The soluble RCK domain readily crystallises, and its conformation can be controlled by pH and the addition or removal of calcium. This should have improved homogeneity of the sample, and offered the potential to crystallise a sodium channel in multiple conformations. Even after the subsequent publication of multiple structures of prokaryotic Navs, this would be of high value, as no single channel has yet been crystallised in both an open and closed conformation.

`

Furthermore, the fusion of the RCK domain to the Nav channel allowed for electrophysiological characterisation of the construct based on its ligand gating, rather than voltage gating properties. Successful characterisation demonstrated proof of concept that NavBh can be gated by the RCK domain, and such a construct has the potential to be a useful tool in the characterisation of Nav binding drugs. The voltage pulse protocols required to stimulate gating of wild type Navs can be challenging to work with, requiring specialised equipment, thus a ligand gated Nav offers a simpler and more cost effective alternative for electrophysiological characterisation of drug-Nav interactions. Thus it was sought to confirm that NavBh-RCK was gated by calcium under conditions at which the RCK domain is known to be active, in order to verify the successful creation of a calcium gated sodium channel.

During the course of this project, the structure of five prokaryotic sodium channel homologues were published, but despite this NavBh remains an important target. Of all the cloned Navs, NavBh remains the best functionally characterised, with a large body of electrophysiological characterisation of mutations and truncations. A novel Nav homologue, NsvBa, became available during the course of this project. NsvBa has not previously been studied structurally, but had been characterised electrophysiologically. Expression, purification, and crystallisation trials were undertaken for the full length channel, a pore-only construct, C-terminal truncations of each, and for constructs designed to introduce crystal contact forming residues from the NavMs and NavAb structures.

Recent work regarding structural characterisation of the Nav C-terminus suggests that this region acts as a disordered spring, but may also be capable of transition into a helix. Preliminary structural predictions for NsvBa indicated a significant probability for both helical structure and disorder in the region of interest, suggesting that NsvBa is an interesting target for structural study in this region, as it may be capable of adopting both conformations. As such, we sought to investigate the structure of the C-terminus of NsvBa, using a homology modelling approach to identify two potential conformations of the C-terminus, and applying SRCD and EPR spectroscopic techniques to confirm which of these models accurately reflects the secondary structure within this region.

Objectives

`

NavBh-RCK

For the NavBh-RCK chimeric fusion construct, the first objective is to successfully express and purify quantities of protein sufficient for structural study. Then to use circular dichroism to confirm that the chimeric fusion is correctly folded, and to investigate whether its thermal stability is affected in the presence of calcium, as thermal stabilisation is a common signifier of ligand binding. Whether the NavBh-RCK is a functional calcium gated sodium channel will then investigated by electrophysiology in synthetic planar lipid bilayers. In order to determine whether the NavBh-RCK construct crystallises, crystallisation trials will then be performed in a variety of conditions to determine whether the chimeric fusion construct approach has been successful at improving the potential of NavBh as a crystallisation target. Lastly, in light of the subsequent publications of Nav crystal structures, homology modelling and analysis of the unresolved regions of the MthK RCK domain will performed in the context of the NavBh-RCK construct, in order to better understand the properties of the NavBh-RCK fusion chimera.

NsvBa

For NsvBa, the first objective is expression and purification of quantities of protein sufficient for structural study. Crystallisation trials will follow, with wild type and modified NsvBa constructs in an attempt to obtain crystals. Following the preliminary bioinformatics work identifying predicting the NsvBa C-terminus to be both helical and disordered, the structure of the C-terminus will be investigated. Homology models will be generated based on the two available structures with a C-terminus, NavAe and NavMs, and which better models the C-terminus of NsvBa will be determined using SRCD of C-terminal truncations and EPR spectroscopy.

`

Chapter 2: Review of Techniques

2.1 Methods for the Recombinant Expression and Purification of Membrane Proteins from Bacterial Cell Culture

Recombinant protein expression and purification is a key tool in structural biology. Most structural techniques require larger quantities of protein than can be easily purified from a proteins native tissue and expression, and in many cases purification from native tissue an unattractive or even impossible option. For the majority of proteins obtaining milligram quantities requires a recombinant and transgenic approach to expression, in which the gene of interest must first be cloned into an expression vector and transformed into a host organism for expression and purification. In the case of membrane proteins overexpression and purification is frequently a challenging process. Overexpression of integral membrane proteins can disrupt membrane dynamics or ion homeostasis, in the case of ion channels. The few cases where cells have high native levels of expression of a particular membrane protein, such as the voltage gated sodium channel in the electroplax of the electric eel *Electrophorus electricus,* (Agnew et al. 1983) or bacteriorhodopsin in the membrane of *Halobacteria salinaria* (Miercke et al. 1989), have provided important inroads into the study of these proteins. However, for the majority of membrane proteins obtaining sufficient quantities for crystallisation trials and other structural studies requires recombinant expression.

Cloning

The first step in recombinant expression is to obtain the sequence for the target protein. Historically this was a significant barrier, particularly in the case of eukaryotic proteins which must have their mRNA sequence isolated, rather the genomic DNA sequence, in order to account for mRNA splicing. The advent of several technological advances has in many cases trivialised this. Databases of genomic and transcriptomic sequences and DNA synthesis techniques have made obtaining a copy of a gene a simple matter. Once obtained, the DNA sequence is cloned into an expression vector. Restriction-ligation based cloning methods have been widely utilised for decades, in which both the gene and vector plasmid are digested with compatible restriction enzymes, purified, and then ligated together. Restriction-ligation based cloning methods typically require large quantities of DNA to work with,

`

due primarily to loss during purification, and tend to be slow and unreliable in comparison to newer methods, such as PCR overlap extension cloning (Bryksin & Matsumura 2010), ligation independent cloning, (Aslanidis & de Jong 1990) or Gibson assembly (Gibson et al. 2009; Sievers et al. 2011).

Expression

The choice of expression system is typically the first considerations when undertaking recombinant protein expression. Expression in *E. coli* is the simplest and most common method of producing recombinant proteins, owing to its ease of manipulation and inexpensive growth conditions. While most prokaryotic proteins express well in *E. coli*, eukaryotic proteins and membrane proteins often require more complex expression systems. Eukaryotic proteins may require specific folding machinery or post-translation modifications, the mechanisms for which are not present in prokaryotic systems. Membrane proteins may have additional requirements, such as specific lipids necessary to stabilise the protein. Eukaryotic expression systems such as yeast, insect cell, or mammalian cell culture based methods offer an alternative system for proteins which do not express in *E. coli*. Such systems are significantly more complicated to manipulate and maintain than bacterial systems, and as such are typically employed when bacterial expression is not an option.

The choice of expression vector to be cloned into is dependent upon several factors, first and foremost being the expression host organism. Most reports of successful expression of membrane proteins in bacterial systems utilise one of the pET vectors in one of the λDE3 lysogen *E. coli* strains, which have a genomic copy of the T7 bacteriophage RNA polymerase under the control of the lac repressor (Newby et al. 2009; Sahdev et al. 2008; Novagen 2014). However, expression and purification of membrane proteins has also been reported with a pBAD vector, which utilises an arabinose induction system (Guzman et al. 1995; Van den Berg et al. 2004). In addition to dictating the induction method, the vector may include a fusion tags, on either the N- or C-terminus of the recombinant protein. Vectors with signal sequences for secretion or exportation to the periplasm are also available, however these are not of use in the expression of membrane proteins, which should be inserted into the membrane.

`

While *E. coli* grow optimally at 37°, induction and incubation at temperatures as low as 16° may aid successful expression of difficult eukaryotic proteins. A lower temperature during incubation slows translation and should allow the protein more time to fold correctly. Additionally, both inclusion body formation and protease activity are temperature dependent, and the lower temperature will generally impair the cells response to the stress of overexpression (Sahdev et al. 2008). Modification of incubation temperatures may be sufficient to rescue expression of a misfolded protein from inclusion bodies. However, for many soluble proteins solubilisation and refolding from inclusion bodies is a viable purification strategy, assuming accuracy of the refolding can be confirmed. Unfortunately larger and more complex proteins, particularly those with quaternary structure, have a lower likelihood of accurate refolding and assembly. This is particularly true of membrane proteins, which contain large hydrophobic regions unlikely to fold correctly in an aqueous environment. Regardless of incubation temperatures, induction should be performed in the mid to late log phase of the bacterial growth curve, typically at an OD600 between 0.4 and 0.6, in order to avoid protease production associated with induction in the stationary phase (Gräslund et al. 2008).

Modification of the protein sequence can in many cases improve protein expression, and is often desirable for downstream purification. The most common protein modification is the addition of a fusion tag. Fusion tags are normally supplied as part of the vector, although they may be cloned in at a later point. Fusion tags are commonly designed for affinity purification, such as the polyhistidine tag. These tags have the added benefit of being useful in protein tracking throughout a purification process, via immunoblotting. Tags which are specifically designed to improve protein solubility are also available (Sahdev et al. 2008; Esposito & Chatterjee 2006; Arnau et al. 2006). These are generally not designed to address the solubility problems inherent in working with integral membrane proteins, and their success in membrane protein expression is not well reported. Tags designed to specifically improve membrane protein expression in bacterial systems do exist, however they are not commonly used (Neophytou et al. 2007). Fusion tags can be added to either the N- or C-terminus, and care should be taken to consider which approach is more appropriate. Whether removal of the tag by proteolysis after purification is desirable should also be considered, as most tags do include with a short linker containing a protease cleavage

`

site, however not all proteases are functional in the detergent solubilised environment.

In cases where protein overexpression is suspected to be toxic or to disrupt cellular homeostasis, non-functional mutants may improve expression. For example, an ion channel pore-blocking mutation, which otherwise leaves the structure of the protein unchanged, may improve expression. Such targeted mutagenesis does require a basic understanding of the structure of the protein, otherwise a screening approach is required.

Codon bias has long been thought to be one of the primary concerns in transgenic expression of eukaryotic proteins, and there are many reports of the removal of rare codons improving protein expression (Lithwick & Margalit 2003; Gustafsson et al. 2004). However, more recent research has also begun to highlight the role of mRNA secondary structure in recombinant protein expression, and there are even reports of the inclusion of rare codons improving recombinant expression yields (Tuller et al. 2010; Gustafsson et al. 2012). Major alteration of the DNA sequence will likely require gene synthesis for large scale changes, or site directed mutagenesis if only a few codon changes are required, and whether or not these changes will improve protein expression can only be determined through trial and error. From a practical standpoint, this is rarely an effective strategy to pursue when working with difficult to express proteins. However, if a gene must be designed and synthesised in order to obtain it when the cloned gene is not otherwise easily available, accounting for codon bias and mRNA secondary structure in the design process is worth considering, and there are bioinformatics tools designed for this purpose (Wu et al. 2006; Villalobos et al. 2006; Richardson et al. 2010)

It should be noted that historically, one of the most effective strategies for working with difficult eukaryotic proteins is the utilisation of prokaryotic homologs of eukaryotic proteins. This strategy circumvents most of the problems of expressing eukaryotic proteins in prokaryotic systems, and due to the conservative nature of structural homology this method can be an effective tool for gaining understanding of the general structure of a eukaryotic protein. However not all eukaryotic proteins have close prokaryotic homologs, and those that do may not share the properties of interest in the eukaryotic protein, and as such this is not always a useful strategy.

`

Cell Disruption and Membrane Isolation

Cellular membrane disruption can be achieved by a variety of methods, depending on scale and expression system. For systems with a fragile cell, such as human cell culture or plant cell protoplasts, cells can be lysed osmotically by simple resuspension in a hypotonic solution. However, when working with bacterial cells the cell wall must be broken down with lysozyme once resuspended in buffer, typically with high salt concentration to disrupt complex formation, as well as protease inhibitors and DNase. Once the cell wall is removed, disruption is performed either by sonication or high pressure mechanical sheer. Differential centrifugation is then performed to clarify the lysate, centrifuging first at a low speed to remove insoluble components and undisrupted cells while leaving the membrane still in solution. It is at this step that inclusion bodies are isolated away from the soluble contents of the cell. The clarified lysate can then be centrifuged at high speed in order to pellet the membrane fraction, separating it from the cytosolic proteins.

Membrane Solubilisation

Once the membrane fraction has been isolated, it is then solubilised in a buffered detergent solution to release the integral proteins from the lipid bilayer. Most purification methods rely on the protein being in a soluble form, and so the lipids stabilising the transmembrane regions of the protein must be replaced with an amphipathic detergent in order to both effectively purify the protein, and to prevent their aggregation in solution. In the case of ion channels, medium length chain (c_{12}-c_{14}) non-ionic detergents, such as dodecyl maltoside (DM) and n-Dodecyl β-D-maltoside (DDM) are common choices for the initial solubilisation step, as many proteins can be solubilised in them in a functional state (Seddon et al. 2004), and they are relatively inexpensive compared to many other detergents.

In the initial membrane solubilisation step, cost becomes a primary consideration of detergent choice as the entire lipid pellet must be saturated. Concentrations well above the critical micelle concentration of the detergent are typically used, and so large amounts of detergent are required for large scale purifications. In cases where an alternative detergent is desirable for downstream applications (e.g. optimisation of crystallisation conditions) the detergent can be easily exchanged during subsequent purification and wash steps.

`

Affinity Chromatography

Affinity purification methods are based on the selective and reversible binding of the target protein to an immobilised substrate, allowing separation of the protein from solution. For this reason, it is frequently called a “capture” step. The use of a recombinant fusion tag allows effective purification of protein without any prior knowledge of its biochemical properties, with recovery high 90% (Arnau et al. 2006). It is frequently the first step in a purification protocol, due to its high specificity, and as unlike chromatographic methods which fractionate a whole sample based on a biochemical property such as size or charge affinity chromatography specifically removes binding proteins from solution. This makes it is a very effective method for isolation of a protein from either a whole cell lysate or solubilised membrane. This also allows the user to completely exchange the buffer or detergents during the elution step if so desired.

Affinity chromatographic methods fall into several major categories: immunoaffinity, immobilised metal affinity, and ligand-binding partner based methods. Immunoaffinity chromatography is based on the use of an epitope fusion tag and an immobilised antibody. In many cases the tags have been developed for dual purpose, either to improve protein solubility and expression, or to allow visualisation of the target protein, such as in the case of green fluorescent protein (Drew et al. 2006). Ligand-binding partner based methods, such as those based on maltose binding protein, glutathione S-transferase, or strep-tactin, are developed around a pair of specifically interacting molecules, one of which is utilised as a fusion tag and the other is immobilised (Arnau et al. 2006). Similarly to immunoaffinity tags, many of these tags have also been developed to improve protein solubility and expression.

Immobilised metal affinity chromatography (IMAC) is the most commonly used affinity purification. A polyhistidine tag consisting of six to ten histidine residues is joined to the protein by a short linker. The imidazole ring of the histidine residues binds to an immobilised metal chelate, either nickel or cobalt, and this binding can later be competed off using imidazole. Alternatively, ethylenediaminetetraacetic acid (EDTA) or other chelating agent can be used to strip both the nickel and the protein bound to it from the bead or matrix, although this necessitates recharging the residue before it can be utilised again. The primary drawback to IMAC is that it is not as specific as other affinity methods. Some native *E. coli* proteins contain multiple

`

histidine residues in close proximity, which can competitively bind along with the poly-his tagged recombinant protein. Of particular concern when purifying membrane proteins from *E. coli* is the multi-drug efflux transporter AcrB, which has a histidine rich C-terminus making it a common contaminant in IMAC (Glover et al. 2011). To further complicate matters, AcrB has been shown to be upregulated in response to stress, such as during over expression (Ma et al. 1995), and if the contamination is not detected, it will result in false positives during crystal screening as it crystallises readily under a variety of conditions (Glover et al. 2011). Due to this potential for contamination IMAC purification is typically followed by an alternative purification step, such as size exclusion or ion exchange chromatography. However, an additional affinity purification utilising a second fusion tag when the protein is double fusion tagged may also be utilised.

Affinity chromatographic methods can generally be performed in either a batch method, in which beads containing the immobilised binding partner are mixed with the protein solution and then removed either via filtration or centrifugation, or in a column method in which the beads are packed into a column which is then attached to a pump for loading, washing , and elution. The major advantage of column based methods over batch methods is that utilisation of a fast protein liquid chromatography (FPLC) pump, such as an ÄKTAFPLC (GE Life Sciences), allows for very tight control and monitoring of the wash and elution processes.

While the fusion tag is a desirable tool during purification, the presence of a tag may interfere with downstream structural experiments. Many fusion tags are designed with a linker containing a protease site which allows for their cleavage from the target protein. In cases where this is desirable a subtractive affinity purification step can be included to remove the cleaved tag and from solution, as well as contaminating proteins that co-purified along with the target protein. It should be noted that not all endoproteases are effective for membrane protein purification due to the presence of detergent which can either obscure the cleavage site, or interact with protease. Care should be taken while designing the construct to assure that any protease step is compatible with the buffer and detergent. The availability of both the fusion tag and linker region should also be considered during the construct design, particularly in regards to membrane proteins or other multi-domain proteins in which the terminus of the protein may be obscured by another domain.

`

Size Exclusion Chromatography

Size exclusion chromatography (SEC), also known as gel filtration, is typically the final step in protein purification protocols. The protein sample is pumped through a column packed with beads of a porous gel matrix, such as agarose or sepharose. This allows for fractionation of the sample based on relative size. Smaller proteins will travel through the column more slowly, retarded by their movement through porous gel, while larger proteins will not enter the gel and elute more quickly. SEC also separates proteins from small binding competitors used for elution in affinity and ion exchange chromatography, such as imidazole or salts, ideally leaving you with a pure sample in a small volume. Gel filtration columns have an optimal size range and care should be taken to use the best column given the size of the target protein. If a target protein is too large, it will end up in or indistinguishable from the void volume fraction, which contains all the proteins and aggregate that is larger than the effective separating power of the column.

It should be noted that while it is common practice to refer to SEC as separating proteins based on molecular weight, this is not strictly true. As proteins travel through a gel matrix, they are separated based on hydrodynamic volume, not weight, although there is typically strong correlation between the two. This is of particular importance when analysing gel filtration of a membrane protein, as most commercially available standards are globular proteins, and will not account for the size of the detergent micelle. In the purification of membrane proteins, it is important to remember that the detergent and any remaining lipids form a complex with the protein, increasing its effective size.

`

2.2 Methods for the Assay of Voltage Gated Ion Channel Functionality

Introduction

A variety of techniques have been developed for the functional assay of ion channels, however one of the oldest methods, patch clamp electrophysiology, remains the gold standard of ion channel functional assay. Many of the new techniques developed over the past decade focus on low-cost/high throughput, however they are mostly intended for use in the biomedical and pharmaceutical industries in screening potential therapeutic compounds. Such methods are frequently not suitable for high resolution characterisation, as most lack the sensitivity and single channel recording capabilities of patch clamp. Advances in engineering and nanofabrication have paved the way for channel recording in synthetic lipid bilayers suspended in either microapertures or nanoporous materials as an alternative to patch clamp, but only in cases when the protein can be expressed and purified in large quantities. Herein, both the current and historical techniques utilised for the assay of ion channels are reviewed, with the specific application of these techniques for use with voltage gated ion channels held in mind.

Electrophysiology

Introduction to Electrophysiology

The basic principles of electrophysiology rely upon the cell membrane as an electrical insulator separating two conductive substances, the cytoplasm and the extracellular buffer. In this system, conduction is the result of the movement of charged ions across this insulator. The membrane is an imperfect insulator, due to the presence of ion channels, transporters, and pores, and thus it has a measurable resistance. The methods of measuring this fall into two categories- direct and indirect. Indirect methods utilise an extracellular electrode, and as such are non-invasive, resulting in no damage to the biological system they are measuring. Because of this, indirect methods are heavily utilised in the medical field, such as electro-encephalo/cardio/myo-grams, but these unfortunately these methods are not as useful in ion channel characterisation. In contrast, direct methods utilise two electrodes on opposite sides of the membrane, requiring the insertion of an electrode into the system, using micropipette to penetrate the membrane of interest. These

`

electrodes are used to record membrane potential changes resulting from movement of ions across the membrane. While this may seem fairly straightforward, the flow of ions through ion channels is a result of the driving force generated by electro-chemical gradient, which changes as a result of ion flux. The more ions that flow through a channel, the less force there is driving them through, resulting in membrane depolarisation. Historically, this meant that a painstaking experimental setup was only useful for a single recording, and the entire procedure must be repeated as there was no method of easily resetting the membrane potential. In order to avoid this, the process of voltage clamping was developed. Voltage clamping uses an electronic feedback system where a measured membrane potential is compared to a desired potential set by the experimenter, and electric current injection is utilised to correct deviation from this holding potential, supplementing the driving force via electrical injection. The primary application of voltage clamping to a biological system, the patch clamp, has become the gold standard for ion channel characterisation. This is particularly true in the case of voltage gated ion channels which require not just a set potential, but also a controlled depolarisation event in order to gate.

Patch Clamp

While the term "voltage clamp" refers generally to the act of controlling the membrane potential across a membrane. Patch clamp more specifically refers to the act of isolating a patch of membrane and voltage clamping across it, allowing the recording of few or even a single ion channel. There are multiple experimental setups which can offer differing utilities in channel recordings, and differing sets of controlled parameters.

The technique of voltage clamping, in which a feedback circuit and two electrodes are used to maintain a membrane potential at a constant value, is typically attributed to Kenneth Cole and George Marmont. They developed the idea in the 1940s, and the technique was later made famous by the work of Hodgekin and Huxley (Hodgkin & Huxley 1990). Patch Clamp is an extension of the concept, first used by Neher and Sakmann in their investigations of acetyl-choline activated channels (Neher & Sakmann 1976). While the concept of isolating a small patch of membrane for voltage clamping is a fairly simple one, the tools and electronics required to do so are not. The pipettes originally used were fire-polished, with a tip diameters in the range

`

of 3-5µm, which are still not sufficient to achieve a tight enough seal without first enzymatically treating the cells to be used in order to remove topographical features of the membrane to prevent leakage. Further advancements were made when it was discovered that gentle suction applied to the interior of the pipette allowed an extremely high resistance seal to be made (Hamill et al. 1981) which simultaneously made the technique easier to perform rapidly and accurately, while reducing the background noise due to seal leakage.

Electronic Equipment

The advancement of electrophysiological techniques over the past few decades have been in no small part due to advances in electronics. The equipment required has improved since the techniques inception, although its basic functions remain the same. At the core of any patch-clamp experiment is a voltage clamp amplifier, which is responsible for monitoring and maintaining the holding potential across the membrane and recording current via the microelectrodes. The microelectrodes are specially fabricated micropipettes, which contain a silver-chloride wire within the pipette reservoir. The voltage clamp amplifier outputs to a data acquisition device, videocassette recorders were originally used, however this practice has long since given way to digital storage, with the added benefit of much more powerful downstream data processing. A faraday cage is also required to isolate the sample from electronic background noise, although this does not preclude the need for` filtering of the data as a certain amount of noise is inherent in any setup for electrophysiological recording. For patch clamp, a microscope of sufficient power to observe and guide the patching procedure is also required.

Cell Attached Patch Clamp

The simplest form of Patch Clamp configuration is the cell attached patch clamp (Figure 11). In this method, the micro-pipette is positioned against the cell membrane and gentle suction is applied, forming a high resistance seal. Ion channel activity in this small patch can then be recorded. One of the primary benefits of this method, that it leaves the cell intact and undisturbed, is also its primary drawback, as you do not have electrodes on both sides of the membrane. It also does not allow for manipulation of

`

the intracellular conditions.

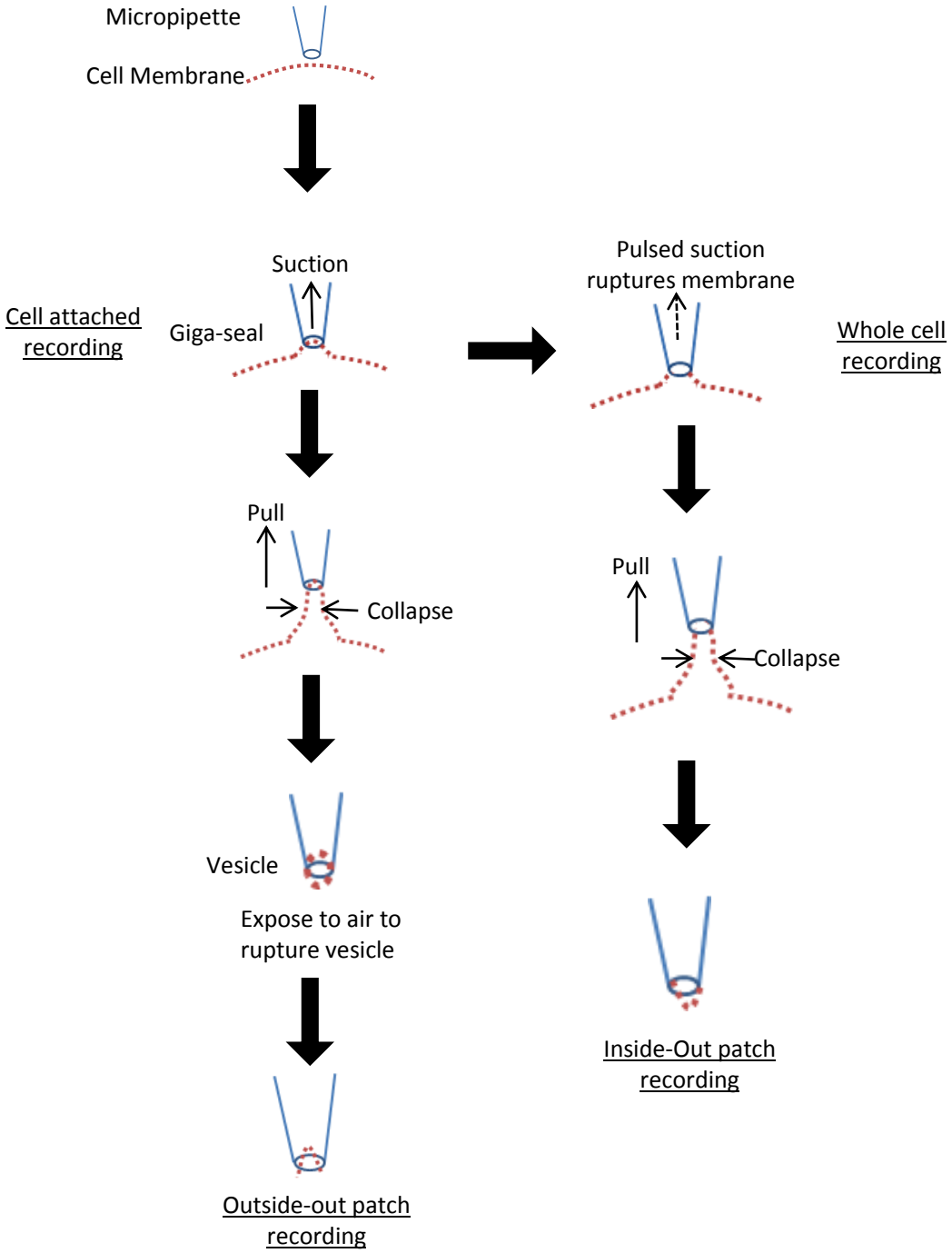

Figure 11: Flowchart Diagram for Setup of the Four Primary Types of Patch Clamp Recording Configurations.
Flowchart diagram detailing the setup procedure for cell attached, whole cell, outside-out, and inside-out types of patch clamp. The micropipette is represented in blue, and the membrane bilayer is red.

Whole Cell Patch Clamp

`

Whole cell patch clamp is similar to simple intracellular recording, in which a pipette electrode is inserted into the cell. The primary difference is that in whole cell patch clamp, rather than pierce the cell with a sharp pipette tip, which causes leakage, the membrane patch is ruptured with aggressive suction after the high resistance seal has been formed. This effectively inserts an electrode into the circuit, which is the coupled with another electrode inserted into the bath solution (Figure 11). While this method does leave the cell membrane mostly intact, the pipette reservoir used is large enough that wash out of the cell by the pipette solution is unavoidable, as the volume of the cell is negligible compared to the volume of the pipette reservoir. While this can be a benefit if intra-cellular factors are suspected to be interfering with channel gating, it does preclude any observations of these phenomena. Wash out also eventually results in the loss of channel activity, due the disruption of the cytoskeleton and heavy dilution of the cell contents. In cases where these problems need to be avoided, a modification of this method called perforated patch clamp can be employed. In perforated patch clamp instead of being ruptured, the membrane patch is perforated, through the use of polyene antibiotics such as nystatin or amphotericin B, which form small pores permeable to inorganic monovalent ions, but not to the divalent ions of interest for ion channel conductance.

Outside-Out and Inside-Out Excised patch

Both outside-out and inside-out excised patch clamp refer to the basic technique of excising the patch of membrane attached to the pipette in a whole-cell patch clamp setup. This results in a small patch of membrane isolated on the tip of the pipette. The primary purpose of these methods is to allow electrical and chemical control over both the intra- and extra-cellular solutions. The terms inside-out and outside-out refer to whether the intracellular or extracellular faces of the membrane ends up in contact with the bath solution. An outside-out patch is obtained by rupturing the cell membrane as in whole cell patch clamp, then pulling away. As the pipette is pulled away, some of the membrane sticks to the pipette, and due to the hydrophobicity of the lipid bilayer it then folds over and tries to reconnect, covering the tip of the pipette with an excised patch of membrane, with the intracellular side in contact with the pipette solution (Figure 11). An inside-out excised patch is obtained in a similar method, except instead of initially rupturing the membrane patch the

`

pipette is placed against it and tightly sealed, as in the cell-attached configuration. The pipette is then pulled away, taking a whole patch of membrane with it, which then folds upon itself to form a vesicle, which is then destroyed by exposure to air (Figure 11), leaving the intracellular side of the membrane facing the bath solution, which can then be manipulated as the experimenter desires either prior to or during an experiment.

Recent Improvements in Patch Clamp

Patch clamp is a technique requiring expertise to perform, however the development of robotic platforms capable of performing patch clamp with minimal supervision has the potential to greatly increase the speed at which measurements can be obtained. While the results from such platforms have yet to match the reliability and quality in data acquisition that an experienced human technician can achieve, successive generations may yet accomplish full automation of the process. While such platforms will likely be of limited use in academic research, they are of great interest to the pharmaceutical industry, where a high throughput approach is extremely desirable, and lower data quality in the initial screening steps is not a drawback. One of the primary ways in which this automation is achieved is via planar patch clamp, in which rather than the pipette being manually manipulated into contact with the cell, a cell suspension is placed on a planar chip containing an aperture, which performs the same function as a pipette. Suction is applied, which brings a cell into contact with the aperture, and generates the seal, negating the need for manual manipulation of a pipette (Estacion et al. 2010).

Voltage Clamping of Synthetic Bilayers

While the voltage clamping of an synthetic lipid bilayer suspended within an aperture between two aqueous compartments has long been possible. For many years the primary obstacle has been the requirement of organic solvent in the generation of the lipid bilayer, the presence of which quickly and irreversibly destroys protein ion channels. Synthetic lipid bilayers are also delicate enough that stability over the course of a recording is a problem. Engineering advances reducing the size of the aperture and allowing aperture shaping have significantly improved membrane stability, as compared to initial apertures generated by punching a pin through a plastic sheet. Advances in material science have allowed the generation of apertures

`

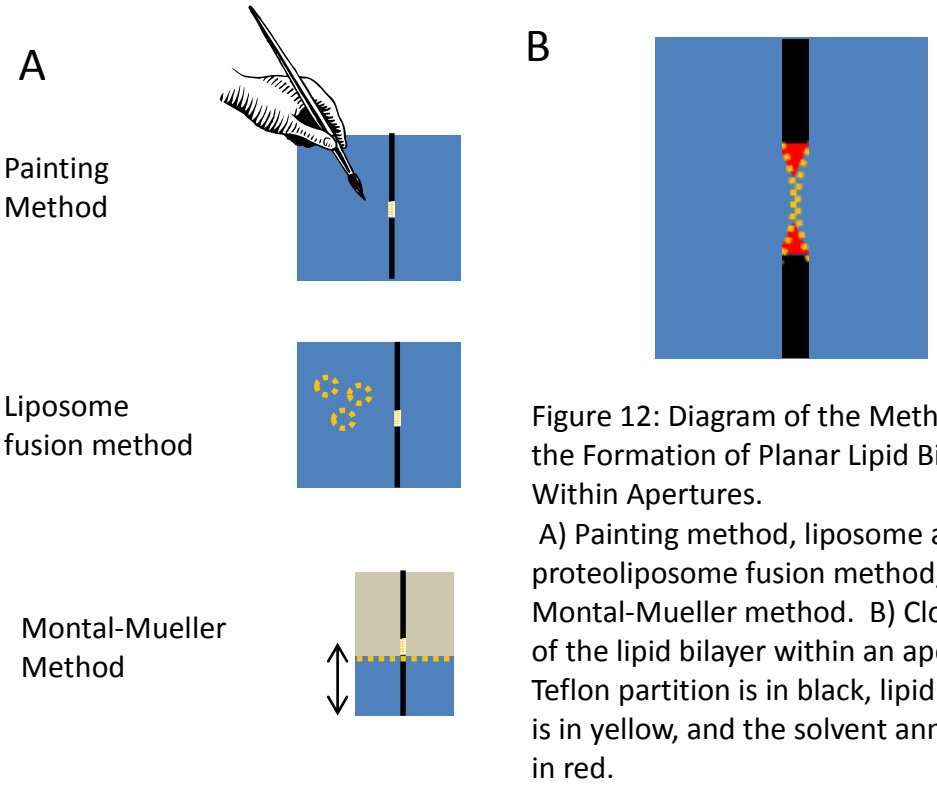

Figure 12: Diagram of the Methods for the Formation of Planar Lipid Bilayers Within Apertures.
A) Painting method, liposome and proteoliposome fusion method, and Montal-Mueller method. B) Close up of the lipid bilayer within an aperture. Teflon partition is in black, lipid bilayer is in yellow, and the solvent annulus is in red.

in the range of 50 to 100 µm in diameter, and for tapering of the pore edge (Kalsi et al. 2013; Kalsi et al. 2014). A bilayer may more easily be formed in such an aperture, and is more stable. The bilayer can be generated within the aperture by putting a small amount of lipid on a paint brush, and painting over the aperture to create a lipid/solvent plug (Figure 12a). This plug can then thinned into a bilayer by raising and lowering the buffer level, however small amounts of the organic solvent used to dissolve the lipid do remain, and may disrupt protein structure. Alternatively, the Montal-Mueller method can be utilised, in which the lipid dissolved in chloroform is pipetted into the buffer, and allowed to spread to the surface of the buffer on both sides of the pore (Montal & Mueller 1972). After evaporation of the solvent, the buffer level is then raised and lowered past the pore, allowing the lipids to fold over the aperture, hence this method is sometimes called the “folding” method (Figure 12b).

The second major obstacle to the use of synthetic lipid bilayers in the characterisation of ion channels is the problem of inserting the ion channels into the lipid membrane. Ion channels, like all transmembrane proteins, are hydrophobic and are not soluble without the presence of a detergent micelle, however detergent disrupts the hydrophobic interactions which maintain the stability of the lipid bilayer.

`

Membrane proteins can, however, be reconstituted into liposomes. Early studies suggested that integration of proteoliposomes into planar lipid bilayers was encouraged by the presence of either an osmotic gradient, or open channels (Woodbury & Miller 1990; Woodbury & Hall 1988). Several studies have successfully utilised proteoliposome integration into planar lipid bilayers for the characterisation of ion channels, using an antibiotic –sterol pair (also known as the nystatin method) to induce liposome fusion (de Planque et al. 2006), and using this technique characterisation of reconstituted NavBh has been published, however single channel conductance differs from experiments performed by the Wallace Lab (Studer et al. 2011) Powl, unpublished results, Figure 7). This method has fairly significant drawbacks though, in that you introduce an active ion channel into the bilayer, and while in theory it is deactivated prior to voltage clamping, it is almost impossible to confirm this. However, given patience, liposomes are capable of fusion with an artificial lipid bilayer with no more encouragement than simple agitation (Mendes et al. 2005; Kalsi et al. 2014).

As compared to traditional patch clamp, voltage clamp recording of ion channels reconstituted within synthetic lipid bilayers does have several distinct advantages, primarily if the aim is a single channel recording. Protein to be reconstituted is first purified, and as a result there is no possibility of interference from channels native to the system. Additionally, the composition of the lipid bilayer can also be completely controlled, as can the concentration of channels. While these things can be modified within a patch-clamp experiment, doing so is a much simpler process when the entire system is created artificially, rather than co-opted from a living cell.

Other emerging techniques utilise supported synthetic lipid bilayers, typically spread horizontally over a microporous or nanoporous material (Studer et al. 2009; Tiefenauer & Studer 2008; Reimhult & Kumar 2008). The benefits of a supported bilayer are primarily in stability, as the supporting structure prevents bilayer deformation during voltage clamping and helps the bilayer resist breaking due to other stresses. Such supports can also be integrated into a chip, allowing easy voltage clamping and recording. The primary obstacle in working with supported bilayers is that the space between the membrane and the support is extremely small, typically not enough for intracellular domains of transmembrane proteins to fit. As such,

`

tethered bilayers have been developed, which increase the space between the bilayer and supporting structure. While this gives enough space for protein intracellular domains, the buffer volume is still small enough that even limited ion flux is enough to deplete or saturate the ion concentrations enough to have a significant effect on the driving force. Microfluidics offers potential solutions, (King et al. 2012) however work perfecting these systems is still ongoing.

Data Analysis and Filtering

The first step in the processing of electrophysiological data is data filtering. Filtering is essential as all electrophysiological setups inherently have some electrical noise. Single ion channel recordings in particular can have conductance as small as a few picoamps, and noise of five picoamps or more is not unusual. Historically such filtering was done via hardware filters as part of the data acquisition process, owing to the limitations of data manipulation post recording. Today most filtering is done via software filters post recording, allowing much finer manipulation without any loss of raw data. At the most basic level, the filtering process can be thought of as a moving average, in which each time-point sample is replaced by the weighted average of a given number of samples on either side, effectively compressing the range of random variation within the sample. One obvious side effect of such filtering is the gradual sloping of sharp transitions within the data, such as the sharp transitions between open and closed channel states. Filter algorithms address this problem by differential weighting of data points within the running average, and a variety of different algorithms are available with different processes. While the choice of filter is an important consideration in data analysis, for the purposes of ion channel characterisation the gaussian filter is the most common choice, as it produces no offshoot or ringing associated with sharp transitions, and does not introduce a phase delay into the data (Molecular Devices 2006), making it ideal for ion channel recordings.

Once filtering has been performed, the next step in data analysis is the identification of channel gating events. For this section only single channel analysis will be considered, as this method is the most robust and most straightforward, and is gold standard for the characterisation of ion channels. It should be noted that single channel analysis is not necessarily exclusive to membrane patches or lipid bilayers with

`

a single channel. Multiple channels may be present, but as long as gating events do not overlap, the data can be treated as single channel analysis for purposes other than determining the channels open probability, or P_O. Gating event detection can either be done simply by eye, or a computational approach can be taken utilising an algorithm from experimenter's software package of choice. With either approach, once gating events have been correctly identified, further analysis options become available. First among these is the previously mentioned P_O analysis, which is simply the determination of the fraction of the time that a channel is open during a given trace. This does not actually tell you much about the channel however, and in many cases dwell time analysis, which is the average time span of a gating event, is more informative.

If recording has been performed over range of holding potentials, typically a set of at least three positive and three negative (e.g. -50, -100, -150, 50, 100, 150), the current/voltage relationship or IV curve, can be determined for the channel. In these graphs the current amplitude is plotted against the holding potential. Typically, histogram analysis is performed to determine the amplitude for an open single channel at a given voltage, although it can also be done by eye.

There are several potential complications to single channel data analysis, beyond simple noise. The presence of more than one active channel at a time can result in a stepwise change in current, although this can be analysed fairly simply as long as the conductance is a multiple of the conductance of a single channel. In the case of recordings of channels in synthetic lipid bilayers, this can be complicated if the channel is capable of conducting ions in both directions but at different current values, as under these experimental conditions channel integration into the bilayer occurs in both orientations, and inward versus outward conductance measurements must be separated in order to determine an accurate conductance. In the case of patch clamp this is not a concern, as channel orientation is controlled by the cell during insertion into the plasma membrane. Other complications to data analysis may come from the experimental setup in the form of a drifting baseline, which can typically be attributed to leakage in the seal or in the bilayer itself. While computation methods can be used to attempt to correct for this, it is likely a better choice to modify the experimental parameters to prevent this from occurring, as the most likely cause is experimental

`

error, and at the very least experimental error should be ruled out before analysis on such data is attempted.

Voltage Pulse Protocols

Most typical ion channel gating occurs in response to a stimulus of some type. In the case of ligand gated channels, gating is stimulated by adding the ligand. However, in the case of voltage gated channels typically very little activity is seen simply sitting at a holding potential. While the inherent random motion of the channel, also referred to as "breathing motion", can cause gating events, this is difficult to observe, as the holding potential required to drive ion flux also holds the voltage sensors in the closed position, preventing channel conductance. In order to observe conductance of voltage gated channels, a voltage pulse protocol is utilised. This requires a more advanced electronic setup capable of changing holding potentials much faster than a human could physically move a switch on a hardware amplifier.

Ion Conductance Microscopy

Scanning ion conductance microscopy was first developed in 1989 for use on flat polymer films (Hansma et al. 1989), and the technique was later successfully applied to measure ion channels in intact cell membranes (Korchev et al. 2000). The technique has been of use in studying ion channel localisation in membranes, and has been incorporated into traditional patch-clamp as a pre-patch navigational system used to guide patching of active ion channels, rather than empty patches of membrane (Gu et al. 2002). The basic technique is essentially patch-clamp, except the micropipette is not adhered to the cell membrane, leaving it free to scan across the membrane surface for activity. This technique is useful if the experimenter wishes to investigate ion channel localisation; however the lack of a high resistance seal makes the technique unsuitable for detailed channel characterisation.

Ion Flux and Voltage Measurement Methods

One alternative to measuring ion flux electrically is to measure the changes ion concentration that result from ion flux. The primary benefit of such techniques is that they do not require the expensive electronic equipment and expertise necessary for electrophysiology. Instead, they utilise either an ion sensitive dye such a ruthenium red, or a radioactive isotope to allow experimental determination of changes in ion

`

concentration. The drawback is that the data you get from such studies is very low resolution, both temporally and quantitatively, as compared to electrophysiological methods. Such experiments can confirm the presence or absence of an active ion channel, as well as comparative studies in which changes in signal can be observed between different conditions. As such, ion flux measurements are not suitable for detailed characterisation of an ion channel; however they are useful tools. Radioactive isotopes of course have the associated safety concerns, and as such may not be a desirable option for many experimenters. Ion staining dyes, on the other hand, are safe and relatively easy to use. However in the case of sodium channels, no sodium efflux dye systems are yet available commercially, although radioactive efflux studies have been used to good effect in studies of prokaryotic Navs (D'Avanzo et al. 2013; McCusker et al. 2011). One alternative to ion sensitive dyes is to utilise a voltage sensitive dye. This strategy that has been utilised in the development of techniques targeted at the biopharmaceutical industry, such as the electrical stimulation voltage ion probe reader (Huang et al. 2006), or techniques using fluorescence imaging plate readers (Baxter et al. 2002; Arkin et al. 1990). These and similar techniques are based primarily upon the theory of fluorescence resonance energy transfer, and are of great use to the biopharmaceutical industry as they scale up much better than traditional electrophysiology, and particularly for drug screening applications the low resolution is not an issue.

Emerging technologies at the interfaces between biology, engineering, and physics offer a glimpse at the future of what ion channel characterisation may hold. Single atom quantum probes, for example the nonvacancy centre in a nanodiamond crystal, can be highly sensitive to magnetic fields, and have shown potential as a fluorescent probe in addition to being sufficiently sensitive to measure ion flux in real time (Hall et al. 2010). Such technologies may greatly simplify the monitoring of ion channel activity, both for industrial and academic research.

2.3 Circular Dichroism and Synchrotron Radiation Circular Dichroism

Circular dichroism spectroscopy is a technique which allows for the measurement of the chirality of a sample via its differential absorption of polarised light. One of its primary uses is the study of protein secondary structure, as protein secondary structure is inherently chiral. Alpha helices, beta sheets, and unstructured

`

amino acids each give rise to distinctive peaks (Figure 13), with the spectra for a given protein being the sum of its component secondary structure. CD can be performed with a bench top machine which allows for measurement in the far UV wavelength region of 190-250nm, where the n-π* and π-π* transition of the amide bond of the peptide backbone can be observed, as well as the near UV region of 250-300nm, where transitions arising from the aromatic sidechains can be observed (Wallace 2009). CD can also be performed using a synchrotron light source (SRCD) to expand the range to include the far UV, below 190nm (Wallace & Janes 2003). The more powerful light source also allows for higher concentrations of absorbing molecules, such as salts or some buffers, which many proteins need to maintain their structure, as well as a lower signal to noise allowing observation of smaller spectra changes.

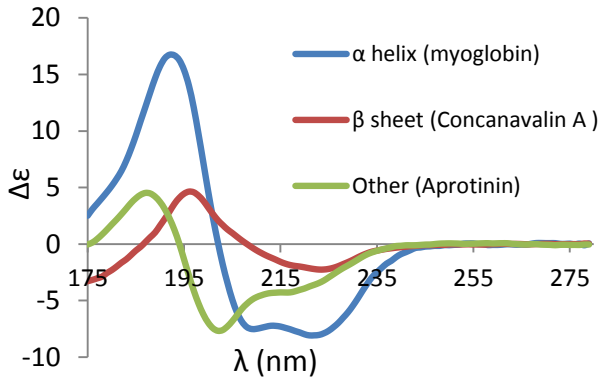

Figure 13: Example CD Reference Spectra.
Reference spectra for a mostly alpha helical protein (myoglobin, PCDDB ID CD0000047000), a mostly beta sheet protein (concanavalin A, PCDDB ID CD0000020000), and a mostly unstructured protein (aprotinin, PCDDBID CD0000007000).

Measurements are typically made in either quartz cuvettes, or specially fabricated demountable cells. Circularly polarised radiation is produced by passing radiation from the source through a series of mirrors, prisms, and slits, which is then passed through the sample, and then to a photomultiplier for detection. The filtering process to produce the polarised radiation has the effect of very significantly decreasing the intensity of light reaching the sample, resulting in a final signal with a difference in absorbance on the order of $3x10^{-4}$. Bench top CD machines use a powerful xenon arc lamp, however the power of the light source is still a limiting factor, thus for cases where high resolution spectra are required, or where an absorbing molecule is required in the buffering solution, SRCD can be particularly useful.

`

Once averaged and calibrated against a baseline, typically camphorsulfonic acid, the processed spectra can then be deconvoluted with analysis software which uses a reference set of CD spectra from proteins with known crystal structures to create representative spectra for the principle types of secondary structure, allowing reconstruction of the unknown spectra from this set of reference spectra. The secondary structure can then be calculated based upon the proportional secondary structure composition of the recreated spectra from the reference spectra used in the reconstruction (Whitmore & Wallace 2004). It should be noted that membrane protein spectra are shifted due to the low dielectric constant of the hydrophobic environment, and thus ideally a reference set of membrane proteins, such as MP180 (Abdul-Gader et al. 2011) should be included in the deconvolution (Wallace & Janes 2009).

Within structural biology, CD is most commonly used to confirm that a recombinantly expressed protein is correctly folded, however the technique can be used to quantify any change in secondary structure, such as one induced by ligand binding or thermal denaturation, or for comparison of different constructs. While it is a low-resolution technique compared to X-ray crystallography or NMR spectroscopy, both of which can generate information at the atomic level, SRCD can be a useful technique for the validation of models produced with such techniques. CD does have several advantages compared to higher resolution techniques however, as it requires much small quantities of purified protein, and can typically be performed in a single afternoon once purified protein has been obtained.

Sodium channels in particular have been well characterised via CD and SRCD spectroscopy, including characterisation of thermal stability (Charalambous et al. 2009; Powl et al. 2012; D'Avanzo et al. 2013), determination of local secondary structure via serial truncation analysis (Powl et al. 2010), and characterisation of ligand binding by thermal stability assay (Nurani et al. 2008). These results demonstrate that sodium channels are majority alpha helical proteins, and that they maintain an unusually high helicity during thermal denaturation.

2.4 Electron Paramagnetic Resonance Spectroscopy

Electron paramagnetic resonance (EPR) is a technique used to measure differences in the spin of unpaired electrons. It is similar to nuclear magnetic resonance (NMR), however it is the excitation of electron spins rather than the spins of

`

atomic nuclei that are observed. Unpaired electrons are introduced into a protein via spin label, which is attached to the sulfhydryl groups of a cysteine residue. Labelled proteins can then be observed with either continuous wave (CW) or double electron-electron resonance (DEER) techniques. CW-EPR measures the local conformational flexibility of a spin label, which gives the user information about the conformational flexibility of the local protein region. Spin labels attached to well-defined secondary structure are conformationally restricted, whereas spin labels attached to disordered residues have a much greater freedom of movement. DEER-EPR, on the other hand, specifically measures the distance between two spin labels, acting as a molecular ruler. Using an electromagnetic pulse, the spin echo decay of a spin label is modulated by the intermolecular dipolar interaction with a nearby second spin label. This leads to an oscillating echo decay, the period of which reflects the average distance between the two spin labels (McHaourab et al. 2011). A series of such measurements can then be integrated in a computational modelling approach to yield fairly detailed structural information.

Membrane proteins in particular have been of interest for study by EPR spectroscopy. Not only is the bottleneck of protein crystallisation avoided completely, EPR spectroscopy can also be performed with protein in both detergent micelles in reconstituted liposomes. Furthermore, unlike crystallographic approaches EPR can be used to observe the dynamic range of a proteins structure, which is particularly useful for flexible or disordered proteins.

EPR spectroscopy is a relatively new technique as applied to sodium channels, having been applied to develop a model of the NavBh voltage sensor (Chakrapani et al. 2010), and more recently to develop a model of the NavMs intracellular C-terminus (Bagnéris et al. 2013). It has also been utilised in the study of potassium channels (Perozo et al. 2002; Lee et al. 2005; Cieslak 2010; Raghuraman et al. 2014), as well as with pentameric ligand gated ion channels (Dellisanti et al. 2013).

It should be noted that EPR spectroscopy is a technique that has a great deal of potential to elucidate the dynamic nature of Navs. Even when a crystal structure is available, it can be difficult to determine whether the conformation captured is one that is physiologically relevant. Additionally, the captured state exists as only a single snapshot, and only through assumption and interpolation between structures

`

captured in different conformations can any information be gleaned about the structure function relationship that occurs during channel gating.

`

Chapter 3: Methods and Materials

3.1 Cloning

Codon optimised NavBh-RCK was ordered from Eurofins MWG Operon (Ebersberg, Germany) as a synthesised gene and cloned into pET15b (Novagen, Billerica MA, USA) by Dr Andrias O'Reilly. All modified NavBh-RCK constructs were generated by Overlap Extension PCR cloning / site directed mutagenesis, using the corresponding primers (Table 2) ordered from Eurofins MWG Operon. NsvBa was provided by Dr Paul DeCaen of Harvard Medical School, (Cambridge MA, USA) and was cloned into pet15B by Dr Claire Bagnéris. All modified NsvBa constructs were generated by Overlap Extension PCR cloning and site directed mutagenesis, using the corresponding primers (Table 2). All constructs were sequenced by GATC sequencing service (Cologne, Germany).

Plasmids were transformed into custom grown chemically-competent *C41 E. coli* (Sigma-Aldrich) cells by standard heat shock protocol (incubation at 42°C for 45 seconds, followed by 5 minute incubation on ice, 1 hour recovery period at 37°C, and plating on Lysogeny Broth (LB) agar with the 100 μg/mL ampicillin (Sigma-Aldrich) for overnight incubation.

3.2 Polymerase Chain Reaction Overlap Extension Cloning and Mutagenesis

Overlap extension polymerase chain reaction cloning was performed as described (Bryksin & Matsumura 2010). Briefly, the target sequence to be cloned was amplified with primers with homologous overlaps for the target vector (Table 2), using NEBPhusion polymerase, following the manufacturers standard protocol (NEB, Ipswitch MA, USA). This step was confirmed by agarose gel electrophoresis, and a second PCR was performed to extend the megaprimer generated in that step into the full length plasmid vector. This was followed by digest with DPNI (NEB) and transformation into chemically-competent NEB5α cells (NEB) following the manufacturers protocol. Cells were plated onto LB Agar with 100μg/mL ampicillin, and incubated overnight at 37°C. A single colony was then used to inoculate 10mL of LB culture supplemented with 100μg/mL ampicillin, which was grown overnight and the plasmid purified using the wizard miniprep kit following the manufacturer's protocol (Sigma-Aldrich). The inserted gene was sequenced from the plasmid to confirm

`

successful cloning (GATC), plasmids with the correct insert were stored at -20°C for further use.

PCR Mutagenesis was performed using designated primers (Table 2), with NEBPhusion following the manufacturer's standard protocol.

3.3 Expression, Cell Disruption, and Membrane Harvesting

For protein expression 200mL of LB supplemented with 100 µg/mL ampicillin was inoculated from a glycerol stock and incubated overnight shaking at 37°C. 10 mL of overnight culture was used to inoculate flasks of 750 mL LB, which were grown at 37° to an OD600 of 0.5-0.6, and induced with 0.5 mM Isopropyl β-D-1-thiogalactopyranoside (IPTG, Sigma-Aldrich). Post-induction NavBh-RCK was incubated for 16 hours at 22°C shaking. Post-induction NsvBa was incubated three hours at 37°C shaking. Cell culture was harvested by centrifugation at 6000 g for 10 minutes. Cell pellets were frozen, and stored at -20°C until used.

Cell pellets were thawed and resuspended in 20 mM sodium phosphate or 20 mM Tris, 0. 5 M NaCl, 1 mM $MgCl_2$, 2 µg/mL DNaseI (NEB), 2 mg/mL Lysozyme (Sigma-Aldrich), and one dissolved EDTA-free proteinase inhibitor cocktail tablet (Roche, Indianapolis IN, USA). Cells were then lysed using an EmulsiFlex-C5 (Avestin, Ottawa, ON, Canada) and unlysed cells and insoluble cellular components were pelleted by centrifugation at 15,000 g for 45 minutes, and the pellet discarded. Membranes were pelleted from the supernatant by centrifugation at 41,000 g for 3-6 hours, and stored at -20°C.

3.4 Membrane Solubilisation and Purification

Membrane pellets were solubilised in membrane solubilisation buffer (2% n-dodecyl β-d-maltoside (DDM, Sigma-Aldrich), 20 mM sodium phosphate pH 8, 0.5 M NaCl, and centrifuged at 20,000 g for one hour to remove insoluble material. 80 mM imidazole (NavBh-RCK constructs) or 20mM imidazole (NsvBa constructs) was then added to the solubilised membrane, and IMAC capture was performed using either Ni-NTA resin (Qiagen, Venlo, Netherlands) , or with a HistrapFF column (GE Life Sciences Buckinghamshire, UK).

For Ni-NTA resin IMAC purifications, 0.5 mL bed volume Ni-NTA resin was washed and equilibrated to the membrane solubilisation buffer. Solubilised membrane was incubated with the resin at 4°C overnight, and then the Ni-NTA resin

`

was washed with the listed imidazole concentrations in wash buffer (20 mM sodium phosphate pH 8, 0.5 M NaCl), and eluted in elution buffer (wash buffer plus 500 mM imidazole).

For Histrap column purifications, columns were equilibrated to the membrane solubilisation buffer (10 column volumes). Solubilised membrane solution was then loaded by peristaltic pump, and allowed to recirculate overnight at 4°C. For NavBh-RCK constructs, the column was then washed with an imidazole gradient from 75 mM to 120 mM on an ÄKTA Fast Protein Liquid Chromatography pump (GE Life Sciences) at 4°C and then eluted with 0.5 M imidazole by filling the column with one column volume and pausing for one hour, repeating this soak-elute cycle five times. For NsvBa constructs, the column was washed with a gradient of 0-80 mM Imidazole, and eluted with a gradient of 80-500 mM imidazole.

Affinity purified samples were concentrated in a centrifugal protein concentrator (Pierce, Leicestershire, UK) with a molecular weight cut off of less than half the predicted molecular weight of the expected oligomeric form of the protein to be concentrated, and run on a Superdex 200 10-300 gel filtration column (GE Life Sciences), or on a Superdex-Increase 200 10-300 column (GE Life Sciences). Fractions were analysed by SDS-PAGE and/or Western blotting.

3.5 Sodium Dodecyl Sulphate Poly-Acrylamide Gel Electrophoresis and Western Blotting

Protein samples were loaded with Nu-Page gel running buffer (Invitrogen Carlsbad CA, USA), and run on a NuPAGE 4–12% gradient Bis-Tris gel in 3-(N-morpholino)propanesulfonic acid buffer (Invitrogen). The BenchMark molecular mass standards (Invitrogen) were run in the left lane. Gels were then either stained with coomassie blue (Sigma-Aldrich) for observation, or transferred to a polyvinyl difluoride membrane for western blotting using the iBlot system (Invitrogen). After transfer, the membrane was blocked in 5% rehydrated milk, and the incubated with monoclonal anti-poly-his-alkaline phosphatase antibody (Sigma-Aldrich) in Tris buffered saline, 0.1% Tween, 0.5% rehydrated milk. Membranes were then developed using BCIP/NBT FAST tablets (Sigma-Aldrich), according to the manufacturers standard instructions.

3.6 Gluteraldehyde Crosslinking

`

5 µL of 2.5% gluteraldehyde (Sigma-Alrdich) was added to 100 µL of protein at approximately 1 mg/mL in 20 mM sodium phosphate, and incubated at room temperature. Samples were taken at the indicated time points, quenched with 500 mM pH 8 Tris buffer, and visualised on SDS-PAGE and coomassie blue staining (Sigma-Aldrich).

3.7 Synchrotron Radiation Circular Dichroism Spectroscopy

SRCD spectra were collected on the DISCO beamline at the Soleil Synchrotron, French National Synchrotron Facility, or on beamline CD1, ISA, University of Aarhus, Denmark by Dr Andrew Miles and Dr Jose Luis-Lopez. The extinction coefficient of each protein was calculated from the amino acid sequence utilising Expasy ProtParam (Gasteiger et al. 2003), and used to determine the concentration by measuring the absorbance at 280nm on a Nanodrop 1000 UV spectrophotometer (Desjardins et al. 2009). SRCD spectra were collected for proteins at approximately 1-4mg/mL, in a Suprasil demountable cell (Hellma, Müllheim, Germany) over a wavelength range of 260 nm to 175 nm in triplicate, using a 1 nm step size and a dwell time of two seconds. For thermal unfolding analysis the temperature was raised in the indicated increments, and three scans were collected at each temperature after a three minute equilibration. Three baseline spectra consisting of buffer collected from the protein concentrator flow-through were averaged and subtracted from the averaged sample spectra. The resulting spectra were calibrated against a spectrum of camphorsulfonic acid collected after the beam fill (Miles et al. 2003). The spectra were smoothed with a Savitsky-Golay filter, and scaled to delta epsilon values using mean residue weight values calculated for each protein. Data processing was carried out using CDTools software (Lees et al. 2004) and analysed on the DichroWeb analysis server (Whitmore & Wallace 2004) using the CONTINLL algorithm (Provencher & Glöckner 1981; van Stokkum et al. 1990), and the MP180 reference set (Abdul-Gader et al. 2011).

C-terminal truncation analysis calculations were performed by determining the helical percentage for each spectra by deconvolution. This was then multiplied by the length of the construct, and subtracted from the value given for the full length c-terminal construct 277 of the same set of SCRD measurements. Values shown are averaged of three replicate sets of SRCD measurements.

3.8 Bioinformatics and Modelling

`

Sequence alignments were performed with Clustal Omega (Sievers et al. 2011) and the hydropathy based alignment algorithm AlignME (Stamm et al. 2013). Structural superpositions were performed using the superposition program in CCP4 (Collaborative Computations Project, 1994). Modelling of the NavMs-RCK linker region was performed in Rosetta (Rohl et al. 2004). Automated homology modelling was performed with the Phyre2 server (Kelley & Sternberg 2009) and the SwissModel server (Schwede et al. 2003) and refined in Modeller (Eswar et al. 2006). Image generation and further model refinement was performed in Pymol (DeLano 2002). Sequence structure predictions were performed on the PsiPred server, using the PsiPred and DisoPred functions (McGuffin et al. 2000; Ward et al. 2004).

3.9 Electrophysiology

Electrophysiology was performed as previously described (Kalsi et al. 2014). Microaperture SU8 sheets were generated by Dr Sumit Kalsi of the de Planque lab (Southampton University, Southampton, UK) by stereolithography (Kalsi et al. 2013), and then clamped between two teflon cups. The cup-sheet interface was treated with Vaseline petroleum jelly to prevent leakage. The microaperture was pre-treated with 5% hexadecane in hexane, and then was dried in order to leave a hexadecane annulus within the aperture, before a buffer of 20 mM Tris pH 8, 0.5 M NaCl was added. PE:PG lipid bilayers (1:1 molar ratio) were generated by the Montal-Mueller method (Montal & Mueller 1972), in which lipids solubilised in chloroform are applied to the surface of buffer on either side of a nanoporous SU8 sheet. The setup was then left for the chloroform to evaporate for 20-30 minutes, before a bilayer was generated across the aperture by raising and lowering the buffer level within the cups past the aperture, until a suitable capacitance was observed. Proteoliposomes of NavBh-RCK constructs were then added to the ground side, along with calcium to the final concentration of 10µM. Recordings were performed within a closed faraday cage. A high sensitivity ID562 BLM amplifier (Industrial Developments Bangor) was used for electrophysiological recordings. Data was acquired at 5KHz with a home built lab view interface. A National Instruments 6036E DAQ card (Newbury) was utilised for the conversion of analogue to digital signals, and chloride silver wire was used for the electrodes. Data was recorded in ClampEx10.2, and analysed with the ClampFit software package (Molecular Devices).

`

3.10 Proteoliposome Reconstitution of NavBh-RCK

NavBh-RCK was reconstituted in 1:1 1-palmitoyl-2-oleoyl-sn-glycero-3-phosphoethanolamine:1-palmitoyl-2-oleoyl-sn-glycero-3-phospho-(1'-rac-glycerol) (PE:PG) liposomes by detergent depletion, as previously described for NavBh (Powl et al. 2012). Lipids were dissolved in chloroform, mixed in a ratio of 1:1 PE:PG, and the chloroform allowed to evaporate. Lipids were then dissolved in reconstitution buffer (0.25% CYMAL5, 20 mM Tris pH 8, 500 mM NaCl) by water bath sonication for 20 minutes. NavBh-RCK in detergent solution was added at a calculated molar ration of approximately 1500:1 lipid:NavBh-RCK octomer. Detergent was removed using Biobeads (Bio-Rad, Berkly CA, USA) following the manufacturer's protocol. Proteoliposomes were then removed from the Biobeads, and snap frozen in liquid nitrogen and stored at -80°C until use.

3.11 Continuous Wavelength and Double Electron-Electron Resonance Electron Paramagnetic Resonance Spectroscopy

EPR spectroscopy was performed as previously described (Bagnéris et al. 2013). Gel filtration of affinity purified NsvBa cysteine mutants was performed as previously described in the presence of 5 mM dithiothreitol (DTT, Carbosynth, West Berkshire, UK). DTT was then removed by buffer exchange during protein concentration on a centrifugal concentrator (Pierce). Concentrated protein was then incubated overnight in the dark at 4°C with a 20-fold molar excess of the spin label 3-(2-iodoacetamido)-PROXYL (Sigma-Aldrich). Free spin label was removed by gel filtration on a Superdex 200 10/300 column, and then the sample was buffer exchanged into D2O and 20% deuterated glycerol (Sigma-Aldrich). Samples were transferred into 50mL capillary tubes for CW-EPR. CW-EPR was performed at room temperature on a Bruker EMXplus spectrometer operating at 9.4 GHz equipped with a 4122SHQE resonator. Measurements were performed using 0.2 mW microwave power, 100 kHz modulation frequency, 0.1 mT modulation amplitude and 10 ms conversion time and time constant. Samples were then transferred into 5 mm NMR tubes (Sigma-Aldrich) for DEER-EPR measurements. DEER measurements were performed at 50 K on a Bruker ELEXSYS E580 spectrometer operating at 9.6 GHz equipped with an ER-4118-X-MD-5 resonator, Oxford Instruments continuous flow cryostat (CF935) and ITC503 temperature controller. The four-pulse DEER sequence used was p/2(nobs)-tl p(nobs)

`

t0 p(npump) (tlþt2 t0) p(nobs) t2 echo, where the observer pulse length was 16 ns for p/2 and 32 ns for p pulses. The pump pulse length was 12 ns. The long interpulse delay (t2) was 3,000 ns. All other parameters were according to (Pannier et al. 2000) with t1,0¼400 ns and Dt1¼56 ns. Data points were collected in 8 ns time steps. The total measurement time for each sample was in the range of 24–36 h. Spectra were analysed using the programme DEERAnalysis2011 (Jeschke et al. 2006). The background was corrected by a homology three dimensional fit and the distance distributions evaluated by either Tikhonov regularisation or two Gaussian distance distributions or two Rice distance distributions. The damped oscillation reached a plateau by 0.5 ms.

Data collection and analysis were performed by Dr Enrico Salvadori, and Prof Chris Kay of University College London.

3.12 Crystallisation Trials

Crystallisation trials were set up by the vapour diffusion method, in 150 nl sitting drops, utilising a Mosquito crystallisation robot. Protein was purified by gel filtration in the listed buffer and trials were setup with the listed crystallisation screens (Tables 3, 4 and 5). Crystallisation trials were monitored at the listed temperature for a period of 6 months for the formation of crystals. Crystallisation screens were purchased from Molecular Dimensions, Suffolk, UK,

`

Chapter 4: Investigation of the NavBh-RCK Chimeric Construct

4.1 Overview

As previously discussed, the chimeric fusion construct NavBh-RCK was designed in an attempt to improve the channel's crystallisation prospects (see chapter 1.8). Theoretically, it should have done so in two ways. First, it included a large soluble domain that was known to crystallise on its own. Second, the ligand gating function of this domain should have allowed for control of the channel's conformation. Addition of the ligand should have decreased the flexibility of the protein, resulting in better conformational homogeneity in the purified protein. The addition of a ligand gating domain also created the opportunity for electrophysiological characterisation of a ligand gated sodium channel, which if successful had potential as a tool in drug binding assays. This chapter describes the expression and purification of NavBh-RCK. Its low solubility was investigated by purification trials, CD spectroscopy, and homology modelling. Electrophysiological characterisation demonstrated that it was a functional ligand gated sodium channel. However, the unstable conductance combined with the low channel solubility indicated that the chimeric fusion approach was only partially successful. Lastly, *in-silico* structural analysis was performed which suggested that differences between the prokaryotic potassium channel helix-bending model of gating and the iris-like gating mechanism demonstrated by the Nav crystal structures may be the source of the low solubility and precipitation displayed by NavBh-RCK.

4.2 Expression and Purification of NavBh-RCK

Initial Expression Trials

NavBh-RCK was initially provided as a codon optimised construct in pET15B by Dr Andreas O'Reilly (formerly of the Wallace lab). Preliminary expression tests of the N-terminally hexahistidine tagged NavBh-RCK were successful both at 37°C for three hours, and at 22°C overnight (Figure 15: Expression Trials of NavBh-RCK Constructs.). However western blots of IMAC purification demonstrated that NavBh-RCK did not bind to the nickel (Figure 16A) or cobalt resin (data not shown). This was unexpected, as wild type N-terminal hexahistidine tagged NavBh is known to have an exceptionally strong affinity for nickel resin. Thus, a model-based approach was employed to investigate the likely structure around the N-terminus of the protein.

`

A

```
           ----------S6----------       *
MTHK   TVTLIVLGIGTFAVAVERLLEFLINREQMKLMGLI...
NavBh  FVSFVLIGTFIIFNLFIGVIVNNVEKAELTDNEED...
```

B

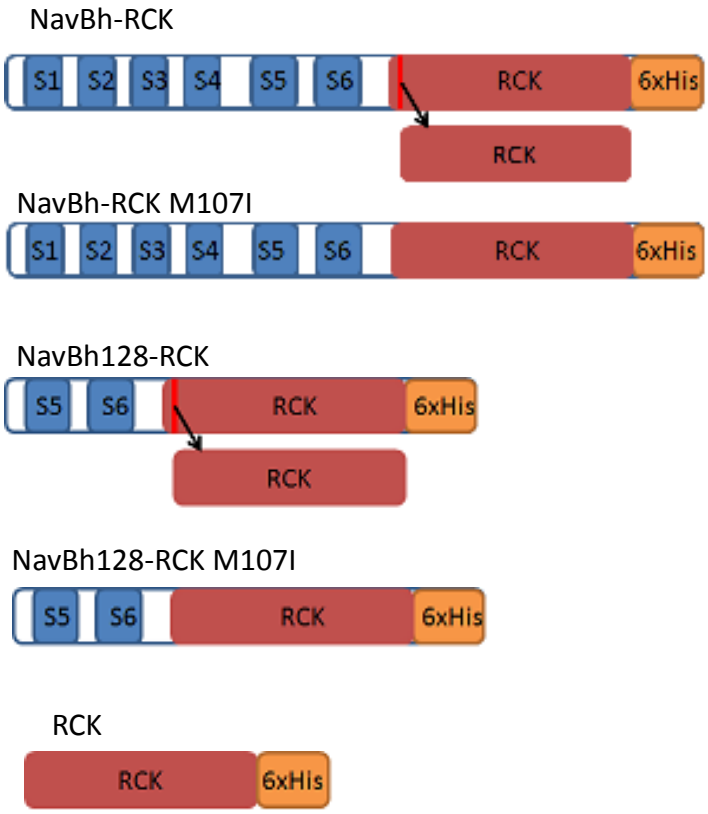

Figure 14: Diagrammatic Representation and Alignment of NavBh-RCK Constructs. A) Alignment of the end of the last transmembrane helix, and linker/neck regions of MthK and NavBh. Transmembrane helices are shown in blue, and the sequence of the NavBh-RCK construct is underlined. The M107 secondary start codon is highlighted in yellow, and denoted with an asterisk. B) Diagrammatic representations of the C-terminally hexahistidine tagged NavBh-RCK constructs. Transmembrane helix domains are shaded in blue, the RCK domain is shaded in red, and the hexahistidine tag in orange. Secondary start codon M107 are shown as red lines, and constructs with secondary start codons mutated to isoleucine are shown without the red line, and without the separate soluble RCK domain.

Superposition in CCP4 was performed, of the MthK crystal structure with the newly published crystal structure of the prokaryotic sodium channel NavAb (Payandeh et al. 2011). This was used to observe the general structural features and likely orientation of the NavBh-RCK chimera (Figure 17: NavAb-RCK Model). This suggested that the tag could easily reside in one of several pockets which would render it unavailable during IMAC (Figure 17B). The C-terminus of the protein was clearly accessible however, and moving the tag to the C-terminus also had the added benefit

`

of tagging the soluble RCK domain. C-terminally hexahistidine tagged NavBh-RCK expressed at similar levels to the N-terminally tagged construct. It bound to the nickel resin, requiring stringent elution conditions similar to those for wild type (WT) NavBh (Figure 18B). All subsequent NavBh-RCK constructs were cloned with this C-terminal hexahistidine tag.

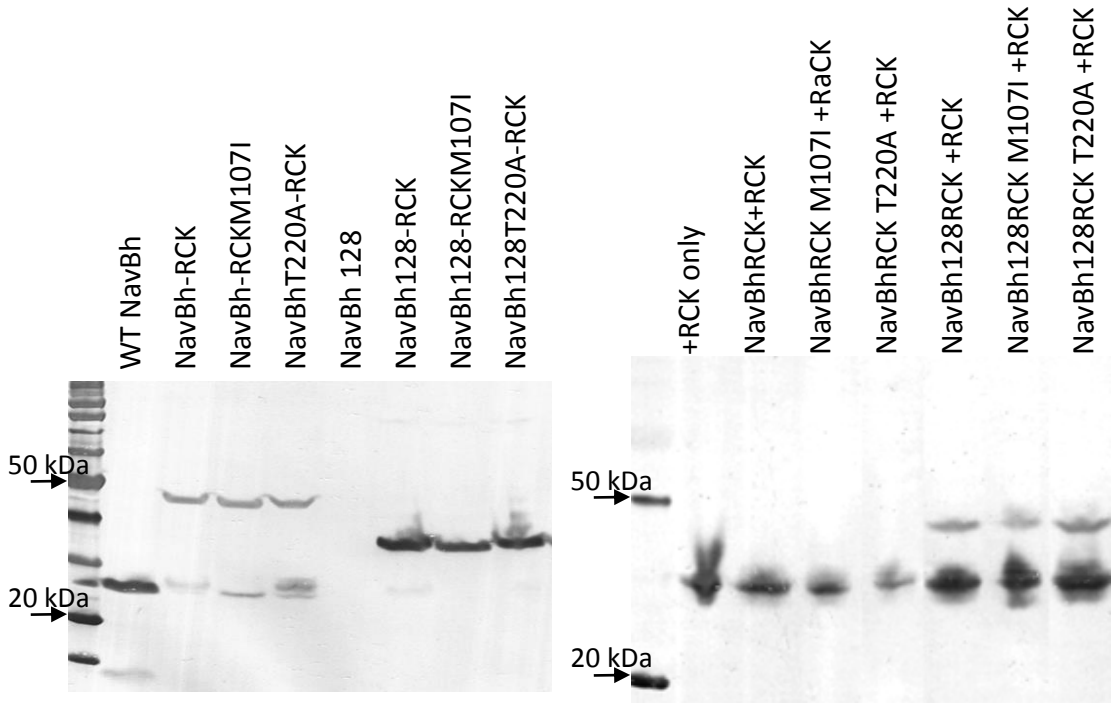

Figure 15: Expression Trials of NavBh-RCK Constructs.
Western blots of whole cell extracts of C41 cells, induced at 37° and grown overnight at 22°. Full length and pore constructs are on the left, on the right are the full length and pore constructs with the soluble RCK domain co-expressed on a separate plasmid.

Attempted concentration of IMAC purified NavBh-RCK resulted in visible precipitation and almost complete loss of the sample. The purified protein demonstrated a maximum concentration of approximately 1 mg/mL. The remainder of the protein precipitated out of solution. Precipitation did not occur during membrane solubilisation, but did occur during IMAC elution and subsequent sample concentration. Multiple conditions were screened (Appendix, Table 4), and it was found that increasing the NaCl concentration to 0.5 M during IMAC elution reduced precipitation in that step, as did elution into a larger volume, resulting in a lower protein concentration. No conditions were identified which allowed for concentration of NavBh-RCK post-IMAC elution above 1-2 mg/mL.

`

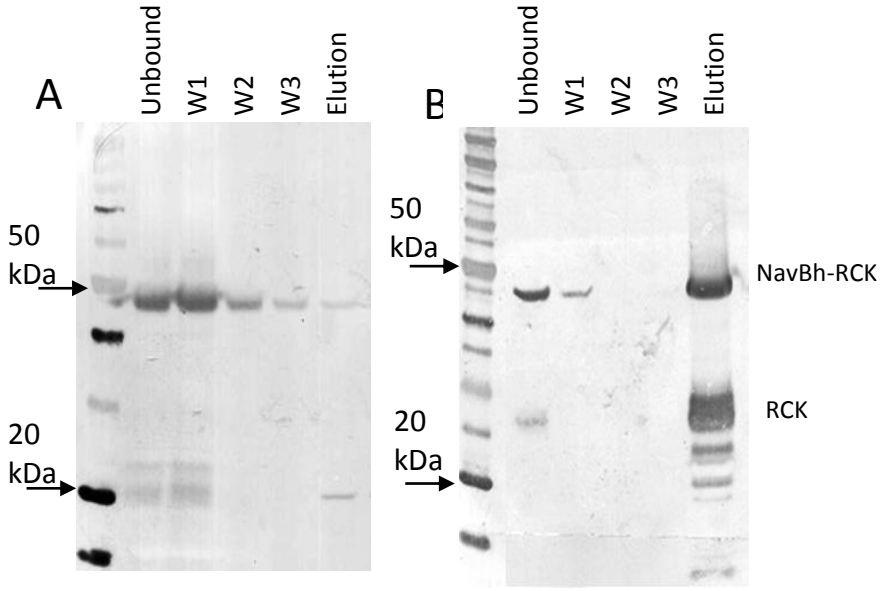

Figure 16: Comparison of Nickel IMAC Purification of N- and C-Terminal Hexahistidine Tagged NavBh-RCK.
Western blots comparing IMAC purification of A) N-terminal hexahistidine NavBh-RCK and B) C-terminal hexahistidine NavBh-RCK. Solubilised membrane was incubated with Ni-NTA resin, 0 mM imidazole for one hour (unbound), washed twice with wash buffer with 0 mM imidazole (w1 and w1), and once with wash buffer with 20 mM imidazole (w3), then eluted in elution buffer, which was wash buffer with 500 mM imidazole (elution). N-terminally tagged NavBh-RCK can be seen as an approximately 50 kDa band in the either in the unbound solubilisation buffer, or to elute from the nickel resin in the first 0 mM imidazole wash. C-terminally tagged NavBh-RCK can be seen as a 50 kDa band and the soluble RCK domain can be seen as an approximately 35 kDa band, both occurring primarily in the elution at 500mM imidazole.

Expression and Purification of NavBh-RCK M107I

MthK had been crystallised using a construct in which the secondary start codon M107, responsible for expressing the soluble RCK domain, was mutated to an isoleucine (Jiang et al. 2002). For the purpose of crystallisation trials, in this study the homologous mutation was introduced in NavBh-RCK. Expression was similar to that of NavBh-RCK, except for the absence of the soluble RCK domain (Figure 15). It should be noted that "M107" was the numbering of the secondary start codon within MthK, and for clarity the numbering from MthK was retained to refer to this residue. NavBh-RCK M107I was found to have the same precipitation and low solubility observed in NavBh-RCK. Crystallisation trials with obtainable concentrations of NavBh-RCK M107I (1-2 mg/mL) were unsuccessful (Appendix, Table 5).

`

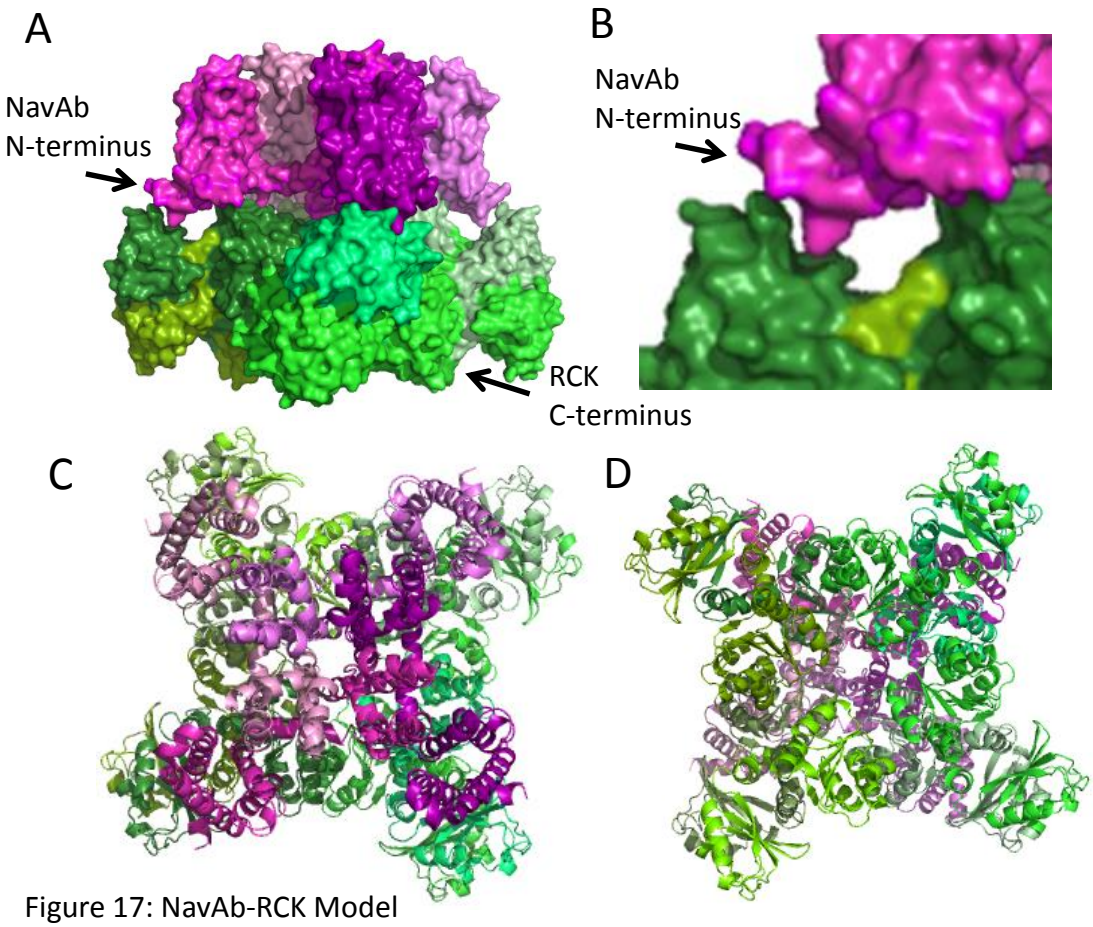

Figure 17: NavAb-RCK Model
A) NavAb-RCK closed pore model, based on the NavAb structure (PBD ID 3RVY) and MthK closed-gating ring structure (PDB ID 2FY8). NavAb is shown in shades of purple, the RCK in shades of green. The chains have been shaded differently in order to differentiate between different subunits. The N- and C- termini of the model have been labelled, in order to demonstrate the position of the hexahistidine tags. B) Zoomed image of the NavAb N-terminus from A. C) View of the NavAb-RCK model from the extracellular surface. D) View of the intracellular surface of NavAb-RCK model, demonstrating alignment of the NavAb voltage sensors over the protrusions of the RCK domain. Images generated in Pymol.

Optimisation of NavBh-RCK and NavBh-RCK M107I Purification

Conditions for efficient purification of NavBh-RCK constructs post-IMAC proved elusive. WT NavBh is known to bind strongly in nickel IMAC, and typically an overnight elution protocol has been used for elution. A similar protocol was used for the chimeric NavBh-RCK constructs as well. This strong binding allowed for highly stringent washing conditions, leaving the sample relatively pure (estimated 80%-95%) after affinity purification (Figure 20, Figure 21). Attempts to concentrate IMAC purified NavBh-RCK and NavBh-RCK M107I in order to load the sample onto a gel filtration column resulted in almost

`

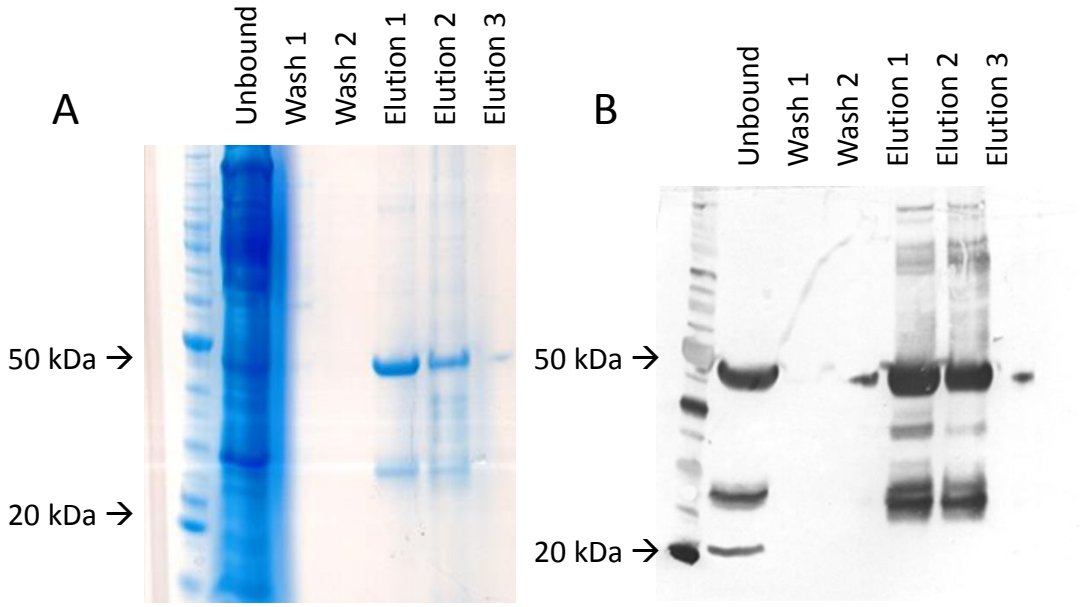

Figure 18: SDS-PAGE and Western Block of IMAC Purification of NavBh-RCK. A)Coomassie blue stained, and B) Western Blot of C-terminally tagged IMAC purified NavBh-RCK. Unbound: solubilised membranes with 80 mM imidazole after one hour rotating incubation with Ni-NTA resin. Wash 1: wash buffer with 40 mM imidazole. Wash 2: wash buffer with 80 mM imidazole. Elution 1-3: serial elutions, one hour rotating incubation each in elution buffer (500 mM imidazole). NavBh-RCK and soluble RCK can be seen at the expected sizes. NavBh-RCK and the soluble RCK domain can be seen either in the unbound fraction, in elutions 1

complete precipitation of the sample with an estimated loss of >95%. This occurred both as pellet formed during concentration, and as further precipitation during gel filtration. As can be observed from gel filtration profiles, the largest peak was present in the column void volume (approximately 7.5 mL), and precipitated protein was visible in the corresponding fractions (Figure 21). Several smaller broad peaks were present throughout the gel filtration profile. This suggested that the channel-RCK complex existed in multiple oligomeric forms. This wasn't unexpected, as the soluble RCK domain is known to dynamically form homo-dimers, homo-tetramers, homo-hexamers, and homo-octomers, in addition to forming the functional octomeric gating ring with the pore-RCK subunits (Kuo et al. 2007). Altering the buffer pH had no observable effect on protein solubility, however at pH 8 the presence of calcium did cause the soluble RCK domain to co-elute with full length NavBh-RCK (Figure 21). This was not unexpected as pH is known to modulate the calcium controlled

`

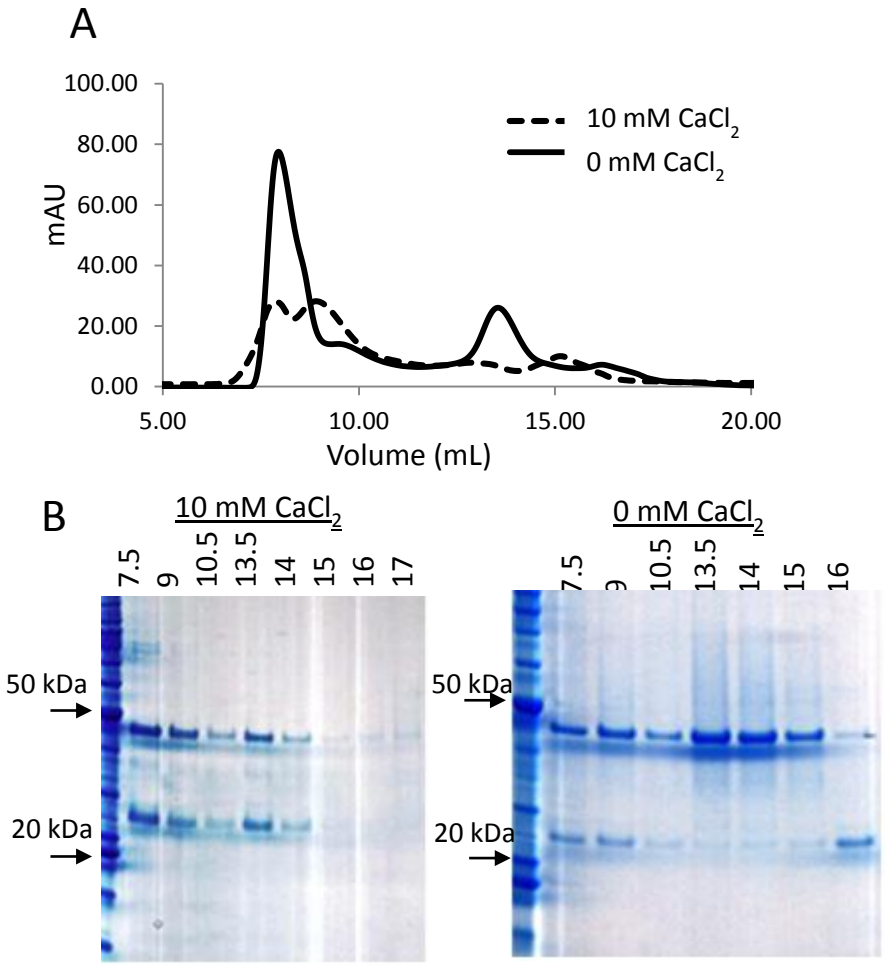

Figure 19: Comparison of NavBh-RCK Gel Filtration With and Without $CaCl_2$.
A) Gel filtration of NavBh-RCK in 20mM Tris pH 8, 0.5 M NaCl, 0.25% CYMAL5, in the presence and absence of 10 mM $CaCl_2$, on a Superdex 200 10/100 gel filtration column. B) Corresponding SDS-PAGE gels, showing NavBh-RCK and the soluble RCK domain at the expected sizes, lanes are labelled with matching volumes from A).

oligomerisation of the soluble RCK domain. This effect has been well characterised for the soluble RCK domain (Kuo et al. 2007; Dong et al. 2005), however has never been investigated in detergent solubilised full length MthK. Neither the addition of calcium nor the presence of EDTA nor EGTA prevented the visible precipitation, or increased protein solubility. In the absence of calcium, a peak can be seen in the gel filtration profile at 13.5 mL, corresponding to approximately 10 0kDa based upon column standards (appendix, Figure 48). As the column standards available were soluble proteins which don't account for the detergent micelle, this this should produce an overestimation of the mass of the protein. As such, this s to a monomer or dimer of NavBh-RCK, as SDS-PAGE analysis revealed a lack of soluble RCK in this fraction (Figure 21B). This peak was seen to shift to approximately 9 mL in the

`

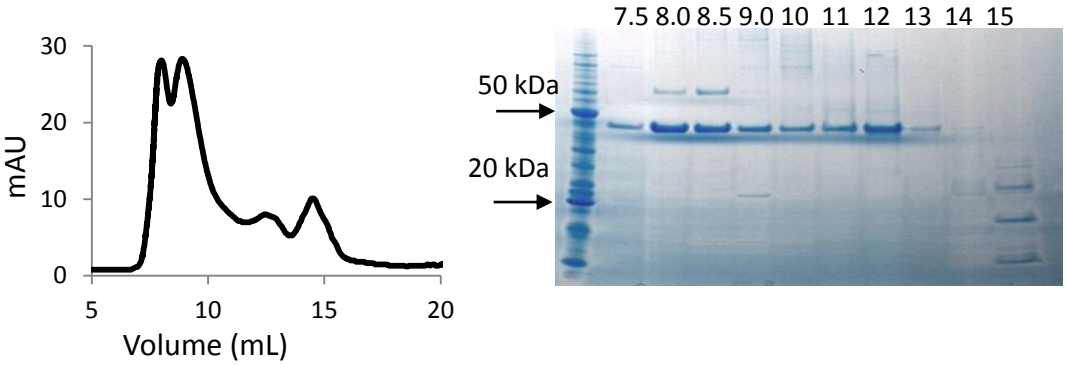

Figure 20: Gel Filtration of Ni IMAC Purified and Concentrated NavBh-RCK M107I pH 7.8, 0 mM $CaCl_2$.

Gel filtration profile of Ni IMAC purified NavBh-RCK M107I, and corresponding SDS-PAGE gel. Run on a Superdex 200 10/300 gel filtration column, in 20 mM sodium phosphate, 500 mM NaCl, 0.25% cymal5. The leftmost peak corresponds to the column void volume of approximately 8 mL. NavBh-RCK can be observed by SDS-PAGE, at the expected size of just under 50 kDa, in fractions between 7.5 mL, and 13 mL.

presence of calcium, which while not in the void volume is outside the practical separation range of the Superdex 200 10/300 column. This may correspond to an octomeric configuration, which has a predicted molecular weight of 324 kDa without the detergent micelle. However, given that the extrapolated size based on column standards is approximately 800 kDa, it is more likely this peak corresponds to soluble aggregate. The larger peak seen in the void volume was attributable to precipitation during gel filtration, and there was no indication that it corresponded to any change in protein solubility, as the absorbance remained in the same range. Additional concentration following gel filtration resulted in complete loss of the remaining sample

`

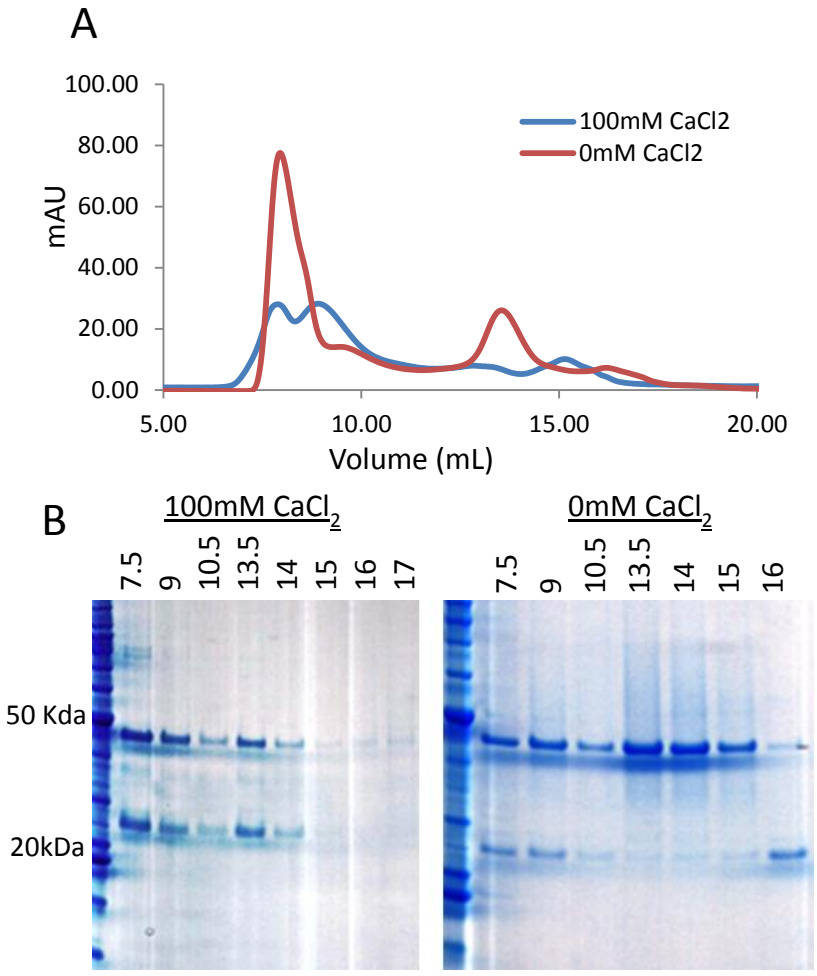

Figure 21: Comparison of NavBh-RCK Gel Filtration With and Without $CaCl_2$. Comparison of NavBh-RCK gel filtration, with and without $CaCl_2$. in 20mM Tris pH 8, 0.5M NaCl, 0.25% CYMAL5. A) Gel filtration. B) Corresponding SDS-PAGE gels.

. Purifications of NavBh-RCK M107I gave similarly low yields (Figure 23), with the majority of the protein lost to precipitation during concentration. NavBh-RCK M107I had a similar gel filtration profile to NavBh-RCK, with a large peak eluting around 9 mL, and several smaller disperse peaks at later volumes (Figure 23). This indicated that despite the previously reported stable formation of the soluble octomeric RCK ring at pH 8, NavBh-RCK oligomerisation remains dynamic even at alkaline pH without the addition of calcium. Despite the large amount of work investigating oligomerisation of the soluble RCK domain, no studies have been published on the oligomerisation of the full length MthK channel. Thus, without access to WT MthK for use as a control, it was difficult to determine whether the effects observed here were an intrinsic property of the RCK domain when attached to any channel, or whether the behaviour was a result of the chimeric nature of NavBh.

`

Comprehensive detergent screening of wild type NavBh has previously been performed within the Wallace lab, both for the full length and the NavBh128 pore constructs in which the S1-S4 helices have been removed. Only minor differences were identified, with membrane solubilisation in DDM and then detergent exchange into CYMAL5 during IMAC being the best performing (A. Powl, personal communication). The four detergents known to work best with NavBh: CYMAL5, LDAO, DDM, and DM, have been tested with the NavBh-RCK construct, with no improvement in solubility of the purified protein (Table 1). As NavBh-RCK does not have a modified hydrophobic transmembrane region, this was unsurprising. Previous detergent screening by the Wallace Lab has demonstrated that shorter chain detergents (NM or shorter) are not suitable for maintaining WT NavBh in a soluble form, further limiting detergent choice. Precipitation occurred primarily during protein concentration, which further suggested that lipid depletion was unlikely a key factor. Furthermore, identical purification conditions are known to not result in the precipitation of WT NavBh, which suggested that it is a property of the RCK domain that results in the low solubility of NavBh-RCK.

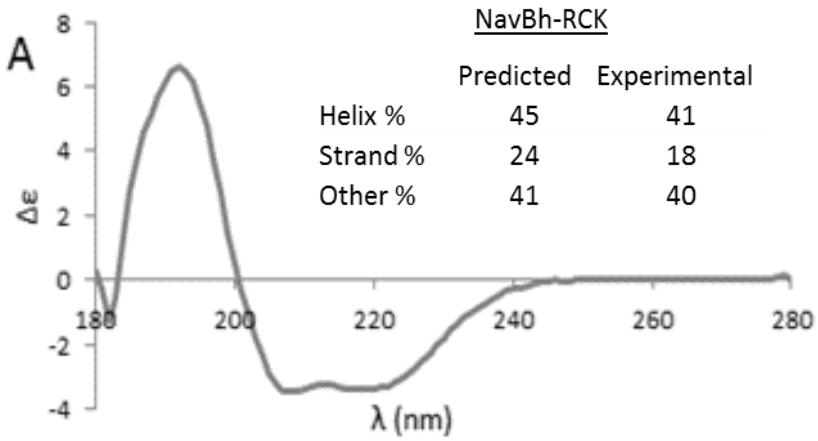

Figure 22: SRCD Spectra of NavBh-RCK.
A) SRCD spectra and secondary structure deconvolution of NavBh-RCK. B) Predictions for the expected secondary structure of NavBh-RCK based on the SRCD measurements of truncated NavBh (Powl et al., 2010) and 2Struct analysis of RCK closed octomer (PDBID# 2FY8) and the full length MthK structure with pore removed (PDBID# 3RBZ)

4.3 SRCD Spectroscopy of NavBh-RCK

As previously discussed CD spectroscopy is a technique which allows for the determination of the secondary structure of a protein, and is frequently used as a tool to confirm protein folding of a recombinantly expressed protein (see chapter 2.3). In

`

the case of NavBh-RCK, it was important to confirm that the chimera was correctly folded, as

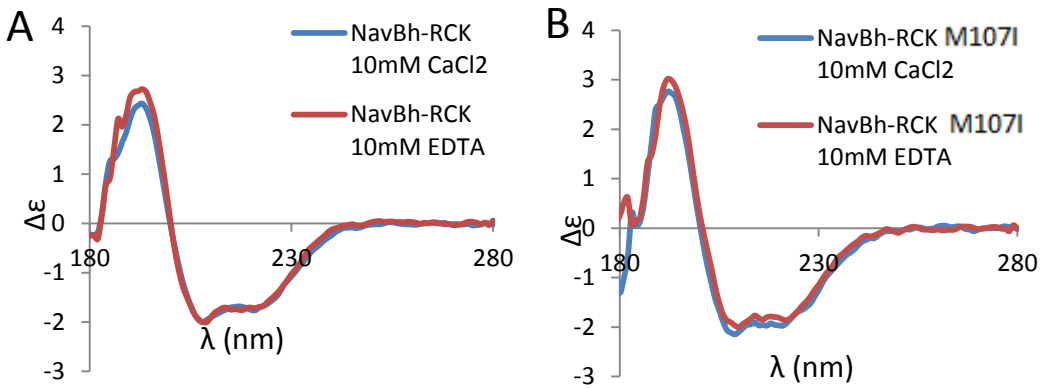

C

	NavBh-RCK 10mM $CaCl_2$	NavBh-RCK 10mM EDTA	Change	NavBh-RCK M107I 10mM $CaCl_2$	NavBh-RCK M107I 10mM EDTA	Change
helix %	18.4	18.6	0.2	18.6	18.9	0.3
sheet %	30.4	31.6	1.2	30	30.9	0.9
other %	51.2	49.6	1.3	51.4	50.5	0.9

D

	Open Gating ring	Closed Gating Ring	Δ
Helix %	38.3	37.1	1.2
Sheet %	21.7	20.3	1.4
Other%	39.9	42.6	2.7

Figure 22 : SRCD Analysis of NavBh-RCK and NavBh-RCK M107I in the Presence of $CaCl_2$ and EDTA.

A) SRCD spectra of Ni Affinity purified NavBh-RCK in the presence of 10 mM CaCl2 or 10 mM EDTA. B) SRCD spectra of Ni affinity purified NavBh-RCK M107I in the presence of 10 mM Calcium or 10 mM EDTA. C) Secondary structural percentages of spectra in A and B. D) Secondary structure percentages from crystal structures of the soluble MthK RCK domain with and without calcium bound, PDB IDs 2AEF and 2AEJ. Images generated in Pymol.

incorrect folding could have caused precipitation. Previous work determined the secondary structural percentages of hexahistidine tagged NavBh via CD and SRCD spectroscopy (Powl et al. 2010; Nurani et al. 2008), and the crystal structures of the open and closed RCK domains were available. This enabled calculation of the expected secondary structural percentages of the NavBh-RCK chimera (Figure 22B). It should be kept in mind that with the secondary start codon intact the sample consisted of an unknown ratio of NavBh-RCK and soluble RCK domains, and due to the precipitation problems of the chimera, the soluble domain may be overrepresented in the sample.

`

SRCD measurements and deconvolution via the DichroWeb server (Whitmore & Wallace 2004) indicate that NavBh-RCK had a slightly lower than expected helical content of 41%, as compared to the expected 44.7% for the NavBh-RCK with a 1:1 ratio of soluble RCK. This deviation from the expected helical content was likely a result of the unknown ratio of soluble RCK domain to full length NavBh-RCK, as the RCK domain

In order to further examine the effects of calcium on NavBh-RCK, SRCD was employed to determine whether calcium binding had any effect on the protein's secondary structure. Analysis of the calcium bound and calcium free RCK domain structures showed only minor differences between the two (Figure 22C). If NavBh disruption by the formation or activation of the RCK gating ring contributed to channel precipitation, it may have been detectable by SRCD.

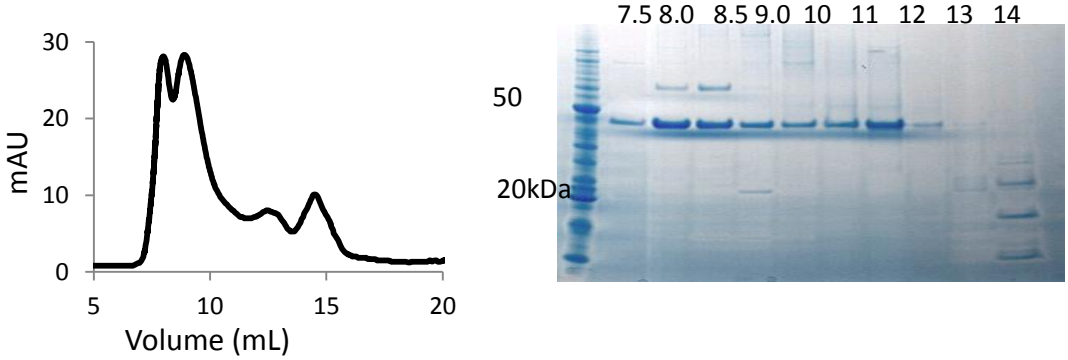

Figure 23: Gel Filtration of Ni IMAC Purified and Concentrated NavBh-RCK M107I pH 7.8, 0mM $CaCl_2$.
Gel filtration profile of Ni IMAC purified NavBh-RCK M107I, and corresponding SDS-PAGE gel. Run on a Superdex 200 10/300 gel filtration column, in 20mM Sodium phosphate, 500mM NaCl, 0.25% CYMAL. The leftmost peak corresponds to the column void volume of approximately 8mL. NavBh-RCK can be observed by SDS-PAGE, at the expected size of just under 50kDa, fractions between 7.5mL, and 13mL.

SRCD of NavBh-RCK in EDTA and in $CaCl_2$ did not demonstrate any large changes in secondary structural percentages with and without $CaCl_2$, either for NavBh-RCK or for NavBh-RCK M107I (Figure 22A).

While the expected secondary structural percentages for the NavBh chimera could be calculated, the unknown ratio of NavBh-RCK to soluble RCK prevented accurate calculations of the expected CD spectrum. Thus the experiment was also repeated with NavBh-RCK M107I (Figure 23B). No large differences in secondary structure were observed between NavBh in the presence the $CaCl_2$ and EDTA. Had a drastic change in channel secondary structure occurred, it would have suggested a possible cause of channel precipitation, as previous CD studies of the soluble RCK

`

domain found no significant difference in spectra with and without $CaCl_2$ (Dong et al. 2005). Calcium binding has however been shown to increase protein stability in low concentrations of urea (Dong et al. 2005).

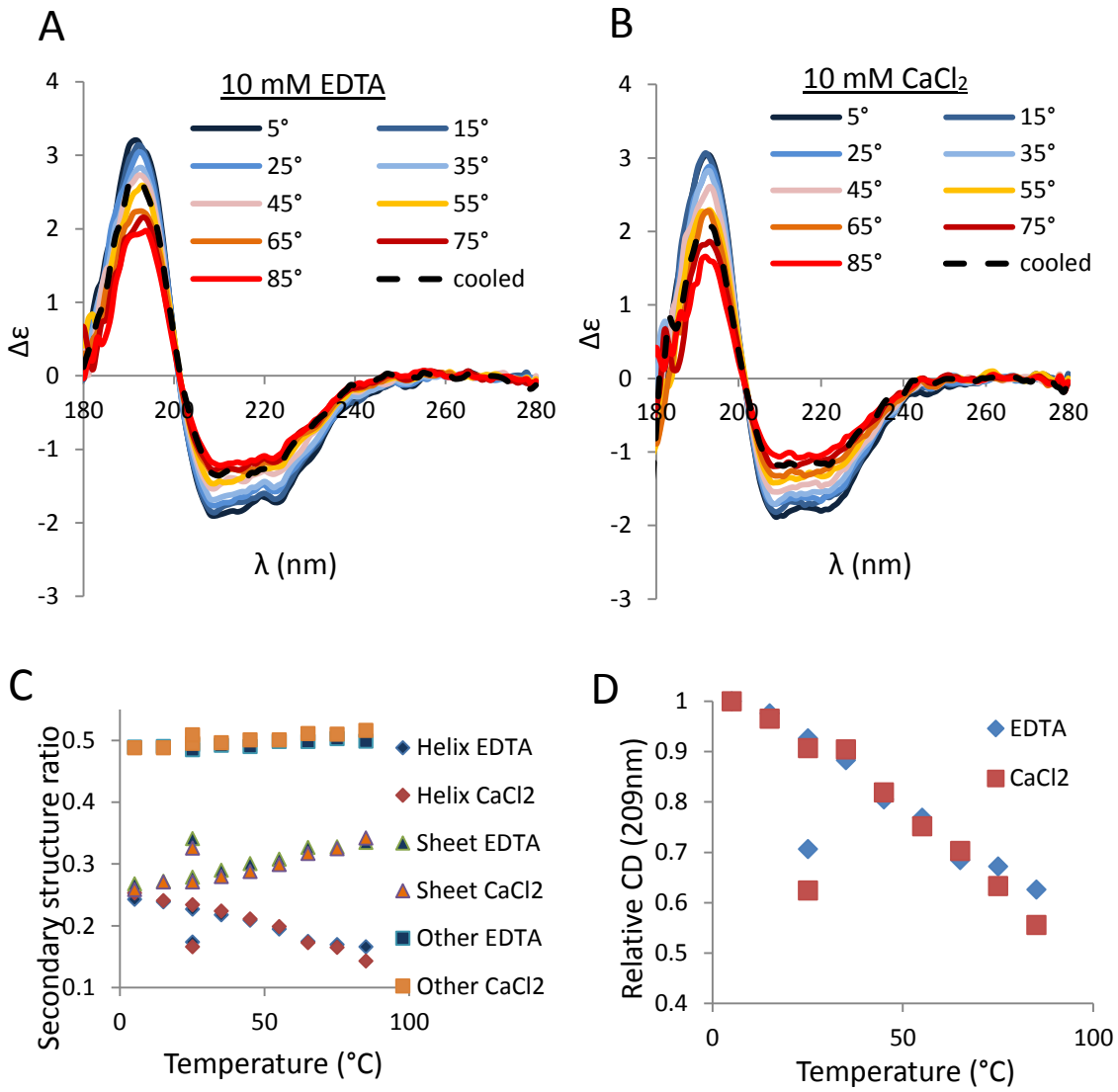

Figure 24: Thermal Denaturation SRCD of NavBh-RCK M107I in the Presence and Absence of $CaCl_2$.
Thermal denaturing SRCD of 2mg/mL NavBh-RCKm107i in the presence of A) 10mM EDTA and B) 3mM $CaCl_2$. C) Secondary structure percentages of spectra in A and B. D) Relative CD signal at 209nm of NavBh-RCK M107I.

In order to determine if increased stability can also be detected in NavBh-RCK, thermal unfolding SRCD spectroscopic studies of NavBh-RCK M107I were performed in the presence of 10 mM EDTA and 10 mM $CaCl_2$ (Figure 24). At >75°C NavBh-RCK M107I retained less helicity in the presence of calcium (Figure 24D). This suggested that unlike the soluble RCK domain, NavBh-RCK M107I was less stable in the presence of calcium. This corresponded with a sharper increase in the high tension (HT) between

`

180 nm-190nm (appendix- Figure 49), which indicates an increased signal absorption, possibly due to precipitation.

4.4 Crystallisation Trials of Low-Concentration NavBh-RCK and NavBh-RCK M107I

Crystal screens were set up at 3.2 mg/mL, the highest concentration achieved. Given the low solubility, it was possible that the NavBh-RCK would crystallise at low concentrations. However, no crystals were observed under any of the conditions tested (appendix, Table 4).

4.5 Electrophysiology of NavBh-RCK

While the primary objective of the NavBh-RCK project was to obtain a crystal structure, a ligand gated sodium channel also had the potential to be a very useful tool for the characterisation of drug binding. Additionally, as the fusion chimera combined domains from different ion channels, showing that it was a functional channel would have been necessary for demonstrating the relevance of any structural data. As such, electrophysiological characterisation of NavBh-RCK in synthetic lipid bilayers was performed in collaboration with the de Planque group at the University of Southampton (see chapter 2.3 for a review of electrophysiology in synthetic lipid bilayers). NavBh-RCK purified by affinity chromatography was resuspended in 1:1 1-palmitoyl-2-oleoyl-sn-glycero-3-phosphoethanolamine (PE) : 1-palmitoyl-2-oleoyl-sn-glycero-3-phospho-(1'-rac-glycerol) (PG) lipid vesicles, as previously described for NavBh (Powl et al. 2012) and allowed to fuse with a 1:1 PE/PG lipid bilayer suspended in a vertical microaperture (Kalsi et al. 2013; Kalsi et al. 2014).

After the addition liposome reconstituted NavBh-RCK, baselines were observed at a variety of holding potentials for 30 minutes prior to the addition of $CaCl_2$. In all recordings, no activity was observed prior to the addition of $CaCl_2$ (data not shown). In the presence of 10 mM $CaCl_2$ at pH 8 the channel is active, (Figure 25). Gating events of 5-6 pA were observed at holding potentials of 125 mV and -125 mV. Channel activity was characterised by long periods of inactivity, interrupted by short periods of rapidly repeating, short lived gating events, with stretches of activity lasting 30-60 seconds. This unpredictability made reproducing the results problematic, as the experimental setup was not quickly and easily repeatable. No activity was observed in hour long trials at pH 7.2 or pH 7.6, in up to 25 mM $CaCl_2$ (data not shown) nor was

`

activity observed in the presence of 5 mM mibefradil (sodium channel blocker) + 25 mM $CaCl_2$, pH 8 over the course of an hour recording (data not shown).

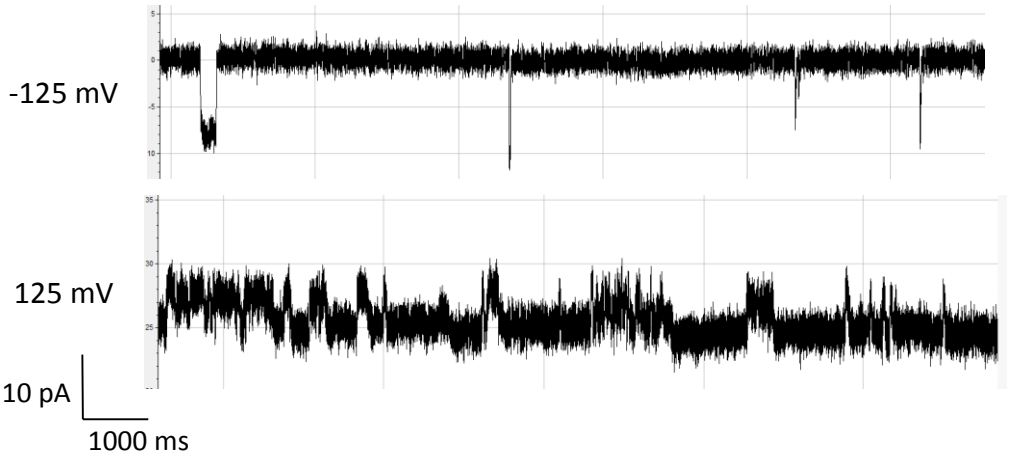

Figure 25: Electrophysiology of NavBh-RCK in a Synthetic Lipid Bilayer. Single Channel recordings of proteoliposome reconstituted, affinity purified NavBh-RCK in PE:PG bilayers suspended in a microaperture, at -125 mV and 125 mV. Measurements made in 20 mM Tris, 0.5 M NaCl, pH 8.0, with 10 mM $CaCl_2$ added after 30 minutes of baseline recordings to confirm absence of activity.

In the same system the NavBh128 pore was characterised by short, single burst opening events attributable to channel breathing motion, resulting in a very low open probability (Figure 7). WT NavBh displayed a conductance of 5-6 pA, similar to that of NavBh-RCK. WT MthK gating was reported to be characterised by long stretches of activity in which the RCK gating ring actively holds the channel in an open configuration (Li et al. 2007). During these longs stretches of activity there were multiple rapid opening and closing events due to inactivation by the pore. This was similar to was stretches of activity observed in this study, with rapid opening and closing events in recordings of NavBh-RCK at 125 mV.

Despite the low solubility of NavBh-RCK, electrophysiological characterisation confirmed that NavBh-RCK was active at an alkaline pH in the presence of $CaCl_2$. No channel activity was observed in the absence of $CaCl_2$, at pH less than 8, or in the presence of mibidefridil. However, it was difficult to attribute this lack of activity to calcium dependent gating, rather than the absence of channel fused with the lipid bilayer, as the system lacked the capability to monitor channel fusion. NavBh-RCK displayed conductance and inactivation characteristic of NavBh, and the calcium and pH dependences as well as the extended gating events that were characteristic of the RCK domain. This suggested that NavBh-RCK is a calcium gated sodium channel, but

`

would have required further confirmation given the low reliability of channel activity, should these constructs have been pursued for other structure/function studies.

4.6 Expression and Purification of NavBh128-RCK

One possible cause of the precipitation and low solubility of NavBh-RCK was steric hindrance between the intracellular loops in the S1-S4 helices, and the RCK domain. The NavAb-RCK model did exhibit any overlap between the NavAb loops and the RCK domain (Figure 17). Interactions between the RCK domain and the intracellular loops of the voltage sensor have previously been demonstrated in the BK channel (Yuan et al. 2010), the one example of a channel with both a native voltage sensor and an RCK domain. Furthermore, in the absence of a voltage pulse protocol, the voltage sensor was expected to hold the channel in a closed conformation, and so its removal should promote channel activity.

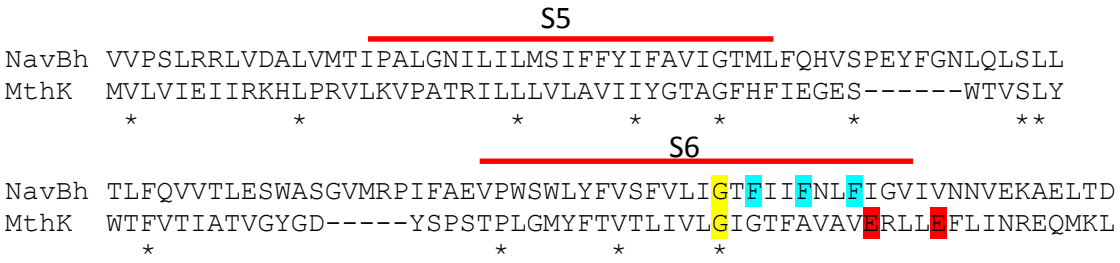

Figure 26: Sequence Alignment of MthK and NavBh.
Clustal Omega sequence alignment of MthK and NavBh pores. The conserved glycine hinge residue is highlighted in yellow, phenylalanine residues forming the hydrophobic blockage in NavBh are highlighted in blue, and the glutamate residues forming the narrowest part of the pore in MthK are highlighted in red.

In order to investigate this hypothesis, a NavBh-RCK construct was generated without the first 128 residues of NavBh, which contain the voltage sensing S1-S4 helices (Figure 14). This construct has been designated NavBh128-RCK. This approach was previously used to express pore-only constructs of the prokaryotic sodium channels NavSp, NavMs, and NavAe (McCusker et al. 2011; McCusker et al. 2012; Shaya et al. 2014), and in the cases of the NavMs and NavAe pores this lead to crystal structures. Furthermore, a pore-only NavBh better mimics the WT MthK channel, which is not voltage gated. Previous work within the Wallace lab demonstrated that expression of the NavBh pore was possible (A. Powl, unpublished results). NavBh was found to be particularly sensitive to where within the S4-S5 linker the truncation occurred, with 128 being the best expressing construct. Therefore this site was chosen

`

to make a pore-only construct for NavBh–RCK, hereafter referred to as NavBh128-RCK.

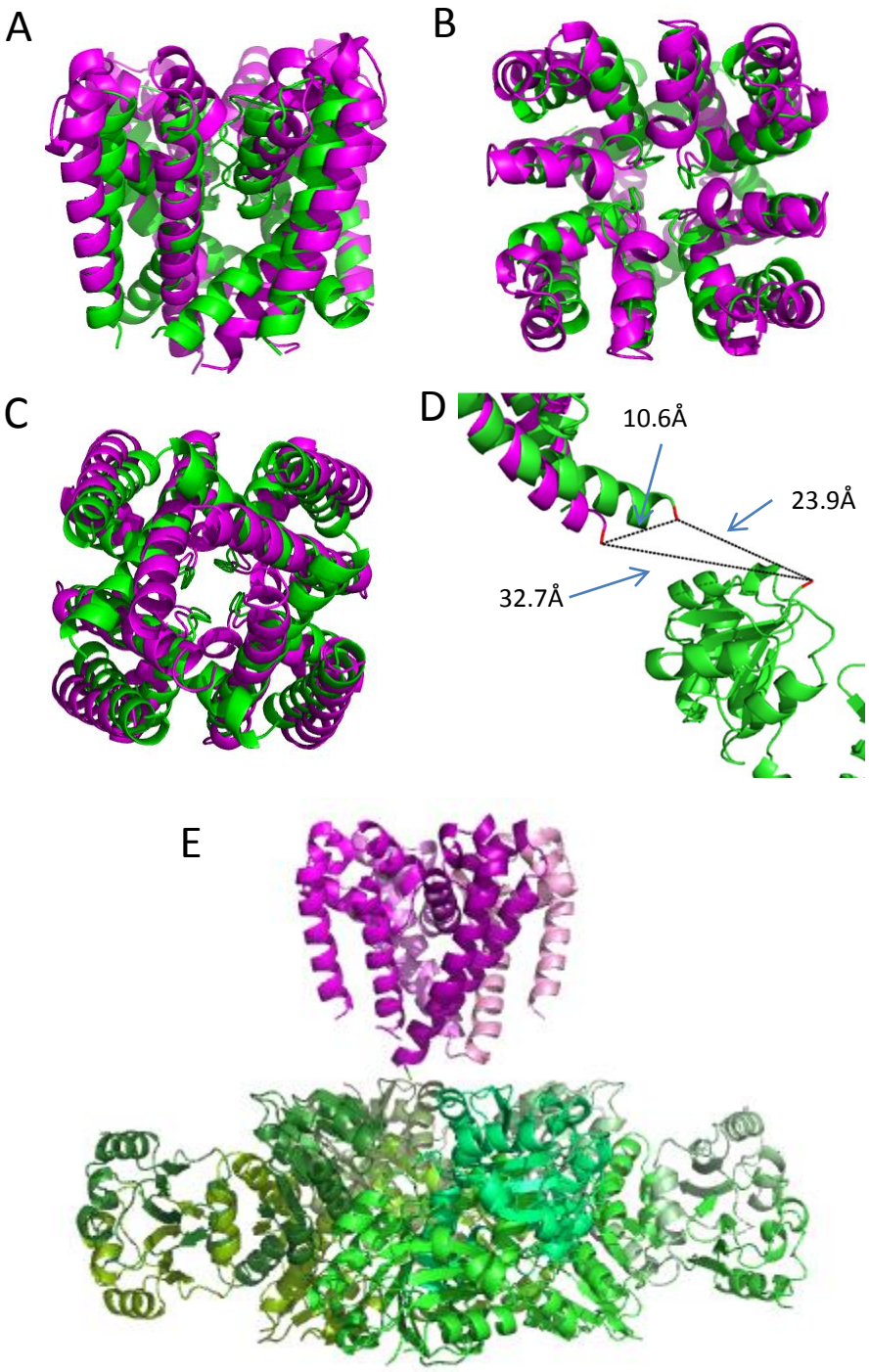

Figure 27: Mthk and NavMs Pore Structural Alignment, and NavMs-RCK Model. Structural alignment of the open NavMs pore (purple, PDB ID 3ZJZ), with the open MthK Pore (green, PDB ID 3RBZ). A) Side view, B) Top-down view, C) bottom up view. D) Measurements of difference in the position of the end of aligned the MthK M2 helix and NavMs S6 helix, and their distance from the first resolved residue of the RCK domain. E) Structural model in which the MthK pore has been replaced by the aligned NavMs pore. Images generated in Pymol.

`

Structural Alignment of NavBh128-RCK and MthK

Sequence alignment of NavBh and the MthK pore offered insights into their differences (Figure 26). The pores of MthK and NavBh had approximately 10% identity, and the transmembrane regions were better conserved than the linker regions. The glycine hinge at which the MthK M2 helix (homologous to the Nav S6 helix) bends was conserved in NavBh, although this wasn't true in the majority of other prokaryotic sodium channels. In MthK, two glutamate residues form the constricting point of the pore, whereas in NavBh a hydrophobic blockage formed of several stacked phenylalanine residues is responsible for channel constriction (Barber et al. 2012).

The crystal structure of the NavMs pore in an open conformation allowed for a retroactive comparison of the MthK pore and an open Nav pore (Figure 27). Superposition of the NavMs and MthK pores demonstrated that the structures do not align well at the end of the S6 helix. In MthK the pore was opened by a bend at the glycine hinge, while in NavMs channel opening was seen to be the result of a rotation of the S6 helices. A difference of approximately 10 Å between the ends of the MthK M2 helix and the homologous NavMs S6 helices was observed (Figure 27e). This translated to a difference of 8.8 Å between the end of the S6 helix and the homologous helix in MthK, and their respective distances to first resolved N-terminal residue in the structure of the covalently bound RCK domain. This difference in position of the end of the last transmembrane helix showed that MthK opens much wider than NavMs. As the RCK domain provided the force to open the channel, it was plausible that binding of calcium to the RCK domain of NavBh-RCK would result in the RCK domain forcing the NavBh S6 helix into a conformation more like that seen in the MthK open pore. This information was not, however, available at the time of the majority of the work on NavBh-RCK.

Expression and Purification of NavBh128-RCK

Expression of NavBh128-RCK was successful, with expression levels lower than the full length NavBh-RCK, but more than WT NavBh128 (Figure 15). NavBh128-RCK also exhibited less expression of the soluble RCK from the second start codon. While the WT NavBh128 construct was the best expressing of the tested truncations, expression was still poor as compared to the wild type NavBh (A. Powl, personal communication). As such, poor expression of the NavBh128-RCK was not unexpected.

`

Purification of NavBh128-RCK was similar to that of the full length. The same high-stringency elution protocol was required for efficient elution during IMAC, and precipitation and loss of the sample during subsequent concentration remained a problem. This demonstrated that interaction between the S1-S4 loops and the RCK domain was not a causal factor in the precipitation of NavBh-RCK.

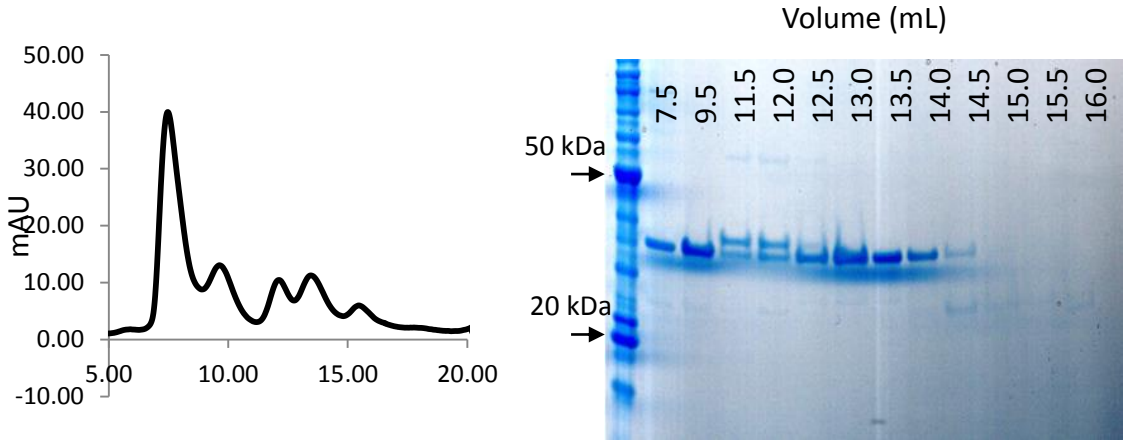

Figure 28: Gel Filtration of NavBh128-RCK.
Gel filtration profile and corresponding coomassie stained gel of IMAC purified NavBh128-RCK, in 20 mM sodium phosphate, pH 8, 0.5 M NaCl. NavBh128-RCK can be seen at the expected size of approximately 35 kDa, but elutes in multiple fraction. The large bar at approximately 30kDa was an artefact of scanning, and was not present on the physical gel.

The gel filtration profile of NavBh128-RCK was similar to that of the full length protein in scale, although the NavBh128-RCK construct appeared in multiple peaks (Figure 28). This is likely due to inconsistent oligomerisation, and the dynamic nature with which the RCK gating ring associates, but could also be due to the low concentration of the RCK domain resulting in a much lower probability of the channel forming the octomeric complex.

4.7 Electrophysiology of NavBh128RCK

Affinity purified samples of NavBh128-RCK were characterised, utilising the same method previously described for the full length NavBh-RCK. At pH 7.4, no activity was detected in the presence of up to 25 mM $CaCl_2$. At pH 8.4 the channel displayed conductance comparable to the full length NavBh-RCK, and to WT NavBh and NavBh128 (Figure 29). Similar to the full length NavBh-RCK, channel activity was intermittent, characterised by bursts of activity lasting 30 seconds to several minutes. NavBh128-RCK was nominally more active than NavBh-RCK, but still low enough to

`

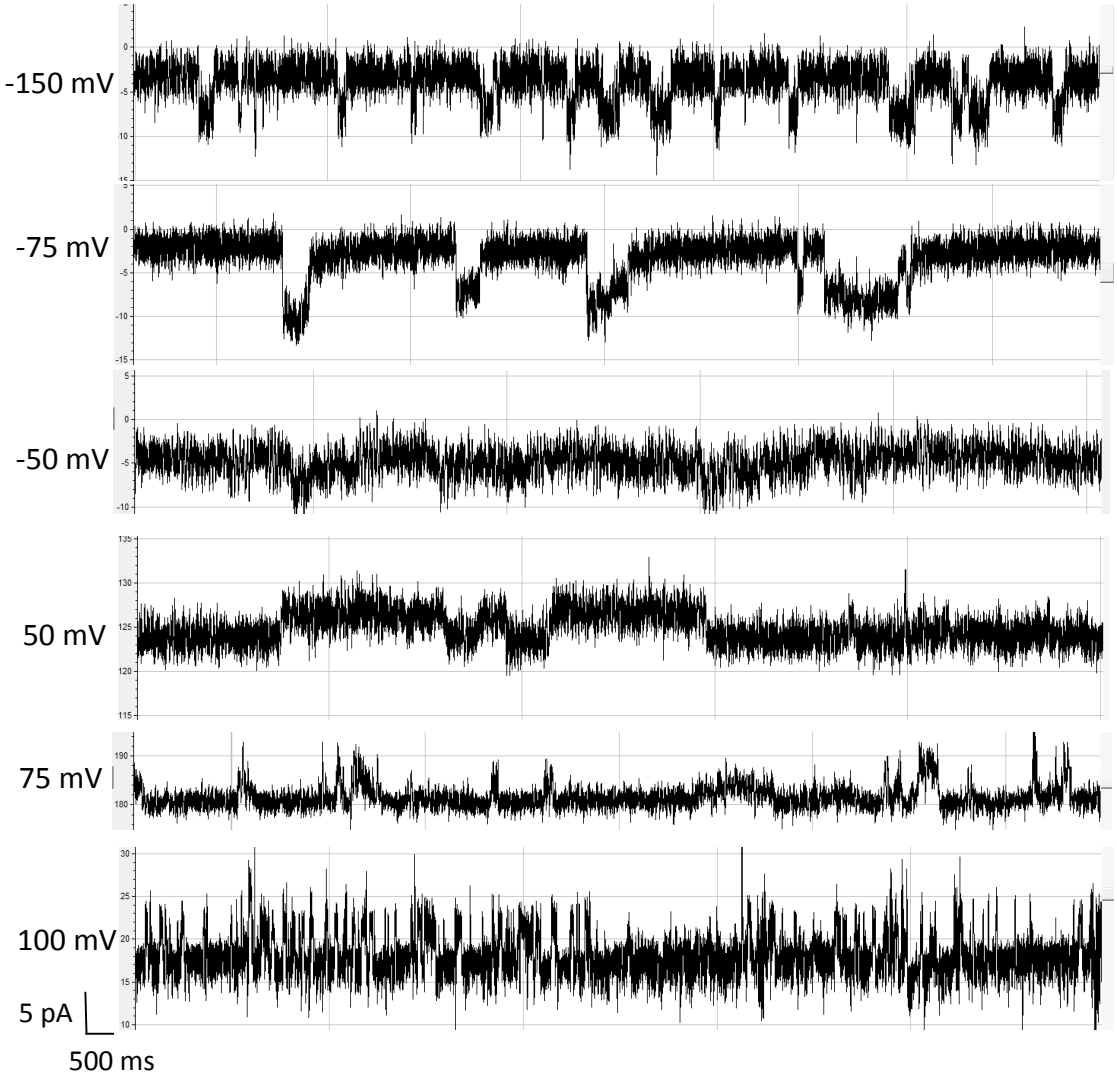

Figure 29: Electrophysiology of NavBh128-RCKK in a Synthetic Lipid Bilayer. Single channel recordings of proteoliposome reconstituted, IMAC purified NavBh128-RCK in PE:PG bilayers suspended in a microaperture, at the indicated voltages.

make calculating a significant P_o impractical. The addition of more proteoliposome reconstituted channel did seem to promote activity, but also led to a destabilisation of the lipid bilayer and irregular channel conductance (data not shown). The increased activity of the NavBh128-RCK as compared to NavBh-RCK suggested that removal of the voltage sensor improved channel activity. However, the soluble RCK domain expressed poorly in the NavBh128-RCK construct (Figure 15). This was compounded by its further dilution, as the experiments required that 5-20 µL of proteoliposomes (along with the soluble RCK domain) were diluted into 1 mL of buffer. The approximate 200 fold dilution of the unbound, soluble RCK domain could have prevented reliable formation of the octomeric gating ring, given its low initial concentration due to its poor expression. This may have been why channel activity

`

remained unreliable. Why the expression of the soluble RCK domain was reduced by the removal of the voltage sensor was unclear, however this hypothesis was easily addressed by co-expression of the soluble RCK domain.

4.8 Co-Expression of NavBh128-RCK Constructs With the Soluble RCK Domain

In order to improve electrophysiological recordings of NavBh-RCK and NavBh128-RCK, a construct consisting of only the soluble RCK domain was generated in a modified pET15B vector, containing a kanamycin resistance gene (Figure 14). The construct was then co-transformed with NavBh-RCK M107I or NavBh128-RCK M107I. The full length NavBh-RCK did not co-express with the soluble RCK domain, but the NavBh128-RCK did co-express with a visible excess of soluble RCK domain produced (Figure 15) Purifications were similar to the previously discussed NavBh-RCK purifications. SDS-PAGE and western blotting of IMAC purified NavBh128-RCK M107I+RCK demonstrated that the soluble co-expressed RCK domain co-purified with the membrane bound pore, and co-eluted with the NavBh128-RCK despite the high stringency washing conditions required for NavBh-RCK (Figure 30A). The precipitation and low solubility of the protein was not improved by co-expression of the soluble RCK domain. During gel filtration the excess soluble RCK domain migrated in multiple

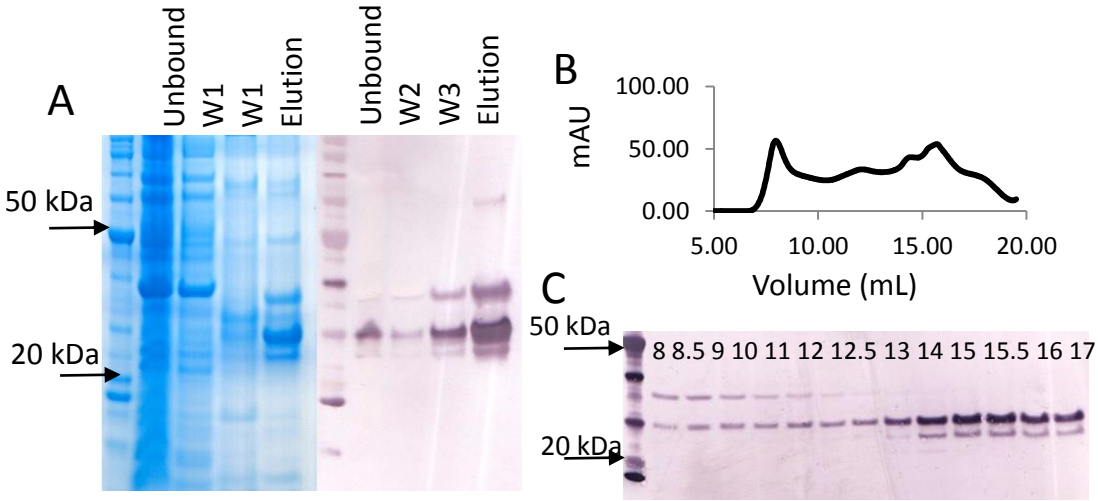

Figure 30: Purification of NavBh128-RCK M107I Co-Expressed With Soluble RCK. A) Coomassie stained PAGE (left) and anti-his western (right) blot of Ni IMAC purified NavBh128-RCK M107I + RCK. Unbound consists of solubilised membranes after one hour incubation with Ni-NTA resin. W1: wash buffer with no imidazole, W2: wash buffer with 100 mM imidazole, Elution: elution buffer with 500 mM imidazole. B) Gel filtration profile of concentrated IMAC purified protein from A. C) Anti-his western blot of gel filtration fractions.

`

oligomeric forms, eluting in widespread peaks between 12ml and 17ml (Figure 30B). This demonstrated that under these conditions (excess soluble RCK, pH 8, 0 mM $CaCl_2$) oligomerisation of the soluble RCK domain was unstable.

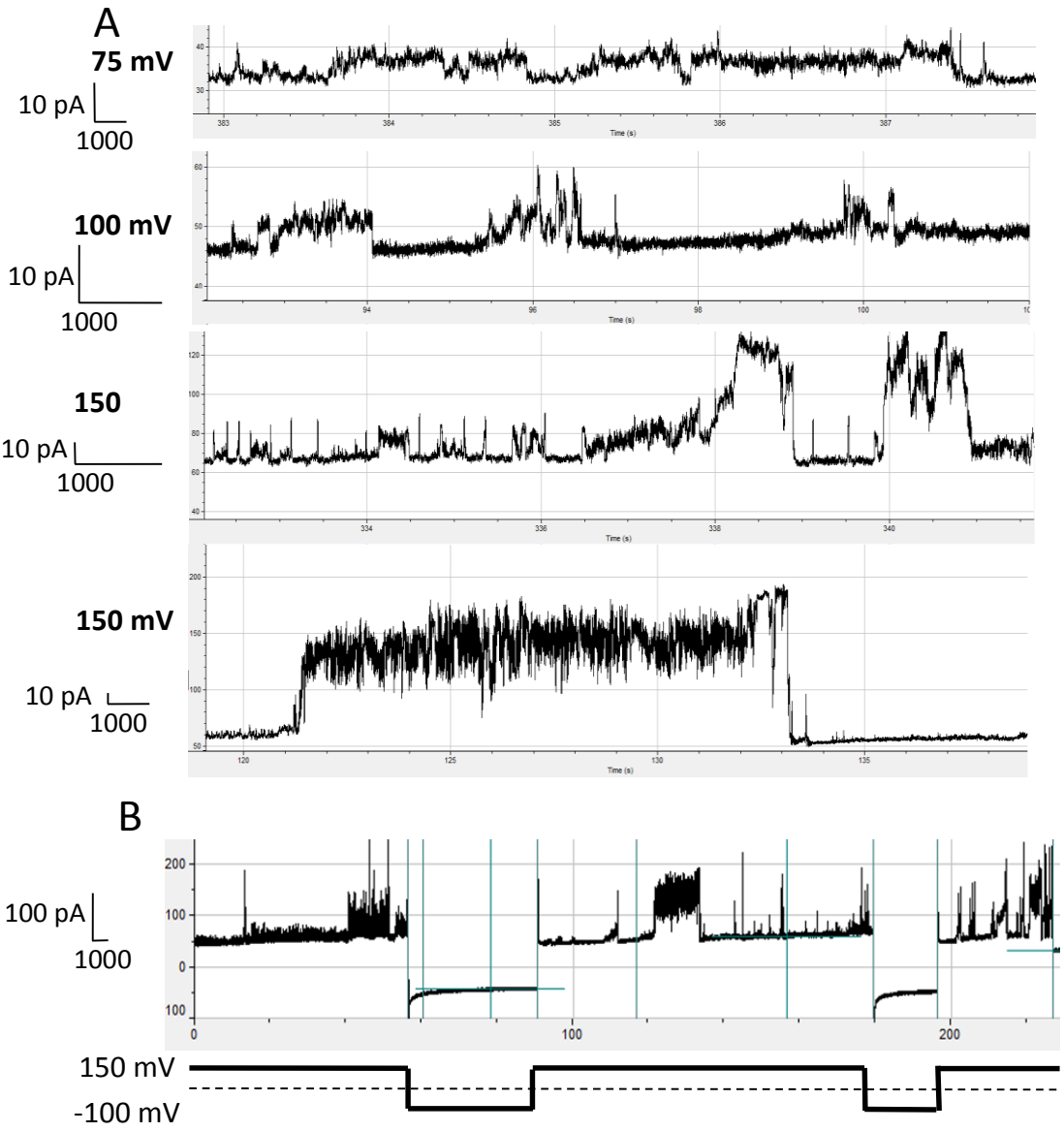

Figure 31: Electrophysiology of NavBh128-RCK M107I Co-Expressed With Soluble RCK.
A) Recordings of proteoliposome reconstituted, IMAC purified NavBh128-RCK M107I plus RCK in PE:PG bilayers suspended in a microaperture, at the indicated voltages. Measurements made at pH 8, 10 mM $CaCl_2$ B) Measurements made over 250 seconds, during which the holding potential was switched back and forth between +150mv, and -100mv. Note that due to the instability of conductance, scales vary greatly depending on the recording. Recordings performed in 20 mM Tris, 0.5 M NaCl, pH 8.0, with 10 mM $CaCl_2$.

`

4.9 Electrophysiology of NavBh128-RCK M107I Co-expressed With the Soluble RCK Domain

Co-purified NavBh128-RCK M107I and soluble RCK domain was characterised as previously described for NavBh-RCK and NavBh128-RCK. The NavBh128-RCK M107I plus RCK was more active than either of the previously investigated constructs. In the absence of calcium at pH 8, the channel displayed no conductance. Upon the addition of calcium NavBh128-RCK M017I+RCK was found to have extremely unstable conductance (Figure 31). Reducing the amount of proteoliposome added reduced the reliability and frequency of activity, however it had no effect on the stability of conductance (data not shown). Switching the voltage holding potential from positive to negative during channel activity stopped all activity until the holding potential was switched back (Figure 31b). This is contrary to what was observed for the constructs previously tested, which displayed continued activity when the holding potential was switched from positive to negative, or vice versa. This suggested a different mechanism of channel gating than previously observed in the absence of the co-expressed soluble RCK domain.

4.10 NsvBa-RCK and NavMs-RCK

Four additional Nav-RCK constructs were generated, from the previously discussed sodium channel homologues NavMs and NsvBa, and their respective pore-

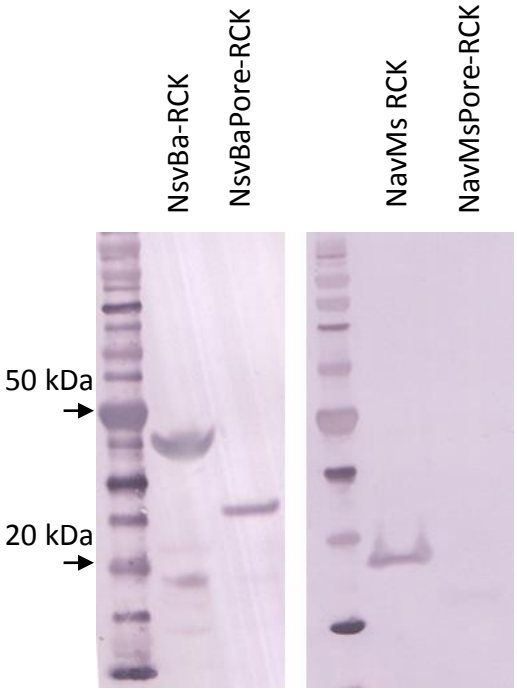

Figure 32: Expression Trials of NsvBa-RCK and NavMs-RCK.
Western blots of expression trials of NsvBa-RCK NsvBaPore-RCK, NavMs-RCK, and NavMsPore-RCK. Expression for three hours at 37°C.

`

only constructs, homologous to NavBh128 (Figure 33), in order to test whether a different prokaryotic Nav homologue would display higher solubility. NsvBa-RCK and NsvbaPore-RCK did express, however after membrane solubilisation both were found to have precipitated out of solution completely. NavMs-RCK was found to not express at all. These constructs were not pursued further.

4.11 Modelling of the Nav-RCK Linker Region

In the MthK crystal structure the lack of a resolved linker region between the pore and the RCK domain lead to the assumption that this region was disordered. A total of 19 residues were unresolved between the end of the pore and the first resolved residue of the RCK domain. The NavBh-RCK chimera was designed such that the linker region would be approximately the same length. Superposition of the NavMs and MthK pores, both of which are in an open conformation, demonstrated that the end of the last transmembrane helix is in a different position in open conformation of the channels (Figure 27). In order to better understand how this difference between prokaryotic sodium and potassium channels in the open conformation may have affected the NavBh-RCK chimera, homology modelling of these missing MthK linker region residues into the NavAb-RCK and NavMs-RCK alignment models was performed.

PsiPred structural prediction of the wild type MthK sequence predicted that the second pore helix would continue through almost the entire missing region, however there was a drop in the confidence of this prediction in the unresolved linker region (Figure 34a). Such an ordered helix would likely have been resolved in the crystal structure, and given the low confidence it seems unlikely that this prediction is correct. Thus, an ab initio loop modelling approach was employed to determine what a completely disordered linker region would look like. Ab initio modelling of the unresolved 19 amino acids resulted in a large, flexible loop (Figure 34B). If these residues were disordered, the difference between the closed and open RCK structures would not have been enough to pull this region taut and affect gating of the channel. This modelling demonstrated the necessity of some structure within this region. Furthermore, experiments in which the linker region of the BK channel was modified demonstrated that the linker was relatively taut (Niu et al. 2004). Such a large, flexible

`

connecting region would also likely have interfered with the formation of crystals by MthK.

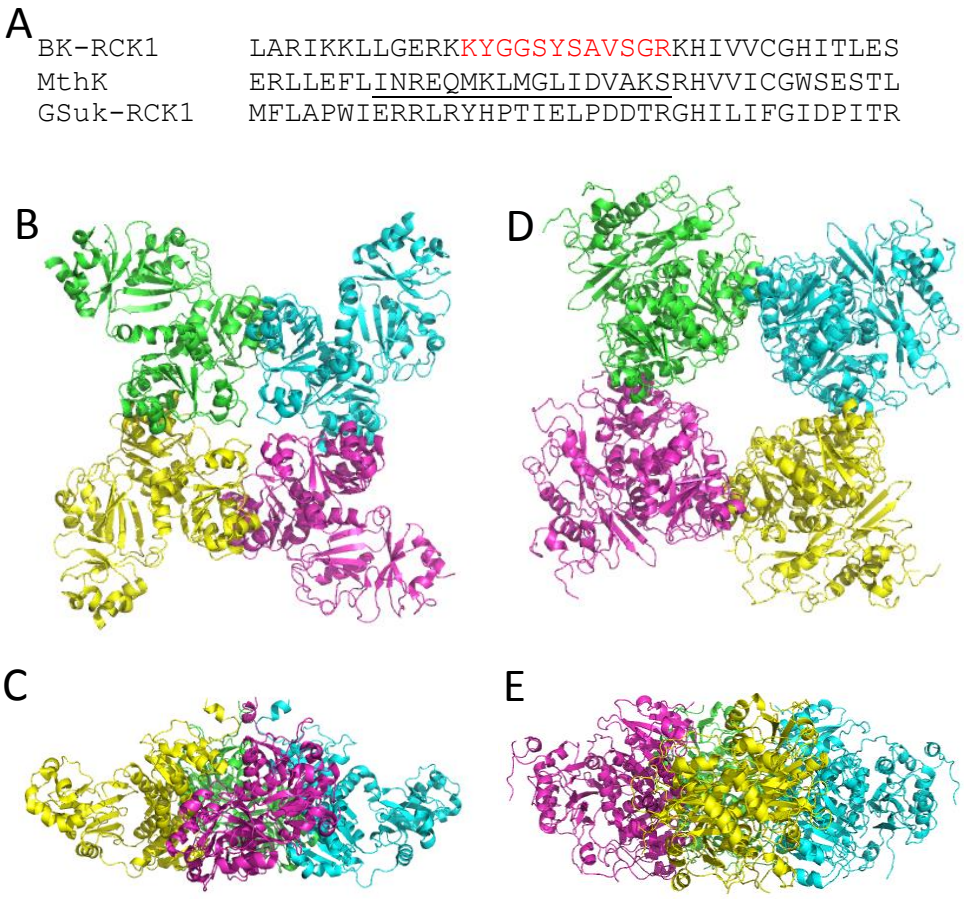

Figure 33: RCK Gating Ring Structures With the Pore-RCK Linker Resolved.
A) Clustal Omega alignment of the MthK linker region (un-resolved residues in red), with homologous linker region from the eukaryotic BK channel, and the prokaryotic GSuK channel. B, C) Structure of the BK gating ring (PDB ID 3NAF). D,E) Structure of the GSuK gating ring (PDB ID 3GVL). Images generated in Pymol.

The recent publication of a crystal structure of GSuK, a full length prokaryotic RCK gated potassium channel in a closed position with a resolved linker region (Kong et al. 2012) allowed for a homology based modelling approach. In combination with the structure of the octomeric gating ring from the BK channel (Wu et al. 2010), this allowed for modelling of the linker region in both the open NavMs-RCK model and the closed NavAb-RCK model. In these structures the linker region was found associated with several clefts along the top of the RCK domain (Figure 33), rather than existing as an unstructured free floating loop. While the sequence homology between BK/GSuK and MthK in this region is low (Figure 33A), modelling of BK/GSuK linkers onto the open and closed MthK-RCK domains resulted in the linker occupying homologous clefts

`

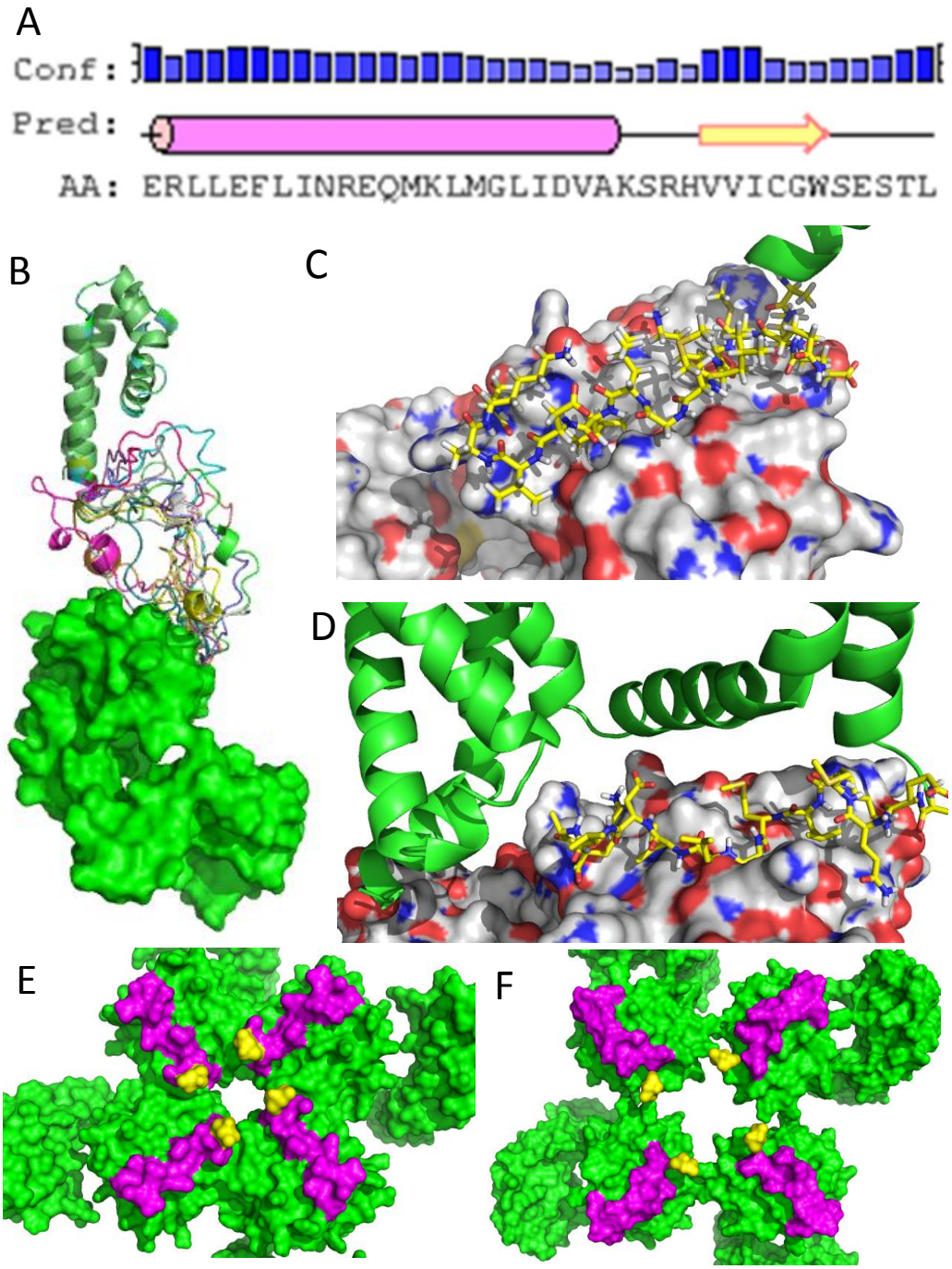

Figure 34: Homology Modelling of the Pore-RCK Linker Region in Nav-RCK Models. A) PsiPred analysis of the MthK unresolved linker region. Confidence levels are shown as blue bars, pink cylinders indicate helical prediction, yellow arrows indicate sheet prediction, black line indicates coil or disorder prediction. B) Whole loop modelling of the unresolved linker region of MthK. C, D) Homology modelling of the linker region of MthK, in NavMs-RCK (C), and NavAb (D) based upon the BK and GSuK linker regions, respectively. E, F) Surface rendering of the modelled S6-RCK linker region in NavMs-RCK (E) and NavAb-RCK (F). The RCK domain is in green, the modelled linker region is in purple, and the last residue of the S6 helix is shown in yellow. Images generated in Pymol.

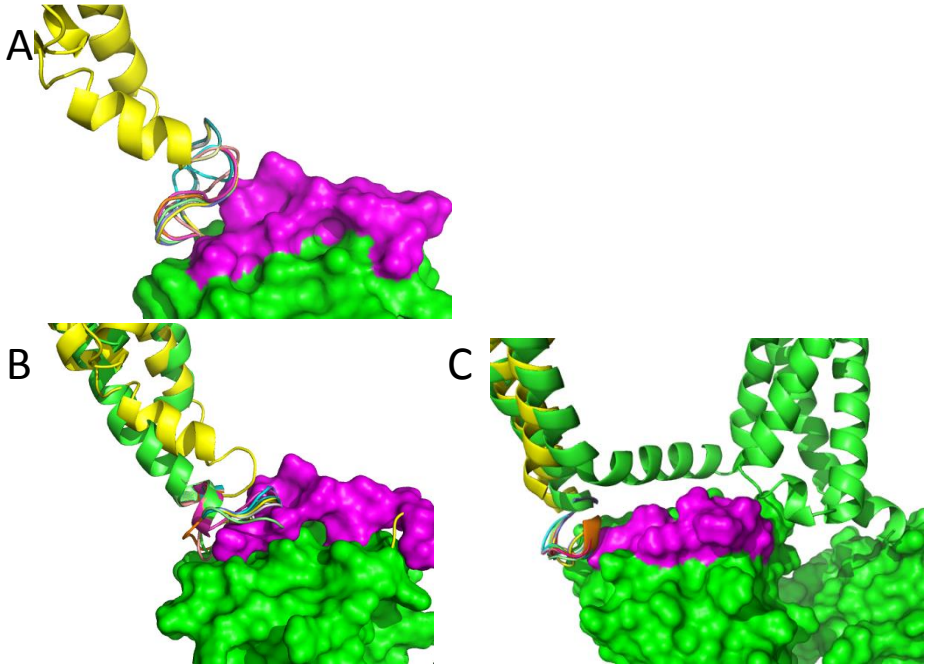

Figure 35: *Ab Initio* Modelling of Residues Not Resolved By Homology Modelling of the Pore-RCK Linker Region in Nav-RCK Models.
A) MthK, B) NavMs-RCK (green), with the MthK pore (PDB ID 3RBZ) superposed in yellow, C) NavAb in green, with KcsA (PDB ID 2DWD) superposed in yellow. 10 iterations of loop modelling are shown, the RCK is shown as a surface representation in green, with the homology modelled linker region in purple. Images generated in Pymol.

on the top of the RCK domain (Figure 34C,D). A view of the gating ring with this linker from the extracellular side and the end of the S6 helices demonstrated that with the pore closed the end of the S6 helix (in yellow) sits directly above the end of the linker, whereas the end of the open NavMs pore does not (Figure 34E, F). Ab-initio modelling of the remaining missing residues demonstrated few possible conformations, which suggested that there is less flexibility in this region in both the Nav-RCK models, as compared to MthK (Figure 35).

4.12 Conclusions

Taken in the context of the concentration dependent precipitation of the NavBh-RCK fusion chimera, this difference in position of the S6 suggested a potential mechanism by which the protein could be destabilised. It is possible the the change in conformation of the RCK domain upon formation of the octomeric gating ring disrupted the NavBh pore enough to destabilise the protein, resulting in its precipitation. At low concentrations, the formation of the full octomer would have been an unlikely event, and thus the protein would remain stable. At higher

`

concentrations, the octomeric gating ring would have been more likely to form even in the absence of calcium, resulting in destabilisation and precipitation.

While the electrophysiological analysis demonstrated that NavBh-RCK was a functional ligand gated sodium channel, the poor reliability of activity and the instability of conductance combined with the requirements of maintaining the protein at low concentrations demonstrated that the fusion chimera was not an ideal strategy. Subsequent publication of multiple prokaryotic Nav crystal structures and of the GSuk crystal structure allowed for retrospective improvement to the Nav-RCK models. Analysis of these models suggested a cause for the precipitation of the NavBh-RCK constructs.

`

Chapter 5: Structural Investigation of NsvBa

5.1 Overview

As previously discussed (Chapter 1.9), functional characterisation of a close homologue of NavBh has recently been published (DeCaen et al. 2014). Despite being a member of the Nav family (Figure 2), it was shown to be a non-selective voltage gated ion channel (NsvBa). However, many residues characterised in NavBh were conserved in NsvBa. This made it an interesting target for structural study, given the lack of a crystal structure of NavBh. Furthermore, initial structural predictions for the neck region of the C-terminus found significant probabilities for both helical and disordered secondary structure. In light of the recent studies which suggested the possibility of a structural transition within this region during channel gating, SRCD spectroscopy and EPR spectroscopy was utilised to characterise the structure of the NsvBa C-terminus.

```
NavBh      ---------MKMEARQKQNSFTSKMQKIVNHRAFTFTVIALILFNALIVGIETYPRIYAD
NsvBa      --------------MQKQSLLIHFSKKIVSHRYFTRIIITLILFNALLVGLETYPALRHE
NavAe      MSERQPDLVGHKVQHPEDETLRGRLAWFIDRPGTQYFIVGLILVNAITLGLMTSPEVTAY
NavMs      --------------------MSRKIRDLIESKRFQNVITAIIVLNGAVLGLLTDTTLSAS
                                :      ::.       :  :*:.*.  :*: *   :
NavBh      HKWLFYRIDLVLLWIFTIEIAMRFLASNPKSAFFRSSWNWFDFLIVAAGHIFAGAQFVTV
NsvBa      YGSLFHVLDVILLWIFTLEILTRFLATTPKKDFFKGGWNWFDTIIVLSSHIFVGGHFITV
NavAe      LQPWLGWVNTFIIAAFVVEISLRIIADGP--RFVRSGWNLFDFSVVAISLVPDSGA-FSV
NavMs      SQNLLERVDQLCLTIFIVEISLKIYAYGVR-GFFRSGWNLFDFVIVAIALMPAQGS-LSV
               :  :: . :  * :**  :: *      *.:..** **  :*  . :   .  .:*
NavBh      LRILRVLRVLRAISVVPSLRRLVDALVMTIPALGNILILMSIFFYIFAVIGTMLFQHVSP
NsvBa      LRILRVLRVLRAISVIPSLRRLVDALMLTIPALGNILILMSIIFYIFAVLGTMLFANVAP
NavAe      LRALRILKVLRLFSMVPRLRRIVEALLRAIPGIAWIALLLLVIFYVFAVMGTKLFAQSFP
NavMs      LRTFRIFRVMRLVSVIPTMRRVVQGMLLALPGVGSVAALLTVVFYIAAVMATNLYGATFP
           ** :*:::*:* .*::* :**:*:.:: ::*.:. :  *: :.**: **:.* *:    *
NavBh      EYFGNLQLSLLTLFQVVTLESWASGVMRPIFAEVPWSWLYFVSFVLIGTFIIFNLFIGVI
NsvBa      EYFANLQLSMLTLFQIVTLDSWGSGVMRPILVDIPWAWTYFIAFVLVGTFIIFNLFIGVI
NavAe      EWFGTLGASMYTLFQVMTLESWSMGIARPVIEAYPWAWIYFVSFILVSSFTVLNLFIGII
NavMs      EWFGDLSKSLYTLFQVMTLESWSMGIVRPVMNVHPNAWVFFIPFIMLTTFTVLNLFIGII
           *:*. *  *: ****::**:**. *: **::   * :* :*: *::: :* ::******:*
NavBh      VNNVEKAELTDNEEDG--EADGLKQEISALRKDVAELKSLLKQSK---------------
NsvBa      VNNVEKANEDEVKDKVKEKEEAAQKQMDSLHEELKEIKQYLKSIEKQNRSS---------
NavAe      IESMQSAHWEAEDAKRIEQEQRAHDERLEMLQLIRDLSSKVDRLERRSGKR---------
NavMs      VDAMAITKEQEEEAKTGHHQE-------PISQTLLHLGDRLDRIEKQLAQNNELLQRQQP
           :: :  :.    . .   . :        : : : .: . :.  :
NavBh      ---
NsvBa      ---
NavAe      ---
NavMs      QKK
```

Figure 36: Alignment NsvBa with structurally characterised C-termini.
Clustal Omega sequence alignment of NavBh, NsvBa, NavAe, and NavMs amino acid sequences.

`

5.2 Expression and Purification of NsvBa

Expression trials of WT NsvBa demonstrated a level of expression comparable to WT NavBh (data not shown). Initial purification attempts yielded quantities of pure protein sufficient for crystallisation trials (Figure 37). Purified WT NsvBa migrated primarily as a single peak at the expected size with a long shoulder. This shoulder may have indicated a tendency for aggregation, however no precipitate was observed, and no peak was present in the void volume. Crystallisation trials of WT NsvBa yielded no crystals (Table 1).

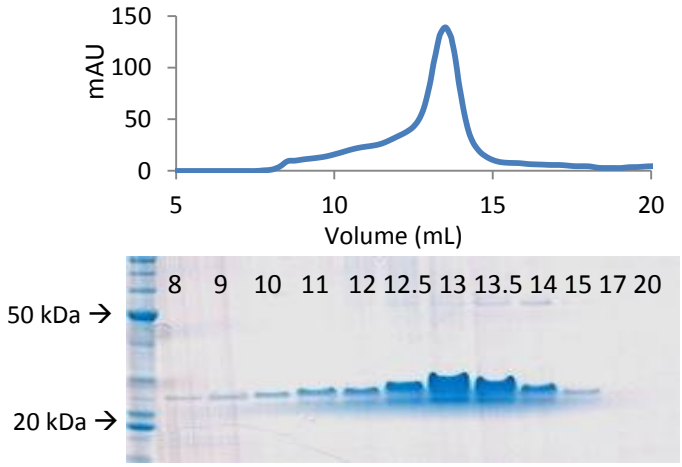

Figure 37: Gel Filtration of IMAC purified NsvBa. Gel filtration plot and coomassie stained SDS-PAGE, corresponding to the labelled fractions.

5.3 *In Silico* Investigations of NsvBa C-Terminal Structure

Recent publications have investigated the structure and function of the Nav C-terminus. A previous SRCD spectroscopy study demonstrated in NavBh that the C-terminus consisted of a disordered neck region followed by a helical region which was predicted to be a coiled-coil (Powl et al. 2010). Site directed spin labelling and DEER-EPR spectroscopy experiments confirmed those results in NavMs, and suggested that this region may also take on a more restrained conformation (Bagnéris et al. 2013). In the crystal structure of the NavAe pore, the NavAe C-terminal neck region was observed to be almost entirely helical (Shaya et al. 2014). Functional characterisation of NavAe required disruption of the structure within this region. This offered further support for the hypothesis that the disordered neck region had a functional role in channel gating, and that a more structured C-terminus stabilised the pore in the closed conformation. While NsvBa had approximately 66% identity with NavBh, the C-terminus was the least conserved region (Figure 36). PsiPred structural analysis

`

predicted a significant probability that this region was helical, similar to NavAe (Figure 38A). However DisoPred protein disorder prediction significantly predicted that this region was disordered, similar to NavBh and NavMs (Figure 38B). Given the hypothesis that channel gating may involve a helix to disorder transition within the neck region, the predictions for both a helical and disordered neck region made NsvBa an interesting target for structural investigations of the C-terminus.

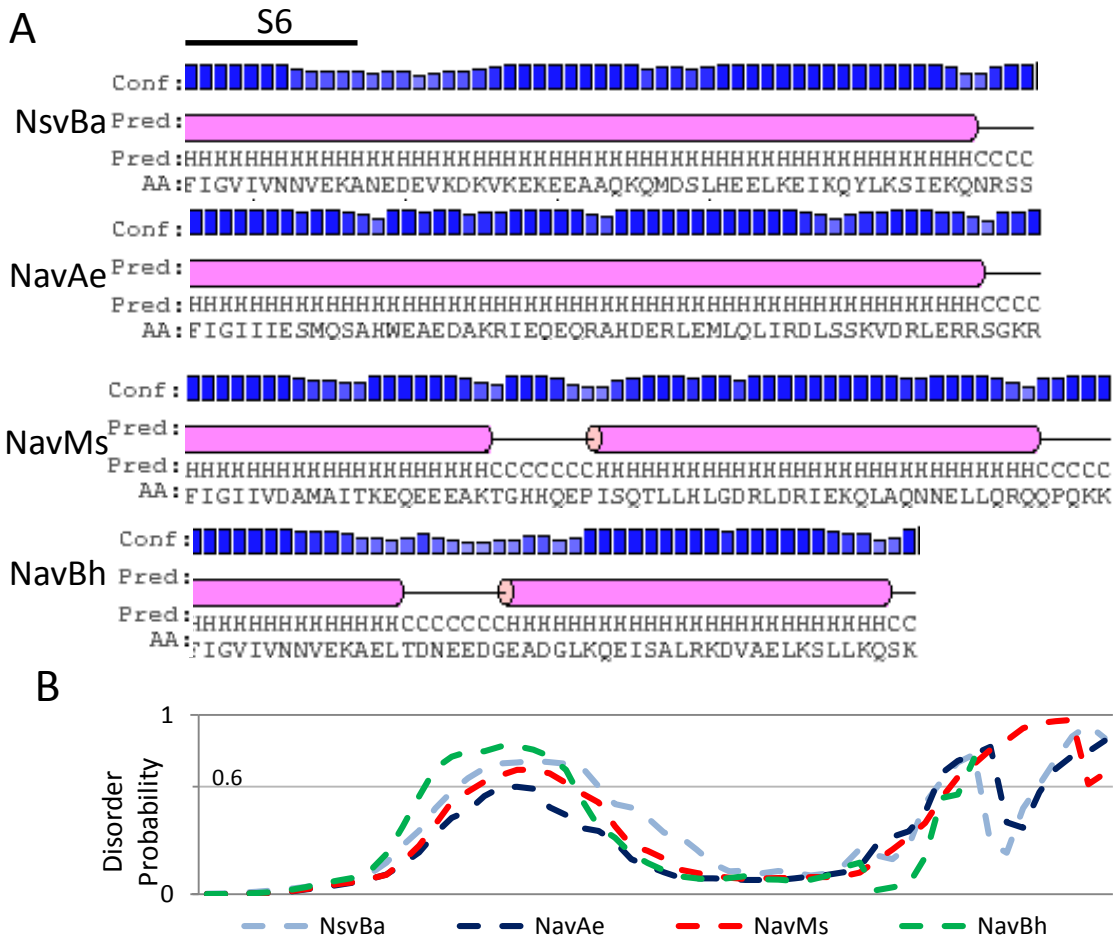

Figure 38: Predictions for Secondary Structure of the NsvBa C-Terminus.
A) PsiPred structural predictions for NsvBa, NavAe, NavMs, and NavBh. Predictions were performed on the full length amino acid sequences, however only the end of the S6 helix and C-terminus are shown. Residues marked H denote helical predictions, residues marked C denote disordered predictions B) DisoPred disorder predictions for the matching regions of the Nav C-terminus, X axis corresponds to the sequences displayed in A. The standard cut-off value for disorder prediction of 0.6, above which a sequence is predicted to be disordered, is shown.

5.4 Homology Modelling of the NsvBa C-Terminus

In order to gain a better understanding of the secondary structure predictions for the NsvBa C-terminus, Phyre2 automated homology modelling was performed

`

using the NavMs pore molecular dynamics model (Bagnéris et al. 2013) to generate a disordered neck model, and the NavAe pore crystal structure (Shaya et al. 2014) to generate a helical neck model (Figure 39). The C-termini of the models corresponded to the *in silico* structure predictions for the neck region of the NsvBa C-terminus. It should be noted that the NavMs crystal structure had an open pore, whereas the NavAe crystal structure had a closed pore. These pore states are retained in the corresponding NsvBa models.

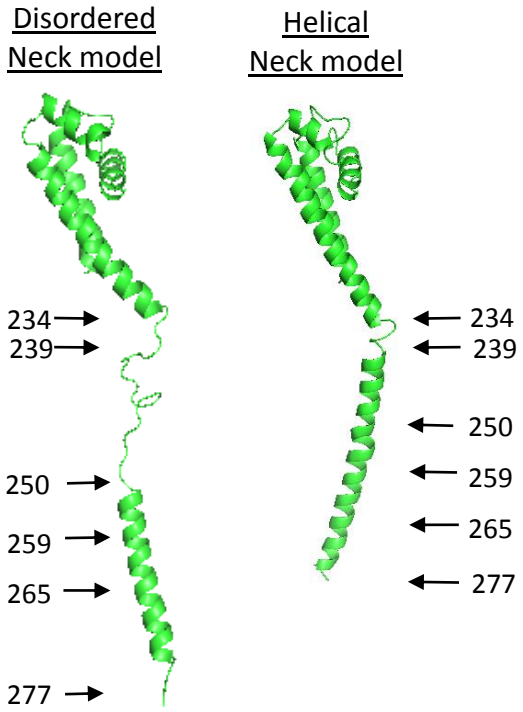

Figure 39: Homology Models of the NsvBa C-Terminus.
Disordered neck model based on NavMs (left), and the helical neck model based on NavAe (right). Monomers of each are shown. Approximate length of truncation constructs displayed with labelled arrows. 227 denotes the full length protein. Images generated in Pymol.

5.5 Expression and Purification of NsvBa C-Terminal Truncations

In order to facilitate structural investigation of the NsvBa C-terminus, a series of C-terminal truncation mutants were generated (Figure 40). In expression trials the removal of seven residues from the end of NsvBa (construct NsvBa 265) resulted in an increase in size of the anti-hexahistidine stained band in western blotting of crude extract (Figure 40B). This increased size can also be observed for truncations 259 and 250, and in the same truncations of the pore-only construct NsvBa138. A similar effect was not reported in the homologous NavBh truncations (Powl et al. 2010), nor in non-

`

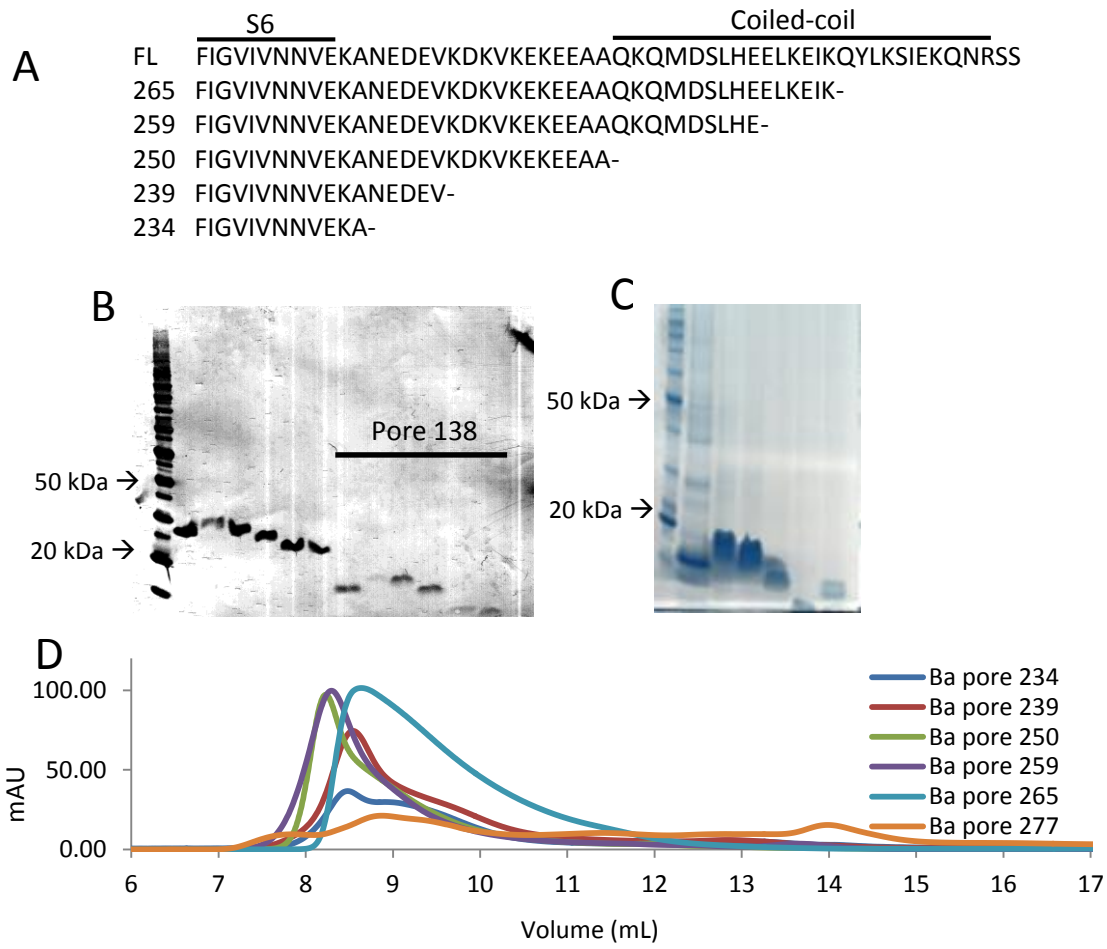

Figure 40: Diagram, Expression and Gel Filtration of NsvBa C-Terminal Truncations. A) Sequences of NsvBa C-terminal truncations, showing the location of the inserted stop codon. B) Western blot analysis of 3 hour 37° expression trials, whole cell lysate. Full length NsvBa on the left, and pore-only constructs, which start at residue 138, on the right. C) SDS-Page of gel filtration purified pore constructs. D) Gel filtration profiles of NsvBa Pore truncations.

homologous C-terminal truncations of NavMs (C. Bagnéris, personal communication). It should be noted that unusual behaviour during SDS-PAGE and gel filtration has not been uncommon for prokaryotic Navs. However, no examples of an increase in band size during SDS-PAGE due to truncation of the C-terminus could be found in the literature, nor has it been previously observed within the Wallace lab. Variation in boiling times of the samples, and addition of 1M urea had no effect (data not shown). During purification trials all truncation constructs of the full length channel were found either in inclusion bodies, or to have precipitated during membrane solubilisation (data not shown). Truncations of the pore-only construct NsvBa138, in which the voltage sensor has been removed and expression starts from the 138th residue, were found in the membrane fraction and were successfully purified. NsvBa 138-277 (pore-

`

only, with the full length C-terminus) was found to have the lowest expression of any of the constructs tested. Truncations in the coiled-coil domain (NsvBa138-265, NsvBa138-259, and NsvBa 138-250) all had high expression, while truncations in the neck region had comparatively less expression (Figure 40b).

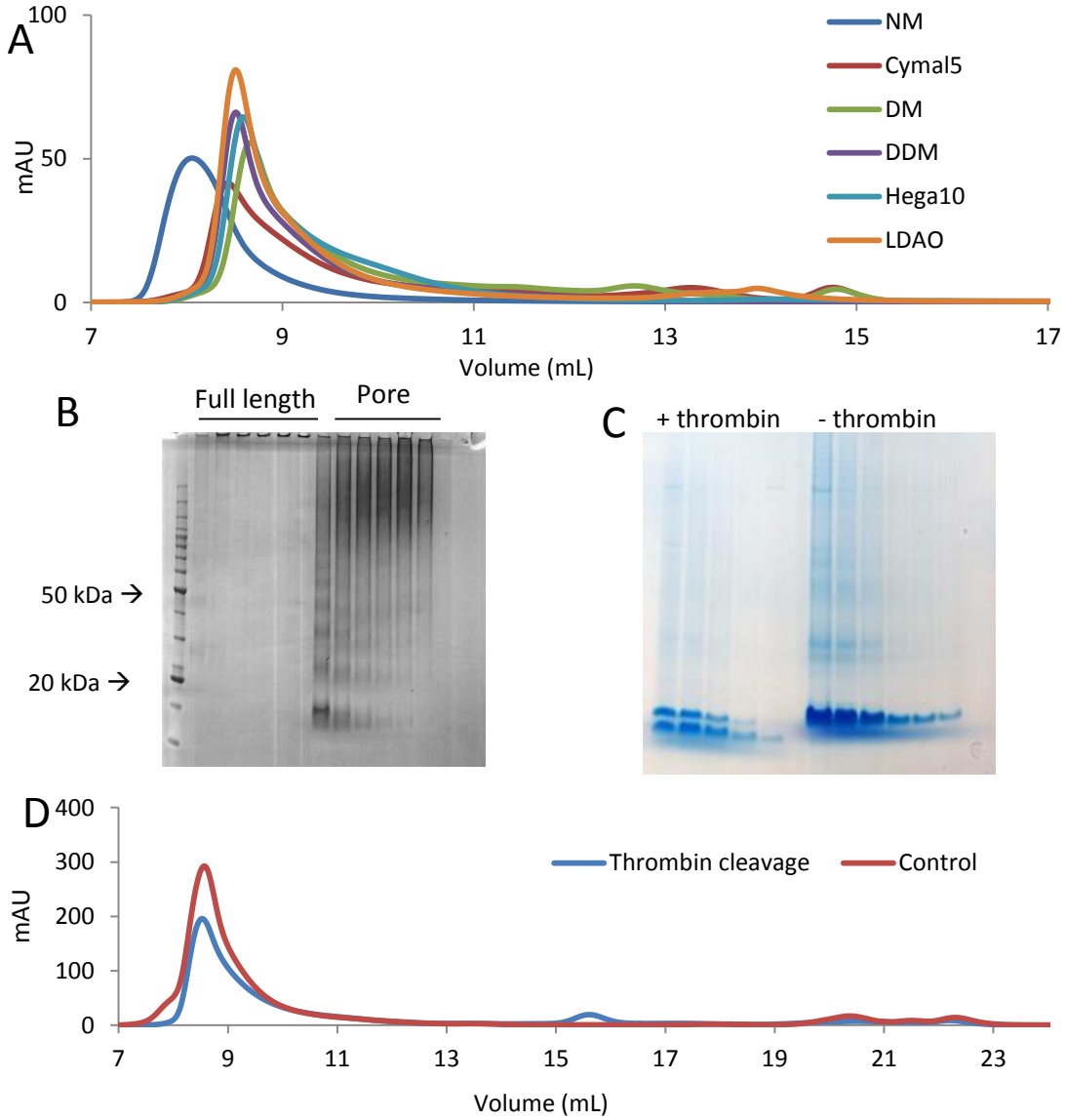

Figure 41: Investigation of NsvBa Aggregation.
A) Gel filtration detergent screening of NsvBa pore 138-265. B) SDS-PAGE of gluteraldehyde crosslinking of NsvBa 265 and NsvBa Pore 138-265, samples taken at 0.5, 1, 2, 5, 25, and 60 minutes. C) Coomassie stained SDS-PAGE corresponding to gel filtration from D. D) Thrombin cleavage of NsvBa138-265 and no-thrombin control.

While IMAC of NsvBa pore constructs was without complication, in gel filtration NavBa138 truncation constructs did not elute at the expected size of 60-90 kDa, but instead as a peak near but not in the void volume, corresponding to > 600kDa (Figure 40D). Gluteraldehyde crosslinking of NsvBa265 and NsvBa138-265 further

`

demonstrated that NsvBa associated in higher order oligomers (Figure 41b). This was not accompanied by any precipitation of the protein. Samples exhibited no loss of protein concentration after 48 hours storage at 4°C, during transportation for SRCD spectroscopy experiments, or during freeze-thawing (data not shown). Detergent screening of NsvBa138-265 demonstrated that this effect was independent of detergent, except in the case of NM, in which NsvBa precipitated and can be seen to

A

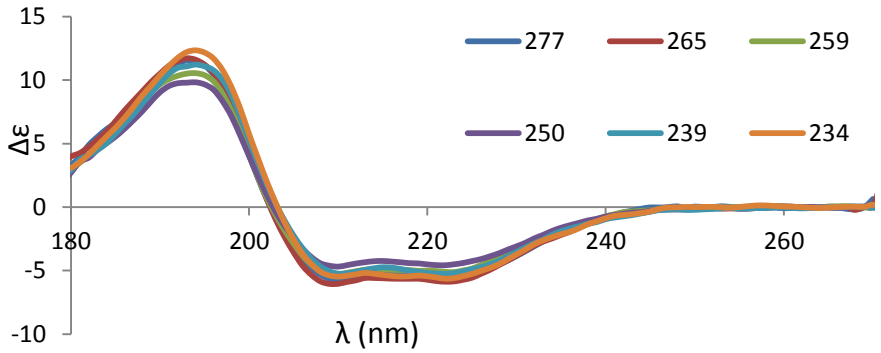

B

Δ	Calculated Helical Residues Removed: Experimental Data	Predicted Helical Residues Removed: Disordered Neck Model	Predicted Helical Residues Removed: Helical Neck Model	Predicted Helical Residues Removed: Transition Model
277	0	0	0	0
265	13.49 +/- 0.03	13	13	13
259	17.41 +/- 1.37	19	19	19
250	27.49 +/- 1.99	28	28	40
239	26.03 +/- 1.62	27	39	40
234	22.32 +/- 7.04	28	40	40

C

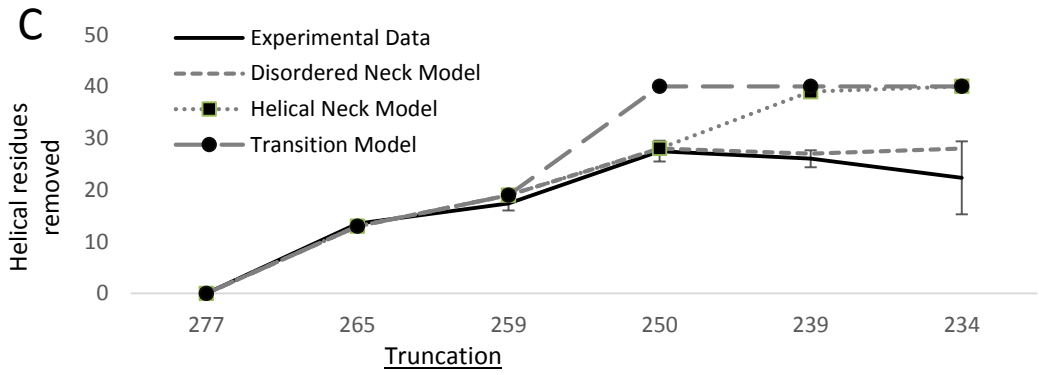

Figure 42: SRCD Analysis of NsvBa Truncations.
A) Representative SRCD spectra of NsvBa truncations. B) Calculated helical residues removed, and predicted helical residues removed for Disordered Neck, Helical Neck, and Transition models. Predictions were obtained by determining secondary structure of each removed section of the corresponding model. C) Graph of B

`

elute in the void volume (Figure 41A). No indications of precipitation were observed in any other conditions. Thrombin cleavage of the hexahistidine tag was also tested, however it had no effect on the unusual behaviour (Figure 41Figure 41C, D).

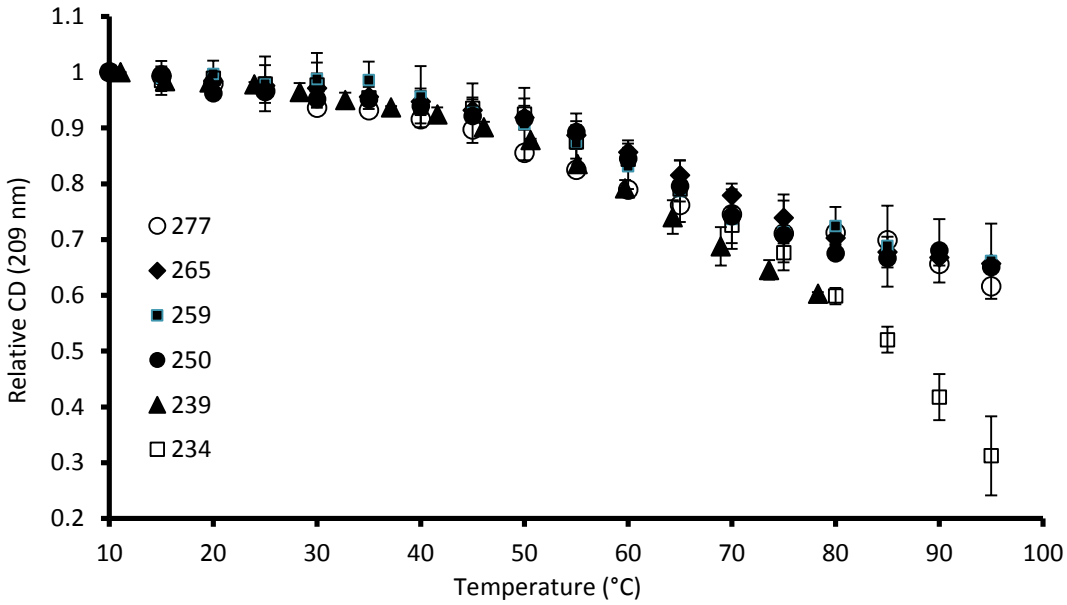

Figure 43: Thermal Unfolding SRCD Spectroscopic Analyses of NsvBa 138 C-Terminal Truncations.
Relative CD signal at 209 nm of listed C-terminal truncations of NsvBa 138 during SRCD thermal unfolding. Error bars denote standard deviation between replicate experiments. 277 denotes the full length protein.

5.6 SRCD Spectroscopy of NsvBa C-Terminal Truncations

Previous work with NavBh demonstrated that SRCD spectroscopic analyses of a series of truncation constructs could be used to investigate the local secondary structure of a protein (Powl et al. 2010). Determination the secondary structural percentages of each truncation construct enabled calculation of the structure of the truncated residues. Comparison of the NsvBa helical neck and disordered neck models predicted that the primary difference between the two models would be observed in the truncations at 234, and 239. In the helical neck model 40 helical residues were predicted to be removed by the 239 truncation. The same truncation would remove only 28 helical residues in the disordered neck model. (Figure 42B). The possibility of a transition between the two models was also considered. If the presence of the coiled-coil stabilised the neck region in a helical conformation, then complete removal of the coiled-coil by truncation at 250 would have resulted in the neck region adopting a disordered conformation. This would have been observed as the loss of 40 helical

`

residues in the truncation at 250. Calculation of the number of helical residues removed, based on the averaged spectra from three replicates correlated significantly with the disordered neck model of the NsvBa C-terminus (Figure 42B).

Thermal unfolding analysis of the pore at 209 nm demonstrated that the full length 277, and the 265, 259 and 250 C-terminal truncations maintained a high degree of helicity even above 50°C, as is common for Navs (Figure 43). However both the 239 and the 234 truncations displayed lower thermal stability than the longer truncations.

5.7 EPR Spectroscopy of the NsvBa C-Terminus

As discussed in Chapter 3.11, a previous study by the Wallace lab in collaboration with the Kay Lab of University College London utilised site directed spin labelling in combination with continuous wave electron paramagnetic resonance (CW-EPR) spectroscopy and pulsed double electron-electron resonance electron

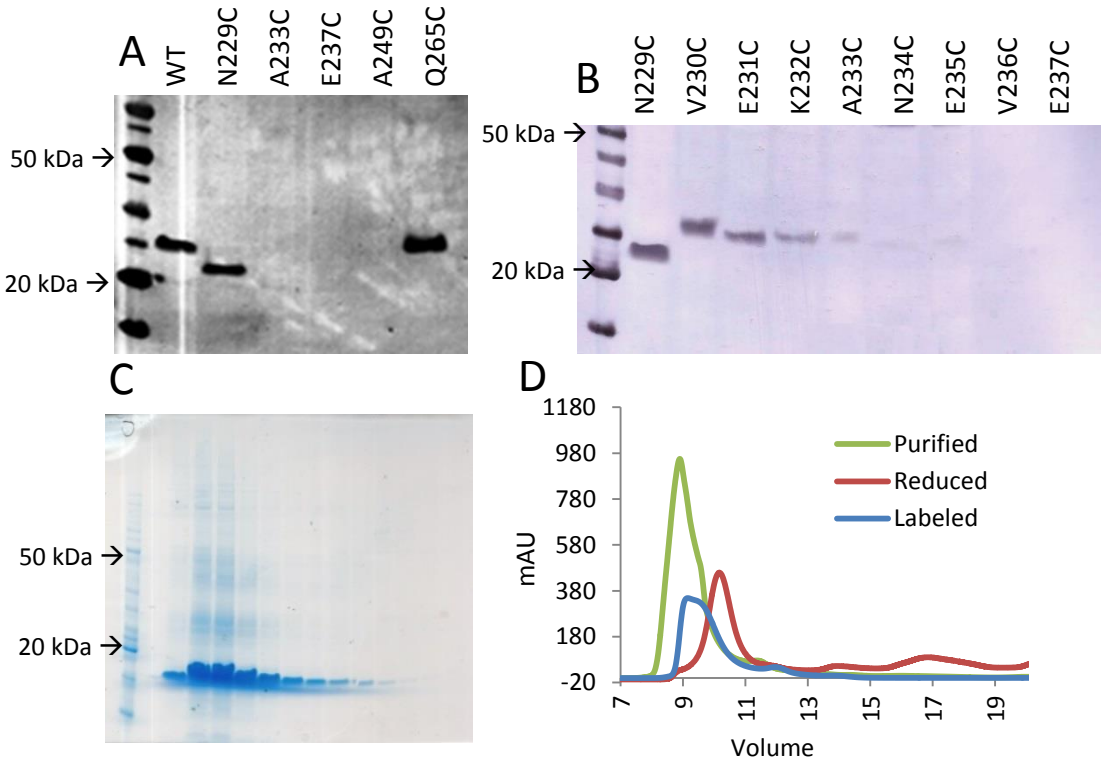

Figure 44: Expression and Purification of NsvBa Cysteine Mutants for DEER-EPR. A) Expression trials of cysteine mutants homologous to those made in NavMs, expression for three hours, 37°C. Western blot of whole cell lysate. B) Scanning cysteine mutagenesis of the NsvBa C-terminal neck region. Expression for three hours at 37°C, western blot of whole cell lysate. C) SDS-PAGE of gel filtration of NsvBa pore 138-265 N229C, corresponding to the purified sample in D. D) Gel filtration of purified, reduced, and labelled NsvBa pore 138-265 N229C. Note that the purified sample was not yet reduced.

`

paramagnetic resonance (DEER-EPR) spectroscopy to investigate the structure of the NavMs C-terminus (Bagnéris et al. 2013). The nitroxide spin labelling of a cysteine residue enabled the use of CW-EPR spectroscopy to examine the mobility of the spin label, which in turn provided information about the conformation of the labelled residue. A label with limited mobility indicated that the residue it was bound to was conformationally restrained (Steinhoff et al. 1994). Navs are homo-tetrameric and thus labelling resulted in four spin labels in close proximity. This enabled the use of DEER-EPR spectroscopy, a technique which measured the distance distributions of the spin labels, based upon their dipole-dipole interactions (Schiemann & Prisner 2007).

In order to further investigate the structure of the NsvBa C-terminus, a series of cysteine mutations was made in the C-terminus of the NsvBa pore to facilitate nitroxide spin labelling. Early expression tests demonstrated cysteine mutations homologous to those made in NavMs had a strong negative effect on expression. Only N229C and the Q265C demonstrated sufficient expression for purification trials (Figure 44A). This was unexpected, as cysteine mutagenesis at the homologous positions in NavMs did not affect expression (C. Bagnéris, personal communication). Scanning cysteine mutagenesis of the neck region demonstrated that this sensitivity is true for all residues within the region of interest (Figure 44B), and large scale purification attempts of NsvBa N229C, NsvBa A233C and NsvBa Q265C did not yield sufficient protein for EPR spectroscopic studies. The NsvBa pore construct 138-277 (full length C-terminus) had expression and purification yields too low to be a viable target for EPR spectroscopic studies.

The NsvBa pore 138-265 construct had the highest expression of any construct tested. While this construct did truncate the last 12 residues of the C-terminus, SRCD spectroscopic analysis demonstrated that this truncation did not affect the secondary structure of the remainder of the protein (Figure 42). Large scale expression and purification of NsvBa138-265 N229C yielded sufficient protein for DEER-EPR spectroscopic studies (Figure 44C). Large scale purifications of NsvBa138-265 A233C, E237C, and A249C did not yield sufficient protein for EPR spectroscopy (data not shown).

Reduction and nitroxide spin labelling of NsvBa138 N229C further demonstrated the tendency of NsvBa138-265 to form higher order oligomers during

`

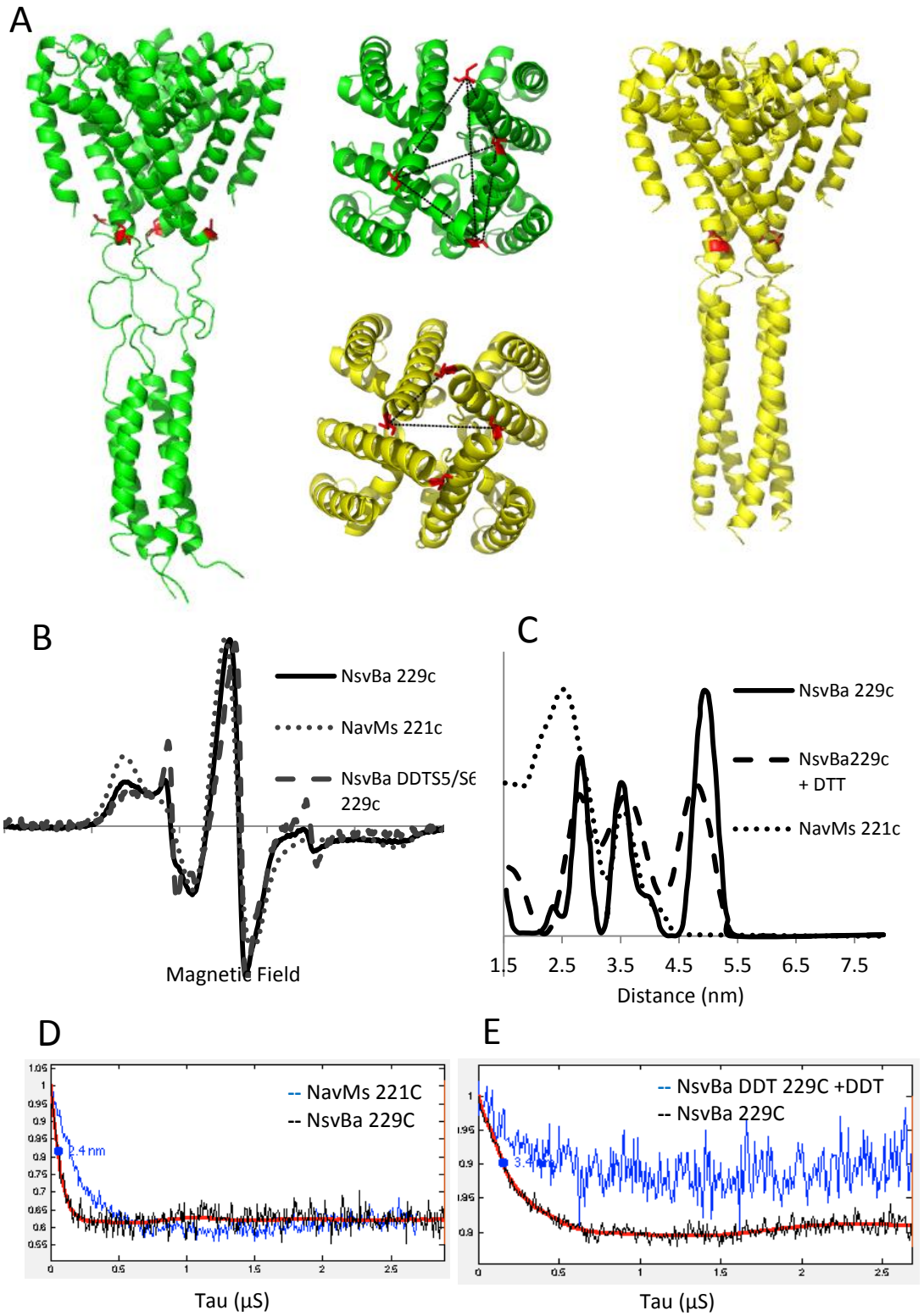

Figure 45: EPR Spectroscopy of NsvBa265 229C.
A) Disordered neck (green) and helical neck (yellow) NsvBa models, with residue 229 mutated to a cysteine, and shown in red. Cutaway view of both models at residue 229, with measurements shown. B) CW-EPR of NsvBa295 N229C (solid) and the homologous NavMs A221C (dotted), NavMs data provided by Dr Chris Kay. C) DEER-EPR measurements of NsvBa N229C, NsvBa N229C with mutations to introduce the DDT binding sites, +DDT. D) Raw DEER data for NavMs A221C, and NsvBa N229C. E) Raw DEER data for NsvBa N229C, and NsvBa N229C with mutations for the introduction of DDT binding sites, +DDT.

gel filtration (Figure 44A). Unreduced protein migrated primarily as a large peak eluting around 9 mL, with a smaller shoulder at 9.5 mL. Reduction of the protein by one hour incubation with 5 mM DTT shifted the peak towards 10 mL, and introduced two small, broader peaks at the expected size of the tetramer and monomer. 48 hour incubation with a 20 fold molar excess of the nitroxide spin label shifted the primary peak back to 9 mL, and re-introduced the shoulder at 9.5 mL.

CW-EPR spectroscopy demonstrated that the label at N229C had mobility similar to that of the label in the homologous NavMs A221C (Figure 45B). This was expected as 229 was predicted to be the last residue of the transmembrane helix in both NsvBa models. DEER-EPR spectroscopy measurements of nitroxide spin labelled NsvBa 138-265 N229C were remarkably different from measurements of labelled NavMs A221C (Figure 45C). The broad peak at 2.5 nm in NavMs was shifted to 2.75 nm in NsvBa. This peak corresponded to the distance between adjacent monomers in NavMs. The peak at 3.5 nm, which corresponded to the distance across the tetramer in NavMs, was roughly the same as in NavMs A221C. There was an additional distance at approximately 5 nm, which had no corresponding distance in NavMs. It was possible that this larger distance was an artefact associated with the aggregation indicated by gel filtration. However were this the case a broader peak would have been expected, and the raw data should have exhibited high background noise as compared to NavMs measurements, which it did not (Figure 45D). This additional distance was suggestive of a parallelogram conformation, similar to what was seen in the molecular dynamics simulation model of NavMs, and can be observed in the disordered neck model of the C-terminus (Figure 45A). It was also possible that the DEER-EPR spectroscopy measurements had captured both the open and closed states of the channel.

5.8 Introduction of the DDT Binding Site to NsvBa

In order to investigate that the 5 nm distance corresponded to the open conformation of the channel, an additional set of mutations were made to introduce the binding site of the insecticide dichlorodiphenyltrichloroethane (DDT) into NsvBa (Figure 46B). In insect Navs, DDT binds in the cleft between the subdomain III S5 and the subdomain IV S6 helices, stabilising the channel in an open conformation (O'Reilly et al. 2014). As there are no ligands which have been shown to bind prokaryotic Navs

`

and stabilise the open conformation of the channel, this was performed in order to attempt to control the conformation of the channel.

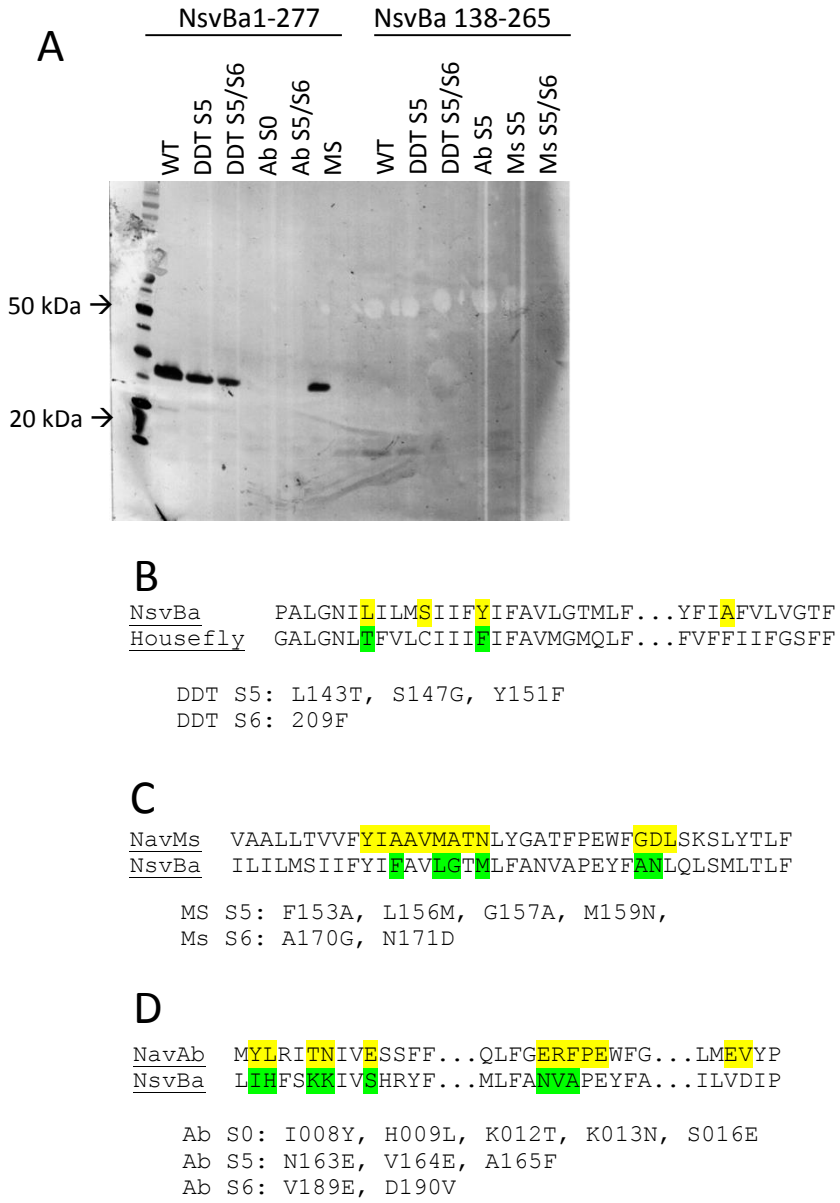

Figure 46: Mutagenesis of WT NsvBa, and NsvBa138-265.
A) Expression trials of mutations. Expression at 3 hours, 37°C, western blot of whole cell lysate. Sequence alignments of NsvBa and B) housefly DIII/DIV, C) NavMs and D) NavAb. Residues required for the DDT binging site (b), or the crystal contacts (c, d) are shown in yellow. Mutations made are shown in green, and listed below each alignment.

Previous work by the Wallace lab has demonstrated that binding of mibifridil and of other pore-blocking drugs did not have an effect on the CD spectra of detergent solubilised Navs. However, an increase the thermal stability of drug bound Navs has been demonstrated (Nurani et al. 2008). In contrast, a 4% decrease in helicity of the NsvBa construct with the DDT binding site was observed after the addition of

`

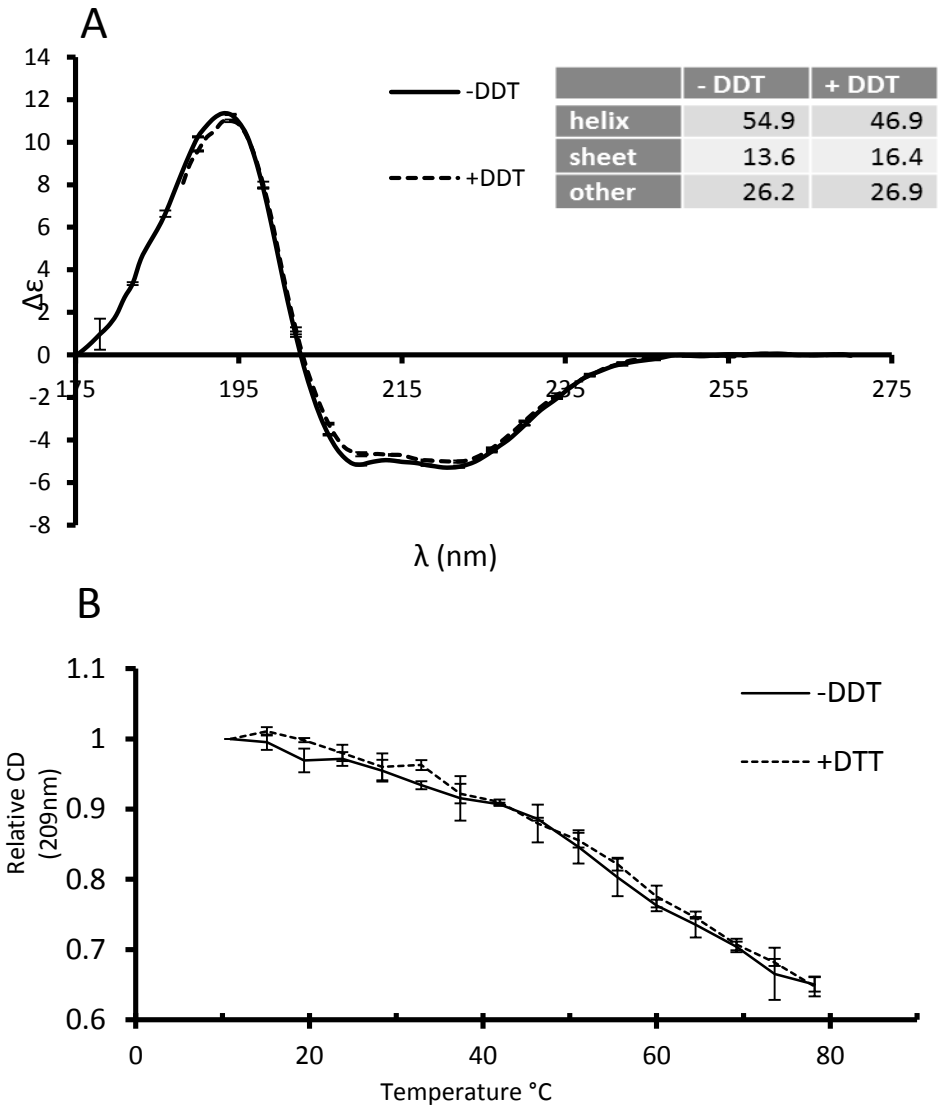

Figure 47: SRCD of NsvBa138-265 DDT S5/S6, With and Without DDT.
A) SRCD spectra of NsvBa138-265 DDT S5/S6, with and without DDT. Secondary structure deconvolutions shown in upper right. B) SRCD thermal unfolding, with and without DDT. Relative CD at 209 nm of constructs in A.

DDT (Figure 47A). However, no difference in thermal stability was observed (Figure 47B). This decrease in helicity would correspond to the transition of five residues from helix to disordered conformation, if it was assumed that 100% of the protein was bound to DDT.

CW-EPR spectroscopic analysis of NsvBa138-265 DDT N229C in the presence of DDT was suggestive of two distinct conformations, one mobile and one more restrained (Figure 46A). This suggested that the channel was in multiple states. DEER-EPR measurements of NsvBa 138-265 DDT N229C in the presence of DDT had a greater signal to noise ratio than the NsvBa138-265 229C (Figure 47E). Comparison of the distance distrubition with that of NsvBa N229C did not indicate any differences (Figure

`

45C). This could have been due a lack of DDT binding, or the result of NsvBa N229C already being stabile in the open conformation. The addition of DDT had no effect on NsvBa 138-265 DDT N229C in SRCD thermal unfolding experiments (Figure 47B).

These results offered no clear indication that the introduction of the DDT binding site enabled binding of DDT to NsvBa. SRCD spectroscopic analysis indicated a change in secondary structure, however this result was not accompanied by the expected thermal stabilisation typical of ligand binding in Navs. CW-EPR spectroscopic analysis demonstrated a less restrained state of the spin label in the presence of DDT, however DEER-EPR spectroscopic analysis found no difference in the corresponding distance distribution.

5.9 NsvBa Crystallisation Trials

Crystallisation trials with WT NsvBa, the NsvBa138 pore construct, and truncation constructs were unsuccessful (Table 5). In an attempt to improve NsvBa's crystallisation prospects, residues from the crystal contacts in the NavMs and NavAb crystal structures were introduced into NsvBa by site directed mutagenesis (Figure 46). Introduction of NavAb contacts was found to completely abolish expression of NsvBa in both the pore and full length constructs. NsvBa pore constructs with NavMs contacts were found to express and purify, however crystallisation trials were unsuccessful.

5.10 Conclusions

Characterisation of the NsvBa C-terminus demonstrated that the neck region was disordered, as seen in the previously characterised NavBh and NavMs. No experimental evidence for helical structure within the neck region of NsvBa was found. However as both helical and disordered neck regions have been demonstrated in different prokaryotic Nav homologues, more work is required to understand how the structure of this region behaves during channel gating. DEER-EPR spectroscopy was successful at measuring distances in the spin labelled NsvBa 138-265 N229C, suggesting a parallelogram conformation rather than the square conformation observed in NavMs. While measurements of spin labels down the length of the C-terminus would allow molecular dynamics simulation of the full structure of this region, the low tolerance to cysteine mutagenesis within the neck region demonstrated that NsvBa would not an ideal target for further experiments.

`

Chapter 6: Discussion and Future Work

6.1 Purification and Solubility of NavBh-RCK Constructs

Despite the publication of multiple Nav crystal structures, NavBh remains a desirable target for structural study, due to its extensive functional characterisation. The replacement of the Nav C-terminus with the MthK RCK domain was envisaged to improve the channel's prospects as a crystallisation target, with added benefits for electrophysiological characterisation and creation of a tool to enable drug screening. In theory, addition of the RCK domain should have improved the solubility of the protein. However, the chimera precipitated at concentrations above 1 or 2 mg/mL, despite both NavBh and MthK being successfully purified under similar conditions. Condition screening was insufficient to improve the low solubility (appendix, Table 4). This suggested that the insolubility was a result of the chimeric design, rather than of properties of either NavBh or the RCK domain.

The only known example of a voltage gate ion channel with a native RCK domain is the eukaryotic channel BK. In BK, it has been shown that the intracellular loops of the voltage sensor interact with the top of the RCK domain (Yuan et al. 2010). This raised the possibility that interaction between the RCK domain and intracellular loops of the NavBh voltage sensor may have contributed to the low solubility/low stability of NavBh-RCK. Removal of the voltage sensor to create the NavBh128-RCK construct did not affect the concentration-dependent precipitation of the protein, demonstrating that such an interaction was not the source of the low solubility (Figure 28). SRCD spectroscopic analyses demonstrated that the channel is correctly folded, however the channel also displayed lower thermal stability in the presence of $CaCl_2$ (Figure 24). This is counter to what was expected, as ligand binding has been shown to stabilise the RCK domain (Dong et al. 2005). This was accompanied by an increase in absorption at low wavelengths, which was possibly associated with protein precipitation (appendix, Figure 49). This instability in the presence of calcium was the first experimental evidence suggesting that the low solubility and precipitation of NavBh-RCK resulted from the activation of the RCK domain.

6.2 Electrophysiology of NavBh-RCK

Electrophysiological characterisation of NavBh-RCK in synthetic lipid bilayers demonstrated that NavBh-RCK was a functional calcium gated sodium channel (Figure

`

25). NavBh-RCK and NavBh128-RCK were both found to support conductance only in the presence of calcium and at alkaline pH, which corresponds to the conditions known to promote the formation and activation of the octomeric gating ring. Furthermore, while channel activity was unreliable, in this study it was shown that both constructs were more active than their WT counterparts (A. Powl, unpublished results). In the absence of a voltage pulse protocol, NavBh128 was more active than the full length WT NavBh (A. Powl, unpublished results), as the voltage sensor seems to hold the channel in a closed position in the absence of a membrane depolarisation event. The same held true for the NavBh-RCK and NavBh128-RCK. While removal of the voltage sensor did not improve channel solubility, it did improve channel activity, despite extremely low expression of the soluble RCK domain (Figure 25, Figure 29). This offered further evidence that, in the absence of a voltage pulse protocol, the voltage sensor kept the channel in a closed position.

In the presence of calcium, both NavBh-RCK and NavBh128-RCK were characterised by sparse periods of intense activity, in which the channel quickly opened and closed repeatedly (Figure 25, Figure 29). WT NavBh has previously been shown to open and then quickly inactivate in response to a voltage pulse protocol, in a single gating event (Kuzmenkin et al. 2004; Ren et al. 2001). In the presence of calcium, MthK was characterised by long periods of activity during which the channel rapidly opens and closes (Jiang et al. 2002; Li et al. 2007). These long stretches of activity were attributed to the RCK being activated and staying in an activated position, while the MthK pore underwent repeated inactivation and recovery through a mechanism thought to be similar to prokaryotic Nav inactivation (Li et al. 2007). Thus, the periods of activity seen in NavBh-RCK were the result of prolonged activation of the RCK domain, and short, inter-burst events during these periods was a property of the NavBh pore. This confirmed that the RCK domain was capable of controlling Nav channel gating.

NavBh-RCK activity was very unreliable as compared to KcsA in the same system, with similar protein ratios (Kalsi et al. 2014). It was initially thought that this was due to the presence of the voltage sensor. However, removal of the voltage sensor almost completely abolished expression of the soluble RCK domain from the secondary start codon (Figure 15). This low concentration of soluble RCK was compounded by the 200 fold dilution of the soluble RCK domain during recordings.

`

Despite this, NavBh128-RCK was more active than the full length NavBh-RCK, demonstrating how effective the voltage sensor is at maintaining the channel in a closed position under a holding potential. This result also raised the possibility that, unlike MthK, the soluble RCK subunit may not have been necessary for channel activity.

It was initially assumed that the observed activity of NavBh-RCK and NavBh128-RCK was the result of calcium-driven assembly and activation of the octomeric RCK gating ring. Therefore, the infrequency of gating events would have been the result of the low effective concentration of the RCK domain. MthK has previously been characterised at concentrations of $CaCl_2$ less than those which were used here, and was shown to be active (Jiang et al. 2002; Li et al. 2007), and the further addition of $CaCl_2$ did not improve channel activity. Increased concentrations of soluble RCK domain resulted in irregular conductance, and activity that was followed shortly by rupture of the lipid membrane (Figure 31A), and channel activity displayed a directionality that was not present in previous recordings (Figure 31B). This suggested that the stable activity demonstrated by NavBh128-RCK, at the low concentration of the soluble RCK domain was the result of activation of an incomplete gating ring, and that the unstable activity a property of the full gating ring. This offered a plausible mechanism for the concentration-dependent precipitation displayed by NavBh-RCK during purification. At higher concentrations, formation of the octomeric complex would have been more likely. Removal of the soluble RCK domain by the M107I mutation would not have been expected to affect this, as the MthK crystal structure demonstrated that the octomeric gating ring can be formed entirely from covalently bound RCK subunits of two back to back tetramers. Furthermore, this mechanism is supported by the lower thermal stability of NavBh-RCK in the presence of calcium (Figure 24).

6.3 Homology Modelling of an Open and Closed Nav-RCK

While no closed structure of MthK was available, comparison of the open MthK and closed KcsA crystal structures has long been used to speculate on the mechanism of channel gating in prokaryotic K^+ channels, and by homology, Navs. Comparison of KcsA and MthK revealed a 30° bend in the C-terminal half of the M2 helix (homologous to the Nav S6) around a conserved glycine hinge (Chakrapani & Perozo 2007). Prior to

`

the publication of the open Nav structure, it was assumed that Navs would share this mechanism. It had previously been shown that mutation of the glycine hinge residue to serine reduced conformational flexibility in NavBh (O'Reilly et al. 2008), and also that mutating the residue to proline reversed the voltage dependent gating (Zhao et al. 2004). The function of this hinge has also been investigated by molecular dynamics (Barber et al. 2012). However, the more recent publication of both open and closed Nav structures suggested a mechanism in which the S6 helix rotates, and the pore opens with an iris like motion, rather than bending of the S6 at the glycine hinge (Payandeh et al. 2011; McCusker et al. 2012). This is further supported by the observation that in the majority of prokaryotic Navs, the hinge which is strongly conserved in prokaryotic K^+ channels is not present.

Superposition of the closed NavAb and KcsA pores demonstrated a similar position for the bottom half of the NavAb S6 helix and the homologous M2 helix in KcsA (Figure 35). Superposition of the open MthK and NavMs pores demonstrated a large difference in the position of the end of the S6 and M2 helices (Figure 27). In MthK, the end of the M2 helix was displaced so that there is a difference of almost 10 Å in the position of the last residue of the MthK M2 helix and the last residue NavMs S6 helix. It was plausible that the translocation of the RCK domain upon activation by calcium in the NavBh-RCK chimera would have pulled the end of the NavBh S6 helix in such a way as to facilitate the large bending seen in the MthK crystal structure, rather than the iris-like motion demonstrated by the NavAb/NavMs crystal structures. What affect this would have had on the NavBh pore was difficult to speculate on, as the region linking the RCK to the end of the M2 helix was not resolved in the MthK crystal structure. Subsequent publication of the structure of the homologous GSuK (Kong et al. 2012), in which the linker region was resolved, in combination with the structure of the activated BK gating ring (Yuan et al. 2010) allowed for homology modelling and retrospective analysis that was not possible at the time of the work.

The lack of resolution in the region linking the MthK pore to the RCK domain originally lead to the assumption that this region was simply a disordered loop. However, *ab initio* modelling of the missing 19 residues into the MthK crystal structure as a loop suggested the necessity of structure within this region (Figure 34). Homology modelling based on the GSuK and BK gating ring crystal structures demonstrated that this region likely associated closely with the top of the RCK domain, leaving only a

`

short, inflexible linker region connecting the RCK domain to the base of the pore (Figure 35). Combined with the previous structural analyses demonstrating a much larger opening motion by the K^+ channel M2 helix than was predicted for the homologous Nav S6 helix, these results suggested that activation of the RCK gating ring would pull the Nav S6 helix out of position in the NavBh-RCK chimera. It was difficult to speculate what effect this would have on the protein, however it did offer a plausible hypothesis for the concentration dependent precipitation observed in the purification of all Nav-RCK constructs.

As the octomeric gating ring forms dynamically in solution, concentrating the protein would have increased the probability of its formation, and thus at low concentrations the soluble RCK units would have been less likely to form the octomeric gating ring. This effect would still have been expected to occur even in the absence of the soluble RCK domain (such as for the M107I constructs), as the crystal structure of MthK demonstrated that an octomeric gating ring can be formed from two back-to-back channel-RCK tetramers. Furthermore, the lack of expression of NavMs-RCK was in line with this hypothesis. The presence of the conserved glycine gating hinge in NavBh may have allowed the channel to tolerate to a degree the tension placed on it by the RCK domain. NavMs lacks the glycine residue conserved in Kvs, and if this were the case would likely not have tolerated it at all. NsvBa does have this conserved residue, and NsvBa-RCK did express, but precipitated out of solution during membrane solubilisation.

It has previously been shown that acidic pH locks the soluble RCK domain into dimers, preventing formation of the RCK gating ring (Kuo et al. 2007). Low pH was not seen to improve channel solubility however. Additionally the presence of EGTA during the concentration step, which should prevent activation of the RCK domain, had no effect. Both of these results were seemingly at odds with the hypothesis that activation of the octomeric gating ring was responsible for the precipitation of NavBh-RCK. However, it should be noted that the work characterising the dynamic behaviour of the RCK oligomerisation was performed entirely using the soluble subunits. No comparable studies have been performed on the dynamic oligomerisation of the RCK bound to the MthK channel. It was also plausible that the dimerization of the RCK domain at low pH placed unanticipated stress on the pore, contributing to the low solubility of NavBh-RCK.

`

The electrophysiological characterisation which demonstrated that NavBh-RCK is a calcium gated sodium channel seemed to contradict the hypothesis that activation by the octomeric gating ring destabilised NavBh-RCK. It was possible that activation of an incomplete gating ring would reduce the tension placed upon the channel, as compared to activation of a full octomeric gating ring. This could have allowed the stable gating observed at low concentrations of RCK. It also explained why NavBh128-RCK, which had a low concentration of soluble RCK and no voltage sensor, demonstrated the best activity and most stable conductance. It is unlikely the activity observed was a result of random motion of the channel, since if this were the case activity would have been observed regardless of the presence or absence of calcium. It also would not have displayed the rapid opening and closing within long periods of activity characteristic of the RCK domain.

6.4 Expression and Purification of NsvBa

Initial results demonstrated successful recombinant expression and purification of WT NsvBa in *E. coli* (Figure 37). Truncation of the WT NsvBa C-terminus resulted in localisation of the expressed protein to inclusion bodies, which suggested that the C-terminus may have a role in stabilising NsvBa or ensuring accurate folding. Truncations of the pore-only construct starting from residue 138 were found to localise to the membrane correctly, however as was previously found in NavBh, removal of the voltage sensor had a negative effect expression (Figure 40). Interestingly, C-terminal truncation of both the pore only and full length NsvBa exhibited shifted band sizes during SDS-PAGE, indicative of an increase in hydrodynamic volume of the protein. Abnormal running behaviour of prokaryotic Navs in SDS-PAGE or gel filtration is not uncommon, however it has not previously been associated with truncations of the C-terminus. Membrane proteins are generally known to have high stability, and NavBh retained more than 80% of the channels helical structure during thermal unfolding studies (Powl et al. 2012). Abnormal behaviour during SDS-PAGE has generally been attributed to this unusually high stability, however this did not offer an explanation for the increase in size of the band on the gel after the removal of C-terminal residues, which should have reduced the size of the protein. Modified NsvBa constructs eluted in single peak with a predicted size > 600 kDa, rather than at the expected sizes of their respective tetramers (Figure 41). Despite this, pore-only NsvBa constructs

`

demonstrated no tendency towards precipitation, and both SRCD and EPR experiments were successful.

The abnormal band size of the C-terminal truncations during SDS-PAGE is particularly interesting, given the conflicting structural predictions of the C-terminus, and the reduction in thermal stability of NsvBa truncations at 239 and 234 (Figure 43). While SRCD spectroscopic analyses found no transition in secondary structure within the rest of the protein correlating with truncation of the coiled-coil domain, it was possible that truncation of the C-terminus affected the hydrodynamic volume of the detergent solubilised protein in unexpected ways. If the coiled-coil played a role in restraining the disordered neck region, its truncation could have been responsible for a shift in the hydrodynamic volume of the detergent solubilised protein. However, the tetramer disassociated during SDS-PAGE, which would have disrupted the coiled-coil, and thus stabilisation by the coiled-coil should not have been a factor. Alternatively, the NsvBa C-terminus may have had a role in thermal stabilisation of NsvBa, a hypothesis supported by the low thermal stability of the C-terminal truncations at 234 and 239. Previous thermal unfolding studies of NavBh truncations demonstrated that its high thermal stability was a property of the transmembrane region of the channel, and not of the C-terminus (Powl et al. 2012). Despite the high homology between NavBh and NsvBa, these results suggested that the same is not true of NsvBa. Another study has also demonstrated that the Nav C-terminus stabilises interactions between the subunits (Mio et al. 2010). However the unusual behaviour exhibited by NsvBa was not dependent on subunit interactions, as the tetramer disassociated during SDS-PAGE.

6.5 SRCD Spectroscopic Analyses of the NsvBa C-Terminus

SRCD spectroscopic analyses successfully determined the secondary structure of the NsvBa C-terminus. Results significantly correlated with the disordered neck model of NsvBa (Figure 42). No indication of a helix to disorder transition was observed. Nor did the results suggest a mixed population of helical and disordered conformations of the neck region within the sample, which would have been suggested had the calculations of the residues removed fallen somewhere in between the two predictions.

`

Previous work in NavBh determined that truncation of the C-terminus increased the helical content retained during thermal unfolding analyses. This demonstrated that the NavBh C-terminus has a low thermal stability, and its removal wasn't observed to have a large effect on the stability of transmembrane regions of the protein (Powl et al. 2012). NsvBa displayed remarkably different behaviour during thermal unfolding experiments (Figure 43). Truncation constructs of NsvBa 138-265, NsvBa 138-259, and NsvBa 138-250 all displayed very similar thermal stability to the pore construct with the full length C-terminus (138-277). However, the two shortest truncations, NsvBa 138-239 and NsvBa 138-134, both displayed significantly reduced thermal stability. This reduction of thermal stability was not observed in the homologous truncation of NavBh. In NavBh, this region consisted of a series of charged residues thought to be important for assembly of the tetramer. This charged region is conserved in NsvBa, and alignment of NavBh and NsvBa offered no explanation as to the different thermal stability (Figure 36). It should be noted that the previously discussed shifted band size during SDS-PAGE was less in these last two truncations. This further suggested that the shifted band size was a result of contributions of the C-terminus to the thermodynamic stability of NsvBa.

6.6 EPR Spectroscopic Studies of the NsvBa C-Terminus

A previous study utilised EPR Spectroscopy in conjunction with molecular dynamics simulations to generate a model of the NavMs C-terminus (Bagnéris et al. 2013). In this study, SRCD analyses of serial truncations has confirmed a disordered neck model of NsvBa. In the hopes of further improving that model, EPR spectroscopic studies of NsvBa were performed.

The introduction of cysteine residues within the neck region of NsvBa for spin labelling found that, unlike in NavMs, mutations within this region had a strong negative effect on expression (Figure 44A, B). Residue N229 was predicted in both the disordered neck and helical neck models of NsvBa to be the final residue of the S6 helix, and mutation of this residue and the following two residues V230, and E231, was tolerated well. However, this was followed by a stretch of mostly charged residues, mutation of which greatly reduced channel expression (Figure 44B). This was unsurprising, as truncation of these residues has already been shown to reduce expression. These results suggested that the C-terminus of NsvBa is more sensitive to

`

modification than that of other characterised homologues, and that the NsvBa C-terminus may have had a distinct functional role in stabilising the protein.

CW-EPR spectroscopy of nitroxide spin labelled NsvBa138-265 N229C indicated that the spin label was in a restricted conformation, as was seen at the homologous position in NavMs (Figure 45B). This offered further support for the NsvBa homology models, which both predicted that this position was the final residue of the S6 helix. DEER-EPR spectroscopy however demonstrates that the distance distribution of the spin labels at this position was remarkably different from the measurements at the homologous position in NavMs (Figure 45C). The presence of a distance at approximately 5 nm that was not observed in NavMs suggested a parallelogram conformation, as was observed in the molecular dynamics simulation of NavMs, and could be seen in the disordered neck model of NsvBa (Figure 45A). Alternatively, this distance could have arisen due to the presence of both the open and closed conformation of the channel. It was difficult to speculate further as to the source of this extra distance, as the low tolerance of the NsvBa C-terminus to mutation prevented spin labelling at additional sites of interest. Furthermore, the possibility that the distance was an artefact correlating with the unusual thermal stability or running size of the NsvBa truncations was difficult to exclude without measurements of spin labels throughout the neck region of the C-terminus. However, these results further suggested that, despite having a similar disordered neck region, the structure of the NsvBa C-terminus had distinct differences from that of NavMs.

6.7 Introduction of DDT Binding Site into NsvBa

If successful, the ability to use DDT to control the conformation of the detergent solubilised channel would have been a powerful tool. While mutagenesis to introduce the residues shown to form the DDT binding site was successful, DDT binding could not be confirmed. CW-EPR spectroscopy indicated two distinct mobilities of the spin labelled residue in the presence of DDT, which could have resulted from the channel's open and closed conformations. DEER-EPR spectroscopic measurements however demonstrated no shift in the distances distribution of spin labelled NsvBa with the DDT binding site in the presence of DDT (Figure 45C). This suggested that either DDT was not binding, or that the resting equilibrium of the detergent solubilised pore already favoured an open conformation, and thus DDT binding had no effect.

`

SRCD spectroscopic analysis demonstrated a decrease in helicity of the protein in the presence DDT, however the expected increase in thermal stability typically associated with ligand binding was not observed (Figure 47). While confirmation of DDT binding would best have been observed via electrophysiological characterisation, the preliminary spectroscopic results were not conclusive enough to pursue such studies.

6.8 Future Work

Further Investigations of the NavBh-RCK Fusion Chimera

The hypothesis that the NavBh pore was unable to tolerate the gating mechanism imposed upon it by the RCK domain as the cause of the concentration dependent precipitation displayed by the protein could be investigated through several different methodologies. It has been shown in BK that shortening or lengthening of the linker region between the pore and RCK domain affects channel activity, both in the presence and in the absence of calcium (Niu et al. 2004). Lengthening the linker could reduce the tension placed on the pore by the RCK domain, preventing disruption of the pore stability by activation of the RCK domain. Further improvements could include creating a NavBh-RCK construct with second RCK domain in tandem rather than expressed from a secondary start codon, as seen in the GSuK and BK channels. This could bypass many of the complicating factors caused by the presence of the dynamically oligomerising soluble RCK domain during purification and characterisation of NavBh-RCK.

Alternatively, an *in silico* approach could utilise molecular dynamics to model the effects of RCK gating ring activation on the attached NavBh pore in the Nav-RCK models. This would directly address the hypothesis that the NavBh pore cannot tolerate activation of the full octomeric gating ring. It could also be used to investigate whether the NavBh pore better tolerates activation by an incomplete RCK gating ring. However, given that the NavBh-RCK with the full octomeric gating ring is 328 kDa without a lipid bilayer or detergent micelle, such an approach would be very computationally intensive. It would also be of limited scientific value, given the multiple prokaryotic Nav structures published since this project's inception. Given this, further efforts to obtain a crystal structure of NavBh would be best allocated to exploration of new crystallisation techniques, such as crystallisation in lipid bicelles, lipid sponge phase, and lipid cubic phase.

`

Further Investigations of NsvBa

While the publication of multiple Nav crystal structures has led to advances in our understanding of their structure, much work remains to be done. In particular, the structural transitions associated with channel gating are not well understood. While NsvBa was an attractive target for structural study, it was not found to crystallise in any of the conditions tested. SRCD spectroscopic analyses of serial truncations demonstrated that the neck region of the NsvBa C-terminus was disordered, and found no indication that the region is capable of transition between helical and disordered conformations. However, the lack of ability to control channel conformation made it difficult to confirm that such a transition would not occur during channel gating. Additional experiments could attempt to further modify a prokaryotic Nav to allow the binding of DDT or one of its homologues, or to find other ways of controlling channel conformation. Disulphide crosslinking of the pore, as was used to obtain the NavAb structure (Payandeh et al. 2011), could be useful to stabilise the channel in a closed position. However, the use of disulphide crosslinking would preclude the use of EPR spectroscopy, as the disulphide cross-linked residues would be reduced and labelled along with the residue targeted for spin labelling. Bifunctional spin labels could offer a potential solution, allowing simultaneous cross-linking and spin labelling, and their use for the study of membrane proteins is under further development (Sahu et al. 2013). A method to stabilise the channel in both open and closed states would allow the direct testing of the hypothesis that channel gating involves a helix to disorder transition within the C-terminus, utilising SRCD spectroscopy and EPR spectroscopy. Furthermore, conformational control of the channel should improve the channels crystallisation prospects, as was discussed in relation to the fusion chimera NavBh-RCK.

In this study, a modelling approach was utilised to predict the structure of the NsvBa C-terminus, based on two conflicting bioinformatics predictions. SRCD analyses of a series of C-terminal truncations successfully validated the disordered neck model. Further experiments could be pursued to investigate the unusual properties of the NsvBa C-terminus, and to improve upon this model. Neither SRCD spectroscopic studies nor EPR spectroscopic studies identified the cause of shifted band size during SDS-PAGE of the NsvBa C-terminal truncations, a phenomenon that raises questions about the potential role of the NsvBa C-terminus in thermal stabilisation of the

`

channel. This is a trait which has not previously been identified in a prokaryotic Nav, and bears further investigation.

Despite the recent publication of multiple crystal structures, prokaryotic Navs have historically been challenging targets for structural study due to their large hydrophobic transmembrane regions, difficulty in their recombinant expression and purification, and inherent flexibility. New techniques for crystallisation, such as lipid cubic and lipid sponge phase methods should be further explored for the crystallisation of Navs (Caffrey 2015). The lipid bicelle method was key to the first published Nav crystal structure (Payandeh et al. 2011), and such techniques may yield structures of other homologues. Alternative methods of structural study, such as DEER-EPR spectroscopy, also hold great promise for the study of Navs, enabling observation of the dynamic range of protein conformation which cannot be seen in a static crystal structure.

`

Appendix

>NavBh-RCK
MKMEARQKQNSFTSKMQKIVNHRAFTFTVIALILFNALIVGIETYPRIYADHKWLFYRI
DLVLLWIFTIEIAMRFLASNPKSAFFRSSWNWFDFLIVAAGHIFAGAQFVTVLRILRVL
RVLRAISVVPSLRRLVDALVMTIPALGNILILMSIFFYIFAVIGTMLFQHVSPEYFGNL
QLSLLTLFQVVTLESWASGVMRPIFAEVPWSWLYFVSFVLIGTFIIFNLFIGVIVNNVE
KEQMKLMGLIDVAKSRHVVICGWSESTLECLRELRGSEVFVLAEDENVRKKVLRSGANF
VHGDPTRVSDLEKANVRGARAVIVDLESDSETIHCILGIRKIDESVRIIAEAERYENIE
QLRMAGADQVISPFVISGRLMSRSIDDGYEAMFVQDVLAEESTRRMVEVPIPEGSKLEG
VSVLDADIHDVTGVIIIGVGRGDELIIDPPRDYSFRAGDIILGIGKPEEIERLKNYISA
SSGLVPRGSHHHHHH

>NavMS-RCK
SVAALLTVVFYIAAVMATNLYGATFPEWFGDLSKSLYTLFQVMTLESWSMGIVRPVMNV
HPNAWVFFIPFIMLTTFTVLNLFIGIIVDAMAIEQMKLMGLIDVAKSRHVVICGWSEST
LECLRELRGSEVFVLAEDENVRKKVLRSGANFVHGDPTRVSDLEKANVRGARAVIVDLE
SDSETIHCILGIRKIDESVRIIAEAERYENIEQLRMAGADQVISPFVISGRLMSRSIDD
GYEAMFVQDVLAEESTRRMVEVPIPEGSKLEGVSVLDADIHDVTGVIIIGVGRGDELII
DPPRDYSFRAGDIILGIGKPEEIERLKNYISA

>NsvBa-RCK
MQKQSLLIHFSKKIVSHRYFTRIIITLILFNALLVGLETYPALRHEYGSLFHVLDVILL
WIFTLEILTRFLATTPKKDFFKGGWNWFDTIIVLSSHIFVGGHFITVLRILRVLRVLRA
ISVIPSLRRLVDALMLTIPALGNILILMSIIFYIFAVLGTMLFANVAPEYFANLQLSML
TLFQIVTLDSWGSGVMRPILVDIPWAWTYFIAFVLVGTFIIFNLFIGVIVNNVEKMAIE
QMKLMGLIDVAKSRHVVICGWSESTLECLRELRGSEVFVLAEDENVRKKVLRSGANFVH
GDPTRVSDLEKANVRGARAVIVDLESDSETIHCILGIRKIDESVRIIAEAERYENIEQL
RMAGADQVISPFVISGRLMSRSIDDGYEAMFVQDVLAEESTRRMVEVPIPEGSKLEGVS
VLDADIHDVTGVIIIGVGRGDELIIDPPRDYSFRAGDIILGIGKPEEIERLKNYISA

>MthK
PATRILLLVLAVIIYGTAGFHFIEGESWTVSLYWTFVTIATVGYGDYSPSTPLGMYFTV
TLIVLGIGTFAVAVERLLEFLINREQMKLMGLIDVAKSRHVVICGWSESTLECLRELRG
SEVFVLAEDENVRKKVLRSGANFVHGDPTRVSDLEKANVRGARAVIVDLESDSETIHCI
LGIRKIDESVRIIAEAERYENIEQLRMAGADQVISPFVISGRLMSRSIDDGYEAMFVQD
VLAEESTRRMVEVPIPEGSKLEGVSVLDADIHDVTGVIIIGVGRGDELIIDPPRDYSFR
AGDIILGIGKPEEIERLKNYISA

>NsvBa
MQKQSLLIHFSKKIVSHRYFTRIIITLILFNALLVGLETYPALRHEYGSLFHVLDVILL
WIFTLEILTRFLATTPKKDFFKGGWNWFDTIIVLSSHIFVGGHFITVLRILRVLRVLRA
ISVIPSLRRLVDALMLTIPALGNILILMSIIFYIFAVLGTMLFANVAPEYFANLQLSML
TLFQIVTLDSWGSGVMRPILVDIPWAWTYFIAFVLVGTFIIFNLFIGVIVNNVEKANED
EVKDKVKEKEEAAQKQMDSLHEELKEIKQYLKSIEKQNRSS

Table 1: Amino Acid Sequences of the Chimeric Nav-RCK Constructs.
NavBh-RCK, NavMs-RCK, and NsvBa-RCK, plus MthK and NsvBa.

`

Construct or Mutation	Forward primer	Reverse Primer
NavBh-RCK C-terminal His tag addition	AGA AGG AGA TAT ACC ATG AAA ATG GAA GCT	GTT AGC AGC CGC ATC CTT ATC AGT GGT GGT GGT GGT GGT GGC TGC CGC GAG GTA CTA GGC CGC TGC TCG CGC TAA TAT AGT TCT TCA GGC GC
NavBh-RCK N-terminal His tag removal	AGA AGG AGA TAT ACC ATG AAA ATG GAA GCT	AGC TTC CAT TTT CAT GGT ATA TCT CCT TCT
Soluble RCK	CTG GTT CCT CGT GGC AGC CAC ATG GGC CTG ATT GAT GTG GCT AAA TC	GAT TTA GCC ACA TCA ATC AGG CCC ATG TGG CTG CCA CGA GGA ACC AG
NavBh-RCK M107I	TAA TAA TGT CGA GAA AGA ACA GAT AAA GTT A	TAA CTT TAT CTG TTC TTT CTC GAC ATT ATT A
NavBh T20A	TCC TGA TTG GAG CGT TTA TCA TTT TTA ATC TGT TC	ATG ATA AAC GCT CCA ATC AGG ACA AAG CTG AC
NavMs-RCK	GAT GCA ATG GCA ATC ACC AAG GAA CAG ATG AAG TTA ATG GGC CTG ATT GA	CAA TCA GGC CCA TTA ACT TCA TCT GTT CTT TTT CAA CGT TAT TGA CGA TAA CT
NsvBa- RCK	TAA CTT TAA GAA GGA GAT ATA CCA TGC AAA AAC AGT CCC TTC TCA TTC	CAA TCA GGC CCA TTA ACT TCA TCT GTT CTT TTT CAA CGT TAT TGA CGA TAA CT
NsvBa A249C	AGA AGC CTG CCA AAA ACA GAT GGA TTC ACT AC	GTT TTT GGC AGG CTT CTT CCT TTT CTT TTA CTT TAT C
NsvBa E258C	CTA CAT TGC GAG CTA AAA GAA ATC AA	AGC TCG CAA TGT AGT GAA TCC ATC
NsvBa N229C	TCA ACT GCG TTG AAA AAG CGA ATG AAG ACG	CTT TTT CAA CGC AGT TGA CGA TAA CTC CAA TAA
NsvBa K268C	CAT GAA GAG CTA TGC GAA ATC AAA CAA TAT TTA AAA TCA ATC GAA AAA C	ATT GTT TGA TTT CGC ATA GCT CTT CAT GTA GTG AAT CCA TCT GTT TTT G
NsvBa V230C	AAT AAC TGT GAA AAA GCG AAT GAA GAC GA	GCT TTT TCA CAG TTA TTG ACG ATA ACT C
NsvBa E231C	TAA CGT TTG CAA AGC GAA TGA AGA CGA AG	TTC GCT TTG CAA ACG TTA TTG ACG ATA ACT C
NsvBa A223C	CGT TGA AAA ATG TAA TGA AGA CGA AGT AAA AGA TAA AGT	TCT TCA TTA CAT TTT TCA ACG TTA TTG ACG ATA ACT CCA
NsvBa K232C	TTG AAT GTG CGA ATG AAG ACG AAG TAA	TTC ATT CGC ACA TTC AAC GTT ATT GAC
NsvBa N234C	AAA AGC GTG TGA AGA CGA AGT AAA AGA TAA	TAC TTC GTC TTC ACA CGC TTT TTC AAC GTT
NsvBa E235C	AAG CGT GTG AAG ACG AAG TAA AAG ATA A	CGT CTT CAC ACG CTT TTT CAA CGT T
NsvBa D236C	GAA TGA ATG CGA AGT AAA AGA TAA AGT	TAC TTC GCA TTC ATT CGC TTT TTC AAC
NsvBa E237C	GAA TGA AGA CTG TGT AAA AGA TAA AGT AAA A	ATC TTT TAC ACA GTC TTC ATT CGC TTT TTC
NsvBa-NavAb contacts- S0	TAT CTT TTT AGT ACA AAC ATT GTT GAG CAC CGT TAT TTT ACA AGA ATT ATT ATT ACT TTA ATT TT	CTC AAC AAT GTT TGT ACT AAA AAG ATA GAG AAG GGA CTG TTT TTG CAT ATG G
NsvBa- NavAb contacts S5	GTT ATT TGC GGA GAG ATT CCC TGA ATA TTT TGC CAA TCT CCA A	GAA TCT CTC CGC AAA TAA CAT CGT ACC TAA TAC GGC
NsvBa-NavAb contacts S6	ATC TTA GAG GTT ATC CCA TGG GCA TGG ACT TAT T	CCC ATG GGA TAA CCT CTA AGA TCG GCC TCA TTA CAC C
NsvBa-NavMs contacts S51	GCT GCC GTA ATG GCT ACG AAC TTA TTT GCG AAT GTA GCT CCT GAA T	GTT CGT AGC CAT TAC GGC AGC TAT ATA GAA AAT AAT GCT CAT TAA AAT TAA AAT ATT
NsvBa-NavMs contacts S52	GAA TAT TTT GGC GAT CTC CAA CTC TCA ATG CTG ACT CTC TTC	AGT TGG AGA TCG CCA AAA TAT TCA GGA GCT ACA TTC GCA AA
NsvBa DDTS5	ACA ATT TTA ATG GGC ATT ATT TTC TTT ATA TTT GCC GTA TTA GGT ACG ATG TTA	AAG AAA ATA ATG CCC ATT AAA ATT GTA ATA TTT CCT AAA GCA GGA ATC GTT AAC

`

NsvBa DDTS6	CTT ATT TTA TTT TCT TTG TGT TAG TCG GGA CCT TCA TTA	CTA ACA CAA AGA AAA TAA AAT AAG TCC ATG CCC ATG G
NsvB128 DDTS5	ACA ATT TTA ATG GGC ATT ATT TTC TTT ATA TTT GCC GTA TTA GGT ACG ATG TTA	AAG AAA ATA ATG CCC ATT AAA ATT GTA ATA TTT CCT AAC ATA TGG CTG CCG CGC
NsvBa 234-stop	CAA TAA CGT TGA AAA AGC GTA AGA AGA CGA AGT AAA AGA TAA AG	CTT TAT CTT TTA CTT CGT CTT CTT ACG CTT TTT CAA CGT TAT TG
NsvBa 239-stop	CGA ATG AAG ACG AAG TAT AAG ATA AAG TAA AAG AAA AGG	CCT TTT CTT TTA CTT TAT CTT ATA CTT CGT CTT CAT TCG
NsvBa 250-stop	GAA AAG GAA GAA GCC GCC TAA AAA CAG ATG GAT TCA CTA C	GT AGT GAA TCC ATC TGT TTT TAG GCG GCT TCT TCC TTT TC
NsvBa 259-stop	TGA AGA GTA AAA AGA AAT CAA ACA ATA TTT AAA ATC	TTT CTT TTT ACT CTT CAT GTA GTG AAT CCA TC
NsvBa 265-stop	GAG CTA AAA GAA ATC AAA TAA TAT TTA AAA TCA ATC GAA AAA C	GTT TTT CGA TTG ATT TTA AAT ATT ATT TGA TTT CTT TTA GCT C
NsvBa138 (pore)	TAA CTT TAA GAA GGA GAT ATA CCA TGT TAG GAA ATA TTT TAA TTT TAA TGA GCA TTA TT	TAA CTT TAA GAA GGA GAT ATA CCA TGT CTT TAA GAA GAC TCG TTG ACG CCT TAA TGT

Table 2: List of Constructs and Primers.
List of constructs and corresponding PCR primers used for their generation.

`

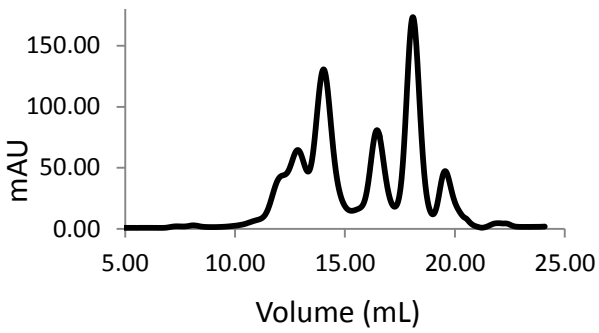

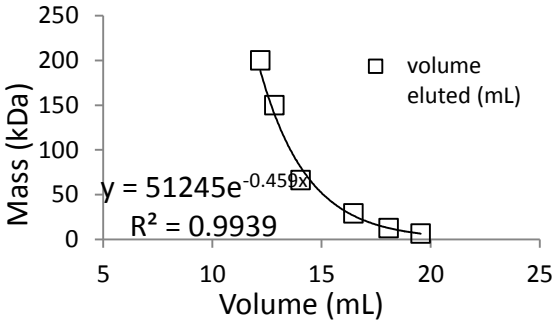

Protein	Molecular Mass (kDa)	volume eluted (mL)
B amylase	200	12.2
Alcohol Dehydrogenase	150	12.84
BSA	66	14.04
Carbonic Annhydrase	29	16.46
Cytochrome C	12.4	18.08
Aprotin	6.5	19.55
Void Volume		7.5

Figure 48: Superdex 200 10/300, Gel Filtration Calibration.
Gel filtration standards, run on GE Superdex 200 10/300 in 0.2M NaCl, 20mM sodium phosphate, pH 7.4. Gel filtration profile (left), and Mass/Volume curve (right). Table of proteins, and their molecular mass, and elution volume (bottom).

`

Construct	Buffer	pH	Ions	Detergent
NavBh-RCK	Sodium phosphate buffered saline	6.8	0.2 M NaCl	DDM, CYMAL5
NavBh-RCK	Sodium Phosphate	7.2	0.2 M NaCl	DDM, CYMAL5
NavBh-RCK	Sodium Phosphate	7.4	0.2 M NaCl	DDM, CYMAL5
NavBh-RCK	Tris	8.0	0.2 M NaCl	DDM, CYMAL5
NavBh-RCK	Tris	8.0	0.5 M NaCl	DDM, CYMAL5
NavBh-RCK	Tris	8.0	0.5 M NaCl	DDM, DDM
NavBh-RCK	Tris	8.0	0.5 M NaCl	DM, DM
NavBh-RCK	Tris	8.0	0.5 M NaCl	DDM, LDAO
NavBh-RCK	Tris	8.0	0.5 M KCl	DDM, CYMAL5
NavBh-RCK	PBS	6.8	0.2 M NaCl	DDM, CYMAL5
NavBh-RCK	Sodium Phosphate	7.4	0.2 M NaCl	DDM, CYMAL5
NavBh-RCK M107I	Sodium phosphate buffered saline	8.0	0.5 M NaCl	DDM, CYMAL5
NavBh-RCK M107I	Sodium Phosphate	8.0	0.5 M NaCl, 100 mM $CaCl_2$	DDM, CYMAL5
NavBh-RCK M107I	Tris	8.0	0.5 M NaCl, 50 mM EDTA	DDM, CYMAL5
NavBh-RCK	Tris	8.0	0.5 M NaCl, 50 mM EGTA	DDM, CYMAL5
NavBh-RCK	Tris	7.4	0.5 M NaCl	DDM, CYMAL5
NavBh-RCK	Tris	8.0	0.5 M NaCl	DDM, CYMAL5
NavBh128-RCK	Sodium Phosphate	8.0	0.5 M NaCl	DDM, CYMAL5
NavBh128-RCK	Tris	8.0	0.5 M NaCl	DDM, CYMAL5
NavBh128-RCK M107I	Tris	8.0	0.5 M NaCl	DDM, CYMAL5
NavBh128-RCK M107I	Tris	8.0	0.5 M NaCl, 100mM $CaCl_2$	DDM, CYMAL5
NavBh128-RCK M107I	Tris	8.0	0.5 M NaCl, 50 mM EGTA	DDM, CYMAL5
NavBh128-RCK M107I + RCK	Tris	8.0	0.5 M NaCl	DDM, CYMAL5

Table 3: Conditions Screened for NavBh-RCK Spin Column Concentration.
Conditions screened for IMAC purification and spin column concentration of NavBh-RCK constructs. The first detergent listed was used for membrane solubilisation, which was exchanged for the second was exchanged during IMAC washing. In all conditions, precipitation was observed during concentration.

`

Construct	Concentration (mg/mL)	Screen	Temperature (°C)
NavBh-RCK M107I	3.2	memgold	4
NavBh-RCK M107I	3.2	memgold	16
NavBh-RCK M107I	3.2	memstart/memsys	4
NavBh-RCK M107I	3.2	memstart/memsys	16
NavBh128-RCK M107I	2.8	memgold	4
NavBh128-RCK M107I	2.8	memgold	16
NavBh128-RCK M107I	2.8	memstart/memsys	4
NavBh128-RCK M107I	2.8	memstart/memsys	16

Table 5: Crystallisation Screening of NavBh-RCK M107I and NavBh128-RCK M107I.
Crystal screening of NavBh-RCK M107I and corresponding pore only construct. Screening was performed immediately after spin column concentration. Samples were observed for a period of 6 months, and no crystals were found in any condition. All trials were performed with the sample in 20mM Tris, pH 8, 200 mM NaCl, 0.25% CYMAL5.

`

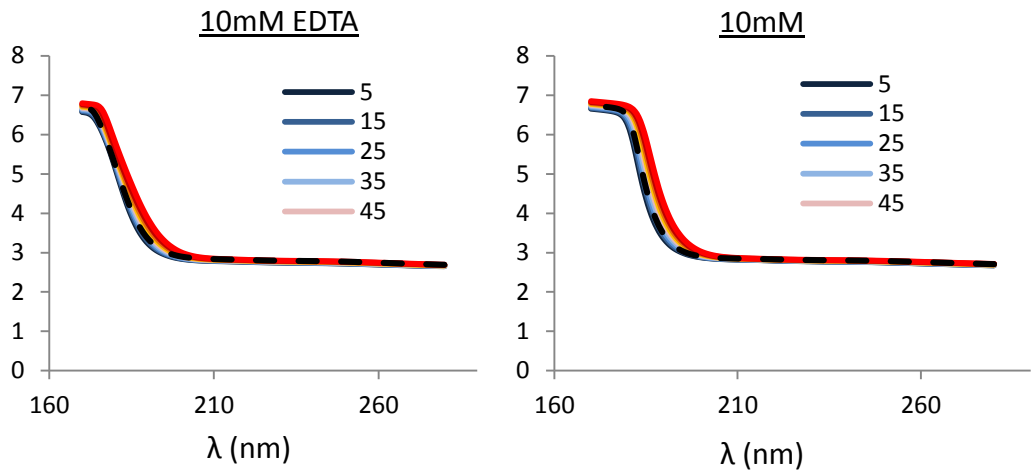

Figure 49: High Tension Measurements of NavBh-RCK M107I Thermal Unfolding experiments.
SRCD High Tension measurements, corresponding to SRCD spectroscopy of NavBh-RCK thermal unfolding experiments in the presence of 10 mM EDTA, or 3 mM $CaCl_2$. (Figure 22)

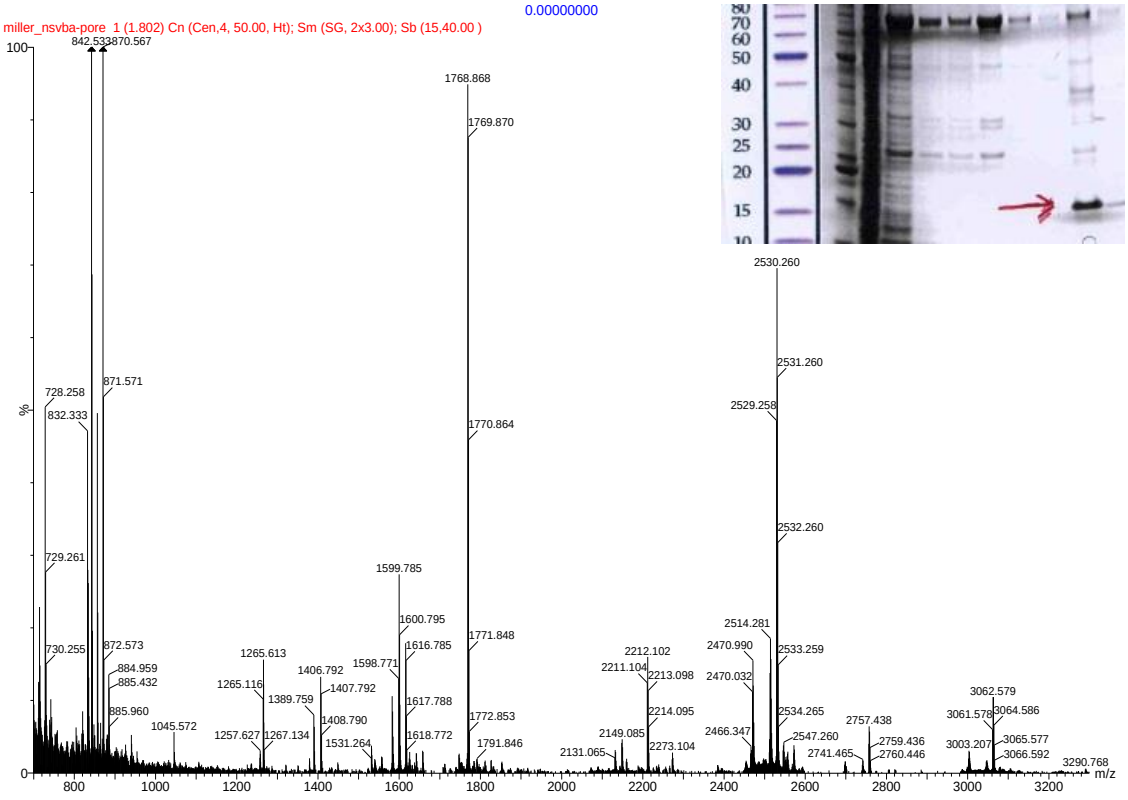

Figure 50: Mass Spectrometry of the NsvBa265 Pore.
Mass spectrometry identification of NsvBa 138-265, performed by Dr Len Packman, at the Cambridge PNAC facility. Analysed band cut from SDS-PAGE is indicated with a red arrow. Results were consistent with NsvBa 138-265.

Construct	1st Detergent	2nd Detergent	Concentration (mg/mL)	Temp (°C)	Mibefradil	screen
NsvBa 138-277	1.5% DDM	0.25% CYMAL5	10.9	4	yes	memgold
NsvBa 138-277	1.5% DDM	0.25% CYMAL5	10.9	4	yes	memstart/sys
NsvBa 138-277	1.5% DDM	0.25% CYMAL5	10	4	no	memgold
NsvBa 138-277	1.5% DDM	0.52% HEGA10	10	4	no	memgold
NsvBa 138-277	1.5% DDM	0.2% DM	10	4	no	memgold
NsvBa 138-265	1.5% DDM	0.52% HEGA10	20	4	no	memgold
NsvBa 138-265	1.5% DDM	0.52% HEGA10	20	4	no	menstart/sys
NsvBa 138-265	1.5% DDM	0.52% HEGA10	20	4	yes	memgold
NsvBa 138-265	1.5% DDM	0.52% HEGA10	20	4	yes	menstart/sys
NsvBa 138-265	1.5% DDM	0.52% HEGA10	20	16	no	memgold
NsvBa 138-265	1.5% DDM	0.52% HEGA10	20	16	no	menstart/sys
NsvBa 138-265	1.5% DDM	0.52% HEGA10	20	16	yes	memgold
NsvBa 138-265	1.5% DDM	0.52% HEGA10	20	16	yes	menstart/sys
NsvBa 138-250	1.5% DDM	0.52% HEGA10	12	16	yes	memgold
NsvBa 138-250	1.5% DDM	0.52% HEGA10	12	16	yes	menstart/sys
NsvBa 138-239	1.5% DDM	0.52% HEGA10	4.6	16	yes	memgold
NsvBa 138-239	1.5% DDM	0.52% HEGA10	4.6	16	yes	menstart/sys
NsvBa 138-250	2% DDM	0.02% DDM	25		no	lcp memgold
NsvBa 138-250	2% DDM	0.02% DDM	25		no	lcp memgold2
NsvBa 138-250	2% DDM	0.02% DDM	25		no	lcp memstart/sys
NsvBa 128-239	2% DDM	0.02% DDM	15		no	lcp memgold
NsvBa 128-239	2% DDM	0.02% DDM	15		no	lcp memgold2
NsvBa 128-239	2% DDM	0.02% DDM	15		no	lcp memstart/sys
NsvBa	2% DDM	0.52%	10	16	no	memgold
NsvBa	2% DDM	0.02% DDM	10	16	no	memgold
NsvBa	2% DDM	0.25% CYMAL 5	10	16	no	memgold
NsvBa	2% DDM	0.02% DDM	10	16	no	memstart/memsys
NsvBa 239	2% DDM	0.02% DDM	8	16	no	memgold
NsvBa 239	2% DDM	0.02% DDM	8	16	no	memstart/memsys
NsvBa 138-265 MS1/MS2	2% DDM	0.02% DDM	20	16	no	memgold
NsvBa 138-265 MS1/MS2	2% DDM	0.02% DDM	20	16	no	memstart/memsys
NsvBa 265 MS1	2% DDM	0.02% DDM	10	16	no	memgold
NsvBa 265 MS1	2% DDM	0.02% DDM	10	16	no	memstart/memsys
NsvBa 138-265	2% DDM	0.02% DDM	5	16	no	memgold
NsvBa 138-265	2% DDM	0.52% HEGA10	5	16	no	memgold
NsvBa 138-265	2% DDM	0.25% CYMAL5	5	16	no	memgold

`

NsvBa 138-265	2% DDM	0.2% DM	5	16	no	memgold
NsvBa 138-265	2% DDM	0.02% LDAO	5	16	no	memgold
NsvBa 138-265	2% DDM	0.02% DDM	5	16	no	memstart/memsys
NsvBa 138-265	2% DDM	0.52% HEGA10	5	16	no	memstart/memsys
NsvBa 138-265	2% DDM	0.25% CYMAL5	5	16	no	memstart/memsys
NsvBa 138-265	2% DDM	0.2% DM	5	16	no	memstart/memsys
NsvBa 138-265	2% DDM	0.02% LDAO	5	16	no	memstart/memsys

Table 6: List of Crystallisation Trials for NsvBa Constructs.
List of crystallisation trials of NsvBa constructs. Trials in red were performed by Dr Claire Bagnéris. All trials were performed with the sitting drop method, unless denoted Lipid Cubic Phase (LCP). First detergent denotes the detergent used to solubilise the membrane. Second detergent was exchanged into during IMAC.

`

References

Abdul-Gader, A., Miles, A.J. & Wallace, B.A., 2011. A reference dataset for the analyses of membrane protein secondary structures and transmembrane residues using circular dichroism spectroscopy. *Bioinformatics*, 27(12), pp.1630–1636.

Adrian, R.H. & Bryant, S.H., 1974. On the repetitive discharge in myotonic muscle fibres. *The Journal of Physiology*, 240(2), pp.505–515.

Agnew, W.S., Miller, J.A., Ellisman, M.H., Rosenberg, R.L., Tomiko, S.A. & Levinson, S.R., 1983. The voltage-regulated sodium channel from the electroplax of Electrophorus electricus. *Cold Spring Harbor Symposia on Quantitative Biology*, 48 Pt 1, pp.165–179.

Agnew, W.S., Moore, A.C., Levinson, S.R. & Raftery, M.A., 1980. Identification of a large molecular weight peptide associated with a tetrodotoxin binding protein from the electroplax of Electrophorus electricus. *Biochemical and Biophysical Research Communications*, 92(3), pp.860–866.

Ahmad, S., Dahllund, L., Eriksson, A.B., Hellgren, D., Karlsson, U., Lund, P.E., Meijer, I.A., Meury, L., Mills, T., Moody, A., Morinville, A., Morten, J., O'Donnell, D., Raynoschek, C., Salter, H., Rouleau, G.A. & Krupp, J.J., 2007. A stop codon mutation in SCN9A causes lack of pain sensation. *Human Molecular Genetics*, 16(17), pp.2114–2121.

Akopian, A.N., Souslova, V., England, S., Okuse, K., Ogata, N., Ure, J., Smith, A., Kerr, B.J., McMahon, S.B., Boyce, S., Hill, R., Stanfa, L.C., Dickenson, A.H. & Wood, J.N., 1999. The tetrodotoxin-resistant sodium channel SNS has a specialized function in pain pathways. *Nature Neuroscience*, 2(6), pp.541–548.

Amaral, C., Carnevale, V., Klein, M.L. & Treptow, W., 2012. Exploring conformational states of the bacterial voltage-gated sodium channel NavAb via molecular dynamics simulations. *Proceedings of the National Academy of Sciences of the United States of America*, 109(52), pp.21336–41.

Amin, A.S., Asghari-Roodsari, A. & Tan, H.L., 2010. Cardiac sodium channelopathies. *Pflugers Archiv European Journal of Physiology*, 460(2), pp.223–237.

Arkin, M.R., Connor, P.R., Garbison, K.E., Heinz, B.A, Wiernicki, T.R. & Johnston, P.A, 1990. FLIPR ™ Assays for GPCR and Ion Channel Targets. *Assay Guidance Manual*.

Arnau, J., Lauritzen, C., Petersen, G.E. & Pedersen, J., 2006. Current strategies for the use of affinity tags and tag removal for the purification of recombinant proteins. *Protein Expression and Purification*, 48(1), pp.1–13.

Artimo, P., Jonnalagedda, M., Arnold, K., Baratin, D., Csardi, G., De Castro, E., Duvaud, S., Flegel, V., Fortier, A., Gasteiger, E., Grosdidier, A., Hernandez, C., Ioannidis, V., Kuznetsov, D., Liechti, R., Moretti, S., Mostaguir, K., Redaschi, N., Rossier, G.,

`

2012. ExPASy: SIB bioinformatics resource portal. *Nucleic Acids Research*, 40(W1), pp.W597–603.

Aslanidis, C. & de Jong, P.J., 1990. Ligation-independent cloning of PCR products (LIC-PCR). *Nucleic Acids Research*, 18(20), pp.6069–6074.

Bagnéris, C., Decaen, P.G., Hall, B.A., Naylor, C.E., Clapham, D.E., Kay, C.W.M. & Wallace, B.A., 2013. Role of the C-terminal domain in the structure and function of tetrameric sodium channels. *Nature Communications*, 4, p.2465.

Bagnéris, C., DeCaen, P.G., Naylor, C.E., Pryde, D.C., Nobeli, I., Clapham, D.E. & Wallace, B.A., 2014. Prokaryotic NavMs channel as a structural and functional model for eukaryotic sodium channel antagonism. *Proceedings of the National Academy of Sciences of the United States of America*, 111(23), pp.8428–33.

Barber, A.F., Carnevale, V., Klein, M.L., Eckenhoff, R.G. & Covarrubias, M., 2014. Modulation of a voltage-gated Na^+ channel by sevoflurane involves multiple sites and distinct mechanisms. *Proceedings of the National Academy of Sciences of the United States of America*, 111(18), pp.6726–6731.

Barber, A.F., Carnevale, V., Raju, S.G., Amaral, C., Treptow, W. & Klein, M.L., 2012. Hinge-bending motions in the pore domain of a bacterial voltage-gated sodium channel. *Biochimica et Biophysica Acta - Biomembranes*, 1818(9), pp.2120–2125.

Baxter, D.F., Kirk, M., Garcia, A.F., Raimondi, A., Holmqvist, M.H., Flint, K.K., Bojanic, D., Distefano, P.S., Curtis, R. & Xie, Y., 2002. A novel membrane potential-sensitive fluorescent dye improves cell-based assays for ion channels. *Journal of Biomolecular Screening*, 7(1), pp.79–85.

Beckh, S., Noda, M., Lübbert, H. & Numa, S., 1989. Differential regulation of three sodium channel messenger RNAs in the rat central nervous system during development. *The EMBO Journal*, 8(12), pp.3611–3616.

Belcher, S.M., Zerillo, C.A., Levenson, R., Ritchie, J.M. & Howe, J.R., 1995. Cloning of a sodium channel alpha subunit from rabbit Schwann cells. *Proceedings of the National Academy of Sciences of the United States of America*, 92(24), pp.11034–11038.

Beneski, D.A., & Catterall, W.A, 1980. Covalent labeling of protein components of the sodium channel with a photoactivable derivative of scorpion toxin. *Proceedings of the National Academy of Sciences of the United States of America*, 77(1), pp.639–643.

Van den Berg, B., Clemons, W.M., Collinson, I., Modis, Y., Hartmann, E., Harrison, S.C. & Rapoport, T.A., 2004. X-ray structure of a protein-conducting channel. *Nature*, 427(6969), pp.36–44.

`

Black, J.A., Dib-Hajj, S., McNabola, K., Jeste, S., Rizzo, M.A., Kocsis, J.D. & Waxman, S.G., 1996. Spinal sensory neurons express multiple sodium channel α-subunit mRNAs. *Molecular Brain Research*, 43(1-2), pp.117–131.

Blanchet, J. & Chahine, M., 2007. Accessibility of four arginine residues on the S4 segment of the Bacillus halodurans sodium channel. *Journal of Membrane Biology*, 215(2-3), pp.169–180.

Boiteux, C., Vorobyov, I. & Allen, T.W., 2014. Ion conduction and conformational flexibility of a bacterial voltage-gated sodium channel. *Proceedings of the National Academy of Sciences of the United States of America*, 111(9), pp.3454–3459.

Bond, P.J. & Sansom, M.S.P., 2007. Bilayer deformation by the Kv channel voltage sensor domain revealed by self-assembly simulations. *Proceedings of the National Academy of Sciences of the United States of America*, 104(8), pp.2631–2636.

Bryksin, A. V. & Matsumura, I., 2010. Overlap extension PCR cloning: A simple and reliable way to create recombinant plasmids. *BioTechniques*, 48(6), pp.463–465.

Burgess, D.L., Kohrman, D.C., Galt, J., Plummer, N.W., Jones, J.M., Spear, B. & Meisler, M.H., 1995. Mutation of a new sodium channel gene, Scn8a, in the mouse mutant "motor endplate disease". *Nature Genetics*, 10(4), pp.461–465.

Caffrey, M., 2015. A comprehensive review of the lipid cubic phase or in meso method for crystallizing membrane and soluble proteins and complexes. *Acta Crystallographica Section F: Structural Biology Communications*, 71(1), pp.3–18.

Caldwell, J.H., Schaller, K.L., Lasher, R.S., Peles, E. & Levinson, S.R., 2000. Sodium channel Na(v)1.6 is localized at nodes of ranvier, dendrites, and synapses. *Proceedings of the National Academy of Sciences of the United States of America*, 97(10), pp.5616–5620.

Cao, Y., Pan, Y., Huang, H., Jin, X., Levin, E.J., Kloss, B. & Zhou, M., 2013. Gating of the TrkH ion channel by its associated RCK protein TrkA. *Nature*, 496(7445), pp.317–22.

Catterall, W.A., Dib-Hajj, S., Meisler, M.H. & Pietrobon, D., 2008. Inherited neuronal ion channelopathies: new windows on complex neurological diseases. *The Journal of Neuroscience*, 28(46), pp.11768–11777.

Catterall, W.A., Kalume, F. & Oakley, J.C., 2010. NaV1.1 channels and epilepsy. *The Journal of Physiology*, 588(Pt 11), pp.1849–1859.

Chahine, M., Pilote, S., Pouliot, V., Takami, H. & Sato, C., 2004. Role of arginine residues on the S4 segment of the Bacillus halodurans Na^+ channel in voltage-sensing. *Journal of Membrane Biology*, 201(1), pp.9–24.

Chakrabarti, N., Ing, C., Payandeh, J., Zheng, N., Catterall, W.A., & Pomès, R., 2013. Catalysis of Na^+ permeation in the bacterial sodium channel Na(V)Ab. *Proceedings*

`

of the National Academy of Sciences of the United States of America, 110(28), pp.11331–11336.

Chakrapani, S. & Perozo, E., 2007. How to gate an ion channel: lessons from MthK. *Nature Structural & Molecular Biology*, 14(3), pp.180–182.

Chakrapani, S., Sompornpisut, P., Intharathep, P., Roux, B. & Perozo, E., 2010. The activated state of a sodium channel voltage sensor in a membrane environment. *Proceedings of the National Academy of Sciences of the United States of America*, 107(12), pp.5435–5440.

Charalambous, K., O'Reilly, A.O., Bullough, P.A. & Wallace, B.A., 2009. Thermal and chemical unfolding and refolding of a eukaryotic sodium channel. *Biochimica et Biophysica Acta - Biomembranes*, 1788(6), pp.1279–1286.

Chen, X., Wang, Q., Ni, F. & Ma, J., 2010. Structure of the full-length Shaker potassium channel Kv1.2 by normal-mode-based X-ray crystallographic refinement. *Proceedings of the National Academy of Sciences of the United States of America*, 107(25), pp.11352–11357.

Chernoff, D.M., 1990. Kinetic analysis of phasic inhibition of neuronal sodium currents by lidocaine and bupivacaine. *Biophysical Journal*, 58(1), pp.53–68.

Cieslak, J.A., (2010). The native structure of the KvAP potassium channel: new applications of pulsed EPR techniques for the study of protein structure in lipid bilayers. Dissertation for the Degree of Doctor of Philosophy in Neuroscience, Northwestern University, Interdepartmental Neuroscience Program.

The Collaborative Computational Project, 1994. The CCP4 suite: Programs for protein crystallography. *Acta Crystallographica Section D: Biological Crystallography*, 50(5), pp.760–763.

Courtney, K.R., Kendig, J.J. & Cohen, E.N., 1978. The rates of interaction of local anesthetics with sodium channels in nerve. *The Journal of Pharmacology and Experimental Therapeutics*, 207(2), pp.594–604.

Cox, J.J., Reimann, F., Nicholas, A.K., Thornton, G., Roberts, E., Springell, K., Karbani, G., Jafri, H., Mannan, J., Raashid, Y., Al-Gazali, L., Hamamy, H., Valente, E.M., Gorman, S., Williams, R., McHale, D.P., Wood, J.N., Gribble, F.M. & Woods, C.G., 2006. An SCN9A channelopathy causes congenital inability to experience pain. *Nature*, 444(7121), pp.894–898.

Cronin, N.B., O'Reilly, A., Duclohier, H. & Wallace, B.A., 2003. Binding of the anticonvulsant drug lamotrigine and the neurotoxin batrachotoxin to voltage-gated sodium channels induces conformational changes associated with block and steady-state activation. *Journal of Biological Chemistry*, 278(12), pp.10675–10682.

Cummins, T.R., Sheets, P.L. & Waxman, S.G., 2007. The roles of sodium channels in nociception: Implications for mechanisms of pain. *Pain*, 131(3), pp.243–257.

`

D'Avanzo, N., McCusker, E.C., Powl, A.M., Miles, A.J., Nichols, C.G. & Wallace, B.A., 2013. Differential lipid dependence of the function of bacterial sodium channels *PLoS ONE*, 8(4), p.e61216.

DeCaen, P.G., Takahashi, Y., Krulwich, T.A., Ito, M. & Clapham, D.E., 2014. Ionic selectivity and thermal adaptations within the voltage-gated sodium channel family of alkaliphilic Bacillus. *ELife*, 3, p.e04387.

DeCaen, P.G., Yarov-Yarovoy, V., Zhao, Y., Scheuer, T. & Catterall, W.A., 2008. Disulfide locking a sodium channel voltage sensor reveals ion pair formation during activation. *Proceedings of the National Academy of Sciences of the United States of America*, 105(39), pp.15142–15147.

DeLano, W.L., 2002. The PyMOL Molecular Graphics System (2002) DeLano Scientific, Palo Alto, CA, USA. http://www.pymol.org.

Dellisanti, C.D., Ghosh, B., Hanson, S.M., Raspanti, J.M., Grant, V.A., Diarra, G.M., Schuh, A.M., Satyshur, K., Klug, C.S. & Czajkowski, C., 2013. Site-directed spin labeling reveals pentameric ligand-gated ion channel gating motions. *PLoS Biology*, 11(11), p.e1001714.

Derebe, M.G., Sauer, D.B., Zeng, W., Alam, A., Shi, N. & Jiang, Y., 2011. Tuning the ion selectivity of tetrameric cation channels by changing the number of ion binding sites. *Proceedings of the National Academy of Sciences of the United States of America*, 108(2), pp.598–602.

Desjardins, P., Hansen, J.B. & Allen, M., 2009. Microvolume protein concentration determination using the NanoDrop 2000c spectrophotometer. *Journal of Visualized Experiments*, (33), pp.1610.

Dong, J., Shi, N., Berke, I., Chen, L. & Jiang, Y., 2005. Structural of the MthK RCK domain and the effect of Ca^{2+} on gating ring stability. *Journal of Biological Chemistry*, 280(50), pp.41716–41724.

Doyle, D.A., Morais Cabral, J., Pfuetzner, R.A., Kuo, A., Gulbis, J.M., Cohen, S.L., Chait, B.T. & MacKinnon, R., 1998. The structure of the potassium channel: molecular basis of K^+ conduction and selectivity. *Science*, 280(5360), pp.69–77.

Drew, D., Lerch, M., Kunji, E., Slotboom, D.J. & de Gier, J.W., 2006. Optimization of membrane protein overexpression and purification using GFP fusions. *Nature Methods*, 3(4), pp.303–313.

Du, Y., Lee, J.E., Nomura, Y., Zhang, T., Zhorov, B.S. & Dong, K., 2009. Identification of a cluster of residues in transmembrane segment 6 of domain III of the cockroach sodium channel essential for the action of pyrethroid insecticides. *The Biochemical Journal*, 419(2), pp.377–385.

England, S. & De Groot, M.J., 2009. Subtype-selective targeting of voltage-gated sodium channels. *British Journal of Pharmacology*, 158(6), pp.1413–1425.

`

Escayg, A., Heils, A., MacDonald, B.T., Haug, K., Sander, T. & Meisler, M.H., 2001. A novel SCN1A mutation associated with generalized epilepsy with febrile seizures plus--and prevalence of variants in patients with epilepsy. *American Journal of Human Genetics*, 68(4), pp.866–873.

Esposito, D. & Chatterjee, D.K., 2006. Enhancement of soluble protein expression through the use of fusion tags. *Current Opinion in Biotechnology*, 17(4), pp.353–358.

Estacion, M., Choi, J.S., Eastman, E.M., Lin, Z., Li, Y., Tyrrell, L., Yang, Y., Dib-Hajj, S.D. & Waxman, S.G., 2010. Can robots patch-clamp as well as humans? Characterization of a novel sodium channel mutation. *The Journal of Physiology*, 588(Pt 11), pp.1915–1927.

Eswar, N., Webb, B., Marti-Renom, M.A., Madhusudhan, M.S., Eramian, D., Shen, M.Y., Pieper, U. & Sali, A., 2006. Comparative protein structure modeling using Modeller. *Current Protocols in Bioinformatics*, Chapter 5, p.Unit 5.6.

Fujinami, S., Terahara, N., Krulwich, T.A. & Ito, M., 2009. Motility and chemotaxis in alkaliphilic Bacillus species. *Future Microbiology*, 4(9), pp.1137–1149.

Furini, S. & Domene, C., 2012. On conduction in a bacterial sodium channel. *PLoS Computational Biology*, 8(4), p.e1002476.

Gamal El-Din, T.M., Scheuer, T. & Catterall, W.A., 2014. Tracking S4 movement by gating pore currents in the bacterial sodium channel NaChBac. *The Journal of General Physiology*, 144(2), pp.147–57.

García, K.D., Sprunger, L.K., Meisler, M.H. & Beam, K.G., 1998. The sodium channel Scn8a is the major contributor to the postnatal developmental increase of sodium current density in spinal motoneurons. *The Journal of Neuroscience*, 18(14), pp.5234–5239.

Gasteiger, E., Gattiker, A., Hoogland, C., Ivanyi, I., Appel, R.D. & Bairoch, A., 2003. ExPASy: The proteomics server for in-depth protein knowledge and analysis. *Nucleic Acids Research*, 31(13), pp.3784–3788.

Gibson, D.G., Young, L., Chuang, R.-Y., Venter, J.C., Hutchison, C.A. & Smith, H.O., 2009. Enzymatic assembly of DNA molecules up to several hundred kilobases. *Nature Methods*, 6(5), pp.343–345.

Glasscock, E., Qian, J., Yoo, J.W. & Noebels, J.L., 2007. Masking epilepsy by combining two epilepsy genes. *Nature Neuroscience*, 10(12), pp.1554–1558.

Glover, C.A.P., Postis, V.L.G., Charalambous, K., Tzokov, S.B., Booth, W.I., Deacon, S.E., Wallace, B.A., Baldwin, S.A. & Bullough, P.A., 2011. AcrB contamination in 2-D crystallization of membrane proteins: Lessons from a sodium channel and a putative monovalent cation/proton antiporter. *Journal of Structural Biology*, 176(3), pp.419–424.

`

Goldberg, Y.P., Macfarlane, J., Macdonald, M.L., Thompson, J., Dube, M.P., Mattice, M., Fraser, R., Young, C., Hossain, S., Pape, T., Payne, B., Radomski, C., Donaldson, G., Ives, E., Cox, J., Younghusband, H.B., Green, R., Duff, A., Boltshauser, E., 2007. Loss-of-function mutations in the Nav1.7 gene underlie congenital indifference to pain in multiple human populations. *Clinical Genetics*, 71(4), pp.311–319.

Goldin, A.L., 2002. Evolution of voltage-gated Na^+ channels. *The Journal of Experimental Biology*, 205(5), pp.575–584.

Gräslund, S., Nordlund, P., Weigelt, J., Hallberg, B.M., Bray, J., Gileadi, O., Knapp, S., Oppermann, U., Arrowsmith, C., Hui, R., Ming, J., dhe-Paganon, S., Park, H., Savchenko, A., Yee, A., Edwards, A., Vincentelli, R., Cambillau, C., Kim, R., 2008. Protein production and purification. *Nature Methods*, 5(2), pp.135–146.

Gu, Y., Gorelik, J., Spohr, H.A., Shevchuk, A., Lab, M.J., Harding, S.E., Vodyanoy, I., Klenerman, D. & Korchev, Y.E., 2002. High-resolution scanning patch-clamp: new insights into cell function. *The FASEB Journal*, 16(7), pp.748–750.

Gustafsson, C., Govindarajan, S. & Minshull, J., 2004. Codon bias and heterologous protein expression. *Trends in Biotechnology*, 22(7), pp.346–353.

Gustafsson, C., Minshull, J., Govindarajan, S., Ness, J., Villalobos, A. & Welch, M., 2012. Engineering genes for predictable protein expression. *Protein Expression and Purification*, 83(1), pp.37–46.

Guy, H.R. & Seetharamulu, P., 1986. Molecular model of the action potential sodium channel. *Proceedings of the National Academy of Sciences of the United States of America*, 83(2), pp.508–512.

Guzman, L.M., Belin, D., Carson, M.J. & Beckwith, J., 1995. Tight regulation, modulation, and high-level expression by vectors containing the arabinose P(BAD) promoter. *Journal of Bacteriology*, 177(14), pp.4121–4130.

Hall, L.T., Hill, C.D., Cole, J.H., Städler, B., Caruso, F., Mulvaney, P., Wrachtrup, J. & Hollenberg, L.C.L., 2010. Monitoring ion-channel function in real time through quantum decoherence. *Proceedings of the National Academy of Sciences of the United States of America*, 107(44), pp.18777–18782.

Hamill, O.P., Marty, A., Neher, E., Sakmann, B. & Sigworth, F.J., 1981. Improved patch-clamp techniques for high-resolution current recording from cells and cell-free membrane patches. *Pflügers Archiv European Journal of Physiology*, 391(2), pp.85–100.

Hanlon, M.R. & Wallace, B.A., 2002. Structure and function of voltage-dependent ion channel regulatory β subunits. *Biochemistry*, 41(9), pp.2886–2894.

Hansma, P.K., Drake, B., Marti, O., Gould, S.A & Prater, C.B., 1989. The scanning ion-conductance microscope. *Science*, 243(4891), pp.641–643.

`

Hartshorne, R.P., Keller, B.U., Talvenheimo, J.A, Catterall, W.A. & Montal, M., 1985. Functional reconstitution of the purified brain sodium channel in planar lipid bilayers. *Proceedings of the National Academy of Sciences of the United States of America*, 82(1), pp.240–244.

Heinemann, S.H., Terlau, H., Stühmer, W., Imoto, K. & Numa, S., 1992. Calcium channel characteristics conferred on the sodium channel by single mutations. *Nature*, 356(6368), pp.441–443.

Hodgkin, A.L. & Huxley, A.F., 1952. A quantitative description of membrane current and its application to conduction and excitation in nerve. *Bulletin of Mathematical Biology*, 52(1-2), pp.25–71.

Holland, K.D., Kearney, J.A., Glauser, T.A., Buck, G., Keddache, M., Blankston, J.R., Glaaser, I.W., Kass, R.S. & Meisler, M.H., 2008. Mutation of sodium channel SCN3A in a patient with cryptogenic pediatric partial epilepsy. *Neuroscience Letters*, 433(1), pp.65–70.

Huang, C.J., Harootunian, A., Maher, M.P., Quan, C., Raj, C.D., McCormack, K., Numann, R., Negulescu, P.A. & González, J.E., 2006. Characterization of voltage-gated sodium-channel blockers by electrical stimulation and fluorescence detection of membrane potential. *Nature Biotechnology*, 24(4), pp.439–446.

Irie, K., Shimomura, T. & Fujiyoshi, Y., 2012. The C-terminal helical bundle of the tetrameric prokaryotic sodium channel accelerates the inactivation rate. *Nature Communications*, 3, p.793.

Ito, M., Xu, H., Guffanti, A.A., Wei, Y., Zvi, L., Clapham, D.E. & Krulwich, T.A., 2004. The voltage-gated Na^+ channel NaVBP has a role in motility, chemotaxis, and pH homeostasis of an alkaliphilic Bacillus. *Proceedings of the National Academy of Sciences of the United States of America*, 101(29), pp.10566–10571.

Jeschke, G., Chechik, V., Ionita, P., Godt, A., Zimmermann, H., Banham, J., Timmel, C.R., Hilger, D. & Jung, H., 2006. DeerAnalysis2006 - a comprehensive software package for analyzing pulsed ELDOR data. *Applied Magnetic Resonance*, 30(3-4), pp.473–498.

Jiang, Y., Lee, A., Chen, J., Cadene, M., Chait, B.T. & MacKinnon, R., 2002. Crystal structure and mechanism of a calcium-gated potassium channel. *Nature*, 417(6888), pp.515–522.

Jiang, Y., Lee, A., Chen, J., Ruta, V., Cadene, M., Chait, B.T. & MacKinnon, R., 2003. X-ray structure of a voltage-dependent K^+ channel. *Nature*, 423(6935), pp.33–41.

Kalsi, S., Morgan, H. & de Planque, M.R.R., 2013. Suspended Bilayers in Shaped Apertures Enable 24-Hour Ion Channel Recordings. *Biophysical Journal*, 104(2), p.519a.

`

Kalsi, S., Powl, A., Wallace, B.A., Morgan, H. & De Planque, M.R.R., 2014. Shaped apertures in photoresist films enhance the lifetime and mechanical stability of suspended lipid bilayers. *Biophysical Journal*, 106(8), pp.1650–1659.

Ke, S., Zangerl, E.M. & Stary-Weinzinger, A., 2013. Distinct interactions of Na^+ and Ca^{2+} ions with the selectivity filter of the bacterial sodium channel NaVAb. *Biochemical and Biophysical Research Communications*, 430(4), pp.1272–1276.

Kearney, J.A., Plummer, N.W., Smith, M.R., Kapur, J., Cummins, T.R., Waxman, S.G., Goldin, A.L. & Meisler, M.H., 2001. A gain-of-function mutation in the sodium channel gene Scn2a results in seizures and behavioral abnormalities. *Neuroscience*, 102(2), pp.307–317.

Kearney, J.A., Yang, Y., Beyer, B., Bergren, S.K., Claes, L., DeJonghe, P. & Frankel, W.N., 2006. Severe epilepsy resulting from genetic interaction between Scn2a and Kcnq2. *Human Molecular Genetics*, 15(6), pp.1043–1048.

Kellenberger, S., West, J.W., Catterall, W.A., & Scheuer, T., 1997. Molecular analysis of potential hinge residues in the inactivation gate of brain type IIA Na^+ channels. *The Journal of General Physiology*, 109(5), pp.607–617.

Kelley, L.A. & Sternberg, M.J.E., 2009. Protein structure prediction on the web: a case study using the Phyre server. *Nature Protocols*, 4(3), pp.363–371.

King, P.H., Corsi, J.C., Pan, B.H., Morgan, H., de Planque, M.R.R. & Zauner, K.P., 2012. Towards molecular computing: Co-development of microfluidic devices and chemical reaction media. *BioSystems*, 109(1), pp.18–23.

Klugbauer, N., Lacinova, L., Flockerzi, V. & Hofmann, F., 1995. Structure and functional expression of a new member of the tetrodotoxin-sensitive voltage-activated sodium channel family from human neuroendocrine cells. *The EMBO journal*, 14(6), pp.1084–1090.

Koishi, R., Xu, H., Ren, D., Navarro, B., Spiller, B.W., Shi, Q. & Clapham, D.E., 2004. A superfamily of voltage-gated sodium channels in bacteria. *Journal of Biological Chemistry*, 279(10), pp.9532–9538.

Kong, C., Zeng, W., Ye, S., Chen, L., Sauer, D.B., Lam, Y., Derebe, M.G. & Jiang, Y., 2012. Distinct gating mechanisms revealed by the structures of a multi-ligand gated K^+ channel. *ELife*, 2012(1), p.e00184.

Korchev, Y.E., Negulyaev, Y.A., Edwards, C.R., Vodyanoy, I. & Lab, M.J., 2000. Functional localization of single active ion channels on the surface of a living cell. *Nature Cell Biology*, 2(9), pp.616–619.

Kuo, M.M.C., Baker, K.A., Wong, L. & Choe, S., 2007. Dynamic oligomeric conversions of the cytoplasmic RCK domains mediate MthK potassium channel activity. *Proceedings of the National Academy of Sciences of the United States of America*, 104(7), pp.2151–2156.

`

Kuzmenkin, A., Bezanilla, F. & Correa, A.M., 2004. Gating of the bacterial sodium channel, NaChBac: voltage-dependent charge movement and gating currents. *The Journal of General Physiology*, 124(4), pp.349–356.

Lee, S.Y., Lee, A., Chen, J. & MacKinnon, R., 2005. Structure of the KvAP voltage-dependent K^+ channel and its dependence on the lipid membrane. *Proceedings of the National Academy of Sciences of the United States of America*, 102(43), pp.15441–15446.

Lees, J.G., Smith, B.R., Wien, F., Miles, A.J. & Wallace, B.A., 2004. CDtool - An integrated software package for circular dichroism spectroscopic data processing, analysis, and archiving. *Analytical Biochemistry*, 332(2), pp.285–289.

Lehmann-Horn, F., Rüdel, R., Ricker, K., Lorković, H., Dengler, R. & Hopf, H.C., 1983. Two cases of adynamia episodica hereditaria: in vitro investigation of muscle cell membrane and contraction parameters. *Muscle & Nerve*, 6(2), pp.113–121.

Li, Y., Berke, I., Chen, L. & Jiang, Y., 2007. Gating and inward rectifying properties of the MthK K^+ channel with and without the gating ring. *The Journal of General Physiology*, 129(2), pp.109–120.

Lithwick, G. & Margalit, H., 2003. Hierarchy of sequence-dependent features associated with prokaryotic translation. *Genome Research*, 13(12), pp.2665–2673.

Logothetis, D.E., Movahedi, S., Satler, C., Lindpaintner, K. & Nadal-Ginard, B., 1992. Incremental reductions of positive charge within the S4 region of a voltage-gated K^+ channel result in corresponding decreases in gating charge. *Neuron*, 8(3), pp.531–540.

Long, S.B., Campbell, E.B. & Mackinnon, R., 2005. Crystal structure of a mammalian voltage-dependent Shaker family K^+ channel. *Science*, 309(5736), pp.897–903.

Long, S.B., Tao, X., Campbell, E.B. & MacKinnon, R., 2007. Atomic structure of a voltage-dependent K^+ channel in a lipid membrane-like environment. *Nature*, 450(7168), pp.376–382.

Ma, D., Cook, D.N., Alberti, M., Pon, N.G., Nikaido, H. & Hearst, J.E., 1995. Genes acrA and acrB encode a stress-induced efflux system of Escherichia coli. *Molecular Microbiology*, 16(1), pp.45–55.

Martin, M.S., Tang, B., Papale, L.A., Yu, F.H., Catterall, W.A. & Escayg, A., 2007. The voltage-gated sodium channel Scn8a is a genetic modifier of severe myoclonic epilepsy of infancy. *Human Molecular Genetics*, 16(23), pp.2892–2899.

McCusker, E.C., Bagnéris, C., Naylor, C.E., Cole, A.R., D'Avanzo, N., Nichols, C.G. & Wallace, B.A., 2012. Structure of a bacterial voltage-gated sodium channel pore reveals mechanisms of opening and closing. *Nature Communications*, 3, p.1102.

`

McCusker, E.C., Avanzo, N., Nichols, C.G. & Wallace, B.A., 2011. Simplified bacterial "pore" channel provides insight into the assembly, stability, and structure of sodium channels. *Journal of Biological Chemistry*, 286(18), pp.16386–16391.

McGuffin, L.J., Bryson, K. & Jones, D.T., 2000. The PSIPRED protein structure prediction server. *Bioinformatics*, 16(4), pp.404–405.

McHaourab, H.S., Steed, P.R. & Kazmier, K., 2011. Toward the fourth dimension of membrane protein structure: Insight into dynamics from spin-labeling EPR spectroscopy. *Structure*, 19(11), pp.1549–1561.

McKinney, B.C., Chow, C.Y., Meisler, M.H. & Murphy, G.G., 2008. Exaggerated emotional behavior in mice heterozygous null for the sodium channel Scn8a (Nav1.6). *Genes, Brain and Behavior*, 7(6), pp.629–638.

Meisler, M.H. & Kearney, J.A., 2005. Sodium channel mutations in epilepsy and other neurological disorders. *Journal of Clinical Investigation*, 115(8), pp.2010–2017.

Mendes, G.P., de Planque, M.R., Grage, S.L., Berry, R. & Watts, A., 2005. Incorporation of the mechanosensitive channel (MscL) and the amyloid Abeta 1-40 peptide by vesicle fusion into planar lipid bilayers. The *FEBS Journal*, 272, pp.342–342

Miercke, L.J., Stroud, R.M. & Dratz, E.A., 1989. Preparative purification of functional bacteriorhodopsin by high-performance size-exclusion chromatography. *Journal of Chromatography*, 483, pp.331–340.

Miles, A.J., Wien, F., Lees, J.G., Rodger, A. & Wallace, B.A., 2003. Calibration and standardisation of synchrotron radiation circular dichroism and conventional circular dichroism spectrophotometers. *Spectroscopy,* 17, 653-661.

Mio, K., Mio, M., Arisaka, F., Sato, M. & Sato, C., 2010. The C-terminal coiled-coil of the bacterial voltage-gated sodium channel NaChBac is not essential for tetramer formation, but stabilizes subunit-to-subunit interactions. *Progress in Biophysics and Molecular Biology*, 103(1), pp.111–121.

Misra, S.N., Kahlig, K.M. & George, A.L., 2008. Impaired NaV1.2 function and reduced cell surface expression in benign familial neonatal-infantile seizures. *Epilepsia*, 49(9), pp.1535–1545.

Molecular Devices, 2006. *pClamp10, data acquisition and analysis for comprehensive electrophysiology*, Molecular Devices.

Montal, M. & Mueller, P., 1972. Formation of bimolecular membranes from lipid monolayers and a study of their electrical properties. *Proceedings of the National Academy of Sciences of the United States of America*, 69(12), pp.3561–3566.

Morrow, E.M., Yoo, S.-Y., Flavell, S.W., Kim, T.-K., Lin, Y., Hill, R.S., Mukaddes, N.M., Balkhy, S., Gascon, G., Hashmi, A., Al-Saad, S., Ware, J., Joseph, R.M., Greenblatt, R., Gleason, D., Ertelt, J.A, Apse, K.A., Bodell, A., Partlow, J.N., 2008. Identifying

`

autism loci and genes by tracing recent shared ancestry. *Science*, 321(5886), pp.218–223.

Nassar, M.A., Stirling, L.C., Forlani, G., Baker, M.D., Matthews, E.A., Dickenson, A.H. & Wood, J.N., 2004. Nociceptor-specific gene deletion reveals a major role for Nav1.7 (PN1) in acute and inflammatory pain. *Proceedings of the National Academy of Sciences of the United States of America*, 101(34), pp.12706–12711.

Neher, E. & Sakmann, B., 1976. Single-channel currents recorded from membrane of denervated frog muscle fibres. *Nature*, 260(5554), pp.799–802.

Neophytou, I., Harvey, R., Lawrence, J., Marsh, P., Panaretou, B. & Barlow, D., 2007. Eukaryotic integral membrane protein expression utilizing the Escherichia coli glycerol-conducting channel protein (GlpF). *Applied Microbiology and Biotechnology*, 77(2), pp.375–381.

Newby, Z.E.R., O'Connell, J.D., Gruswitz, F., Hays, F.A., Harries, W.E.C., Harwood, I.M., Ho, J.D., Lee, J.K., Savage, D.F., Miercke, L.J.W. & Stroud, R.M., 2009. A general protocol for the crystallization of membrane proteins for X-ray structural investigation. *Nature Protocols*, 4(5), pp.619–637.

Niu, X., Qian, X. & Magleby, K.L., 2004. Linker-gating ring complex as passive spring and Ca^{2+} dependent machine for a voltage- and Ca^{2+}-activated potassium channel. *Neuron*, 42(5), pp.745–756.

Noda, M., Ikeda, T., Suzuki, H., Takeshima, H., Takahashi, T., Kuno, M. & Numa, S., 1986. Expression of functional sodium channels from cloned cDNA. *Nature*, 322(6082), pp.826–828.

Novagen, 2014. pET System Manual. *Novagen.*

Nurani, G., Radford, M., Charalambous, K., O'Reilly, A.O., Cronin, N.B., Haque, S. & Wallace, B.A., 2008. Tetrameric bacterial sodium channels: Characterization of structure, stability, and drug binding. *Biochemistry*, 47(31), pp.8114–8121.

O'Reilly, A.O., Charalambous, K., Nurani, G., Powl, A.M. & Wallace, B.A., 2008. G219S mutagenesis as a means of stabilizing conformational flexibility in the bacterial sodium channel NaChBac. *Molecular Membrane Biology*, 25(8), pp.670–676.

O'Reilly, A.O., Khambay, B.P.S., Williamson, M.S., Field, L.M., WAllace, B.A. & Davies, T.G.E., 2006. Modelling insecticide-binding sites in the voltage-gated sodium channel. *The Biochemical Journal*, 396(2), pp.255–263.

O'Reilly, A.O., Powl, A.M. & Wallace, B.A., 2011. An Alternative Tetramerisation Domain Restores Expression of the NaChBac voltage-gated sodium channel. *Biophysical Journal*, 100(3), p.422a–423a.

O'Reilly, A.O., Williamson, M.S., González-Cabrera, J., Turberg, A., Field, L.M., Wallace, B.A. & Davies, T.G.E., 2014. Predictive 3D modelling of the interactions of

`

pyrethroids with the voltage-gated sodium channels of ticks and mites. *Pest Management Science*, 70(3), pp.369–377.

Ouyang, W., Jih, T.-Y., Zhang, T.-T., Correa, A.M. & Hemmings, H.C., 2007. Isoflurane inhibits NaChBac, a prokaryotic voltage-gated sodium channel. *The Journal of Pharmacology and Experimental Therapeutics*, 322(3), pp.1076–1083.

Paldi, T. & Gurevitz, M., 2010. Coupling between residues on S4 and S1 defines the voltage-sensor resting conformation in NaChBac. *Biophysical Journal*, 99(2), pp.456–463.

Pannier, M., Veit, S., Godt, A., Jeschke, G. & Spiess, H., 2000. Dead-time free measurement of dipole–dipole interactions between electron spins. *Journal of Magnetic Resonance*, 142(2), pp.331–340.

Papale, L.A., Beyer, B., Jones, J.M., Sharkey, L.M., Tufik, S., Epstein, M., Letts, V.A., Meisler, M.H., Frankel, W.N. & Escayg, A., 2009. Heterozygous mutations of the voltage-gated sodium channel SCN8A are associated with spike-wave discharges and absence epilepsy in mice. *Human Molecular Genetics*, 18(9), pp.1633–1641.

Pau, V.P.T., Smith, F.J., Taylor, A.B., Parfenova, L. V., Samakai, E., Callaghan, M.M., Abarca-Heidemann, K., Hart, P.J. & Rothberg, B.S., 2011. Structure and function of multiple Ca^{2+} binding sites in a K^+ channel regulator of K^+ conductance (RCK) domain. *Proceedings of the National Academy of Sciences of the United States of America*, 108(43), pp.17684–17689.

Pavlov, E., Bladen, C., Winkfein, R., Diao, C., Dhaliwal, P. & French, R.J., 2005. The pore, not cytoplasmic domains, underlies inactivation in a prokaryotic sodium channel. *Biophysical journal*, 89(1), pp.232–242.

Payandeh, J., Gamal El-Din, T.M., Scheuer, T., Zheng, N. & Catterall, W.A., 2012. Crystal structure of a voltage-gated sodium channel in two potentially inactivated states. *Nature*, 486(7401), pp.135–9.

Payandeh, J., Scheuer, T., Zheng, N. & Catterall, W.A., 2011. The crystal structure of a voltage-gated sodium channel. *Nature*, 475(7356), pp.353–358.

Perozo, E., Cuello, L.G., Cortes, D.M., Liu, Y.S. & Sompornpisut, P., 2002. EPR approaches to ion channel structure and function. *Novartis Foundation Symposium*, 245, pp.146–158; discussion 158–164, 165–168.

De Planque, M.R.R., de Planque, M.R.R., Mendes, G.P., Zagnoni, M., Sandison, M.E., Fisher, K.H., Berry, R.M., Watts, A. & Morgan, H., 2006. Controlled delivery of membrane proteins to artificial lipid bilayers by nystatin-ergosterol modulated vesicle fusion. *Nanobiotechnology*, 153(2), pp.21–30.

Platt, D. & Griggs, R., 2009. Skeletal muscle channelopathies: new insights into the periodic paralyses and nondystrophic myotonias. *Current Opinion in Neurology*, 22(5), pp.524–531.

`

Powl, A.M., Miles, A.J. & Wallace, B.A., 2012. Transmembrane and extramembrane contributions to membrane protein thermal stability: Studies with the NaChBac sodium channel. *Biochimica et Biophysica Acta - Biomembranes*, 1818(3), pp.889–895.

Powl, A.M., O'Reilly, A.O., Miles, A.J. & Wallace, B.A., 2010. Synchrotron radiation circular dichroism spectroscopy-defined structure of the C-terminal domain of NaChBac and its role in channel assembly. *Proceedings of the National Academy of Sciences of the United States of America*, 107(32), pp.14064–14069.

Provencher, S.W. & Glöckner, J., 1981. Estimation of globular protein secondary structure from circular dichroism. *Biochemistry*, 20(1), pp.33–37.

Qu, Y., Rogers, J., Tanada, T., Scheuer, T. & Catterall, W.A., 1995. Molecular determinants of drug access to the receptor site for antiarrhythmic drugs in the cardiac Na^+ channel. *Proceedings of the National Academy of Sciences of the United States of America*, 92(25), pp.11839–11843.

Raghuraman, H., Islam, S.M., Mukherjee, S., Roux, B. & Perozo, E., 2014. Dynamics transitions at the outer vestibule of the KcsA potassium channel during gating. *Proceedings of the National Academy of Sciences of the United States of America*, 111(5), pp.1831–1836.

Ragsdale, D.S., McPhee, J.C., Scheuer, T. & Catterall, W.A., 1994. Molecular determinants of state-dependent block of Na^+ channels by local anesthetics. *Science*, 265(5179), pp.1724–1728.

Reimhult, E. & Kumar, K., 2008. Membrane biosensor platforms using nano- and microporous supports. *Trends in Biotechnology*, 26(2), pp.82–89.

Ren, D., Navarro, B., Xu, H., Yue, L., Shi, Q. & Clapham, D.E., 2001. A prokaryotic voltage-gated sodium channel. *Science*, 294(5550), pp.2372–2375.

Richardson, S.M., Nunley, P.W., Yarrington, R.M., Boeke, J.D. & Bader, J.S., 2010. GeneDesign 3.0 is an updated synthetic biology toolkit. *Nucleic Acids Research*, 38(8), pp.2603–2606.

Rogart, R.B., Cribbs, L.L., Muglia, L.K., Kephart, D.D. & Kaiser, M.W., 1989. Molecular cloning of a putative tetrodotoxin-resistant rat heart Na^+ channel isoform. *Proceedings of the National Academy of Sciences of the United States of America*, 86(20), pp.8170–8174.

Rohl, C.A., Strauss, C.E.M., Misura, K.M.S. & Baker, D., 2004. Protein structure prediction using rosetta. *Methods in Enzymology*, 383, pp.66–93.

Rosenberg, R.L., Tomiko, S. a & Agnew, W.S., 1984. Reconstitution of neurotoxin-modulated ion transport by the voltage-regulated sodium channel isolated from the electroplax of Electrophorus electricus. *Proceedings of the National Academy of Sciences of the United States of America*, 81(4), pp.1239–1243.

`

Sahdev, S., Khattar, S.K. & Saini, K.S., 2008. Production of active eukaryotic proteins through bacterial expression systems: A review of the existing biotechnology strategies. *Molecular and Cellular Biochemistry*, 307(1-2), pp.249–264.

Sahu, I.D., McCarrick, R.M., Troxel, K.R., Zhang, R., Smith, H.J., Dunagan, M.M., Swartz, M.S., Rajan, P. V., Kroncke, B.M., Sanders, C.R. & Lorigan, G.A., 2013. DEER EPR measurements for membrane protein structures via bifunctional spin labels and lipodisq nanoparticles. *Biochemistry*, 52(38), pp.6627–6632.

Sasaki, M., Takagi, M. & Okamura, Y., 2006. A voltage sensor-domain protein is a voltage-gated proton channel. *Science*, 312(5773), pp.589–592.

Sato, C., Ueno, Y., Asai, K., Takahashi, K., Sato, M., Engel, A. & Fujiyoshi, Y., 2001. The voltage-sensitive sodium channel is a bell-shaped molecule with several cavities. *Nature*, 409(6823), pp.1047–1051.

Scheuer, T., 2011. Regulation of sodium channel activity by phosphorylation. *Seminars in Cell and Developmental Biology*, 22(2), pp.160–165.

Schiemann, O. & Prisner, T.F., 2007. Long-range distance determinations in biomacromolecules by EPR spectroscopy. *Quarterly Reviews of Biophysics*, 40(1), pp.1–53.

Schmidt, D., Jiang, Q.-X. & MacKinnon, R., 2006. Phospholipids and the origin of cationic gating charges in voltage sensors. *Nature*, 444(7120), pp.775–779.

Schroeter, A., Walzik, S., Blechschmidt, S., Haufe, V., Benndorf, K. & Zimmer, T., 2010. Structure and function of splice variants of the cardiac voltage-gated sodium channel Nav1.5. *Journal of Molecular and Cellular Cardiology*, 49(1), pp.16–24.

Schwede, T., Kopp, J., Guex, N. & Peitsch, M.C., 2003. SWISS-MODEL: An automated protein homology-modeling server. *Nucleic Acids Research*, 31(13), pp.3381–3385.

Seddon, A.M., Curnow, P. & Booth, P.J., 2004. Membrane proteins, lipids and detergents - not just a soap opera: Lipid-protein interactions. *Biochimica et Biophysica Acta*, 1666(1-2), pp.105–117.

Shafer, T.J., Meyer, D.A. & Crofton, K.M., 2005. Developmental neurotoxicity of pyrethroid insecticides: Critical review and future research needs. *Environmental Health Perspectives*, 113(2), pp.123–136.

Shafrir, Y., Durell, S.R. & Guy, H.R., 2008a. Models of the structure and gating mechanisms of the pore domain of the NaChBac ion channel. *Biophysical Journal*, 95(8), pp.3650–3662.

Shafrir, Y., Durell, S.R. & Guy, H.R., 2008b. Models of voltage-dependent conformational changes in NaChBac channels. *Biophysical Journal*, 95(8), pp.3663–3676.

`

Shafrir, Y., Durell, S.R. & Guy, H.R., 2009. Structural models of NaChBac: Does the secondary structure of S4 change during gating? *Biophysical Journal*, 96(3), p.484a.

Shaya, D., Findeisen, F., Abderemane-Ali, F., Arrigoni, C., Wong, S., Nurva, S.R., Loussouarn, G. & Minor, D.L., 2014. Structure of a prokaryotic sodium channel pore reveals essential gating elements and an outer ion binding site common to eukaryotic channels. *Journal of Molecular Biology*, 426(2), pp.467–483.

Shrivastava, I.H., Durell, S.R. & Guy, H.R., 2004. A model of voltage gating developed using the KvAP channel crystal structure. *Biophysical Journal*, 87(4), pp.2255–2270.

Sievers, F., Wilm, A., Dineen, D., Gibson, T.J., Karplus, K., Li, W., Lopez, R., McWilliam, H., Remmert, M., Söding, J., Thompson, J.D. & Higgins, D.G., 2011. Fast, scalable generation of high-quality protein multiple sequence alignments using Clustal Omega. *Molecular Systems Biology*, 7(1), p.539.

Smith, F.J., Pau, V.P.T., Cingolani, G. & Rothberg, B.S., 2012. Crystal structure of a Ba^{2+}-bound gating ring reveals elementary steps in RCK domain activation. *Structure*, 20(12), pp.2038–2047.

Smith, F.J., Pau, V.P.T., Cingolani, G. & Rothberg, B.S., 2013. Structural basis of allosteric interactions among Ca^{2+}-binding sites in a K^+ channel RCK domain. *Nature Communications*, 4, p.2621.

Sokolov, S., Scheuer, T. & Catterall, W.A., 2008. Depolarization-activated gating pore current conducted by mutant sodium channels in potassium-sensitive normokalemic periodic paralysis. *Proceedings of the National Academy of Sciences of the United States of America*, 105(50), pp.19980–19985.

Sokolov, S., Scheuer, T. & Catterall, W.A., 2007. Gating pore current in an inherited ion channelopathy. *Nature*, 446(7131), pp.76–78.

Stamm, M., Staritzbichler, R., Khafizov, K. & Forrest, L.R., 2013. Alignment of helical membrane protein sequences using AlignMe. *PLoS ONE*, 8(3), p.e57731.

Starace, D.M. & Bezanilla, F., 2004. A proton pore in a potassium channel voltage sensor reveals a focused electric field. *Nature*, 427(6974), pp.548–553.

Steinhoff, H.J., Mollaaghababa, R., Altenbach, C., Hideg, K., Krebs, M., Khorana, H.G. & Hubbell, W.L., 1994. Time-resolved detection of structural changes during the photocycle of spin-labeled bacteriorhodopsin. *Science*, 266(5182), pp.105–107.

Van Stokkum, I.H., Spoelder, H.J., Bloemendal, M., van Grondelle, R. & Groen, F.C., 1990. Estimation of protein secondary structure and error analysis from circular dichroism spectra. *Analytical Biochemistry*, 191(1), pp.110–118.

`

Struyk, A.F. & Cannon, S.C., 2007. A Na^+ channel mutation linked to hypokalemic periodic paralysis exposes a proton-selective gating pore. *The Journal of General Physiology*, 130(1), pp.11–20.

Struyk, A.F. & Cannon, S.C., 2008. Paradoxical depolarization of Ba^{2+}-treated muscle exposed to low extracellular K^+: Insights into resting potential abnormalities in hypokalemic paralysis. *Muscle and Nerve*, 37(3), pp.326–337.

Studer, A., Demarche, S., Langenegger, D. & Tiefenauer, L., 2011. Integration and recording of a reconstituted voltage-gated sodium channel in planar lipid bilayers. *Biosensors and Bioelectronics*, 26(5), pp.1924–1928.

Studer, A., Han, X., Winkler, F.K. & Tiefenauer, L.X., 2009. Formation of individual protein channels in lipid bilayers suspended in nanopores. *Colloids and Surfaces B: Biointerfaces*, 73(2), pp.325–331.

Takeshita, K., Sakata, S., Yamashita, E., Fujiwara, Y., Kawanabe, A., Kurokawa, T., Okochi, Y., Matsuda, M., Narita, H., Okamura, Y. & Nakagawa, A., 2014. X-ray crystal structure of voltage-gated proton channel. *Nature Structural & Molecular Biology*, 21(4), pp.352–7.

Tamkun, M.M., Talvenheimo, J. a. & Catterall, W.A., 1984. The sodium channel from rat brain. Reconstitution of neurotoxin-activated ion flux and scorpion toxin binding from purified components. *Journal of Biological Chemistry*, 259(3), pp.1676–1688.

Tang, L., Gamal El-Din, T.M., Payandeh, J., Martinez, G.Q., Heard, T.M., Scheuer, T., Zheng, N. & Catterall, W.A., 2014. Structural basis for Ca^{2+} selectivity of a voltage-gated calcium channel. *Nature*, 505(7481), pp.56–61.

Terlau, H., Heinemann, S.H., Stühmer, W., Pusch, M., Conti, F., Imoto, K. & Numa, S., 1991. Mapping the site of block by tetrodotoxin and saxitoxin of sodium channel II. *FEBS letters*, 293(1-2), pp.93–96.

Tiefenauer, L.X. & Studer, A., 2008. Nano for bio: nanopore arrays for stable and functional lipid bilayer membranes (Mini Review). *Biointerphases*, 3(2), p.FA74.

Trimmer, J.S., Cooperman, S.S., Tomiko, S.A., Zhou, J.Y., Crean, S.M., Boyle, M.B., Kallen, R.G., Sheng, Z.H., Barchi, R.L. & Sigworth, F.J., 1989. Primary structure and functional expression of a mammalian skeletal muscle sodium channel. *Neuron*, 3(1), pp.33–49.

Trudeau, M.M., Dalton, J.C., Day, J.W., Ranum, L.P.W. & Meisler, M.H., 2006. Heterozygosity for a protein truncation mutation of sodium channel SCN8A in a patient with cerebellar atrophy, ataxia, and mental retardation. *Journal of Medical Genetics*, 43(6), pp.527–530.

Tsai, C.J., Tani, K., Irie, K., Hiroaki, Y., Shimomura, T., McMillan, D.G., Cook, G.M., Schertler, G.F.X., Fujiyoshi, Y. & Li, X.D., 2013. Two alternative conformations of a

`

voltage-gated sodium channel. *Journal of Molecular Biology*, 425(22), pp.4074–4088.

Tuller, T., Waldman, Y.Y., Kupiec, M. & Ruppin, E., 2010. Translation efficiency is determined by both codon bias and folding energy. *Proceedings of the National Academy of Sciences of the United States of America*, 107(8), pp.3645–3650.

Ulmschneider, M.B., Bagnéris, C., McCusker, E.C., DeCaen, P.G., Delling, M., Clapham, D.E., Ulmschneider, J.P. & Wallace, B.A., 2013. Molecular dynamics of ion transport through the open conformation of a bacterial voltage-gated sodium channel. *Proceedings of the National Academy of Sciences of the United States of America*, 110(16), pp.6364–9.

Usherwood, P.N.R., Davies, T.G.E., Mellor, I.R., O'Reilly, A.O., Peng, F., Vais, H., Khambay, B.P.S., Field, L.M. & Williamson, M.S., 2007. Mutations in DIIS5 and the DIIS4-S5 linker of Drosophila melanogaster sodium channel define binding domains for pyrethroids and DDT. *FEBS Letters*, 581(28), pp.5485–5492.

Uysal, S., Vásquez, V., Tereshko, V., Esaki, K., Fellouse, F.A., Sidhu, S.S., Koide, S., Perozo, E. & Kossiakoff, A., 2009. Crystal structure of full-length KcsA in its closed conformation. *Proceedings of the National Academy of Sciences of the United States of America*, 106(16), pp.6644–6649.

Vieira-Pires, R.S., Szollosi, A. & Morais-Cabral, J.H., 2013. The structure of the KtrAB potassium transporter. *Nature*, 496(7445), pp.323–328.

Villalobos, A., Ness, J.E., Gustafsson, C., Minshull, J. & Govindarajan, S., 2006. Gene Designer: a synthetic biology tool for constructing artificial DNA segments. *BMC Bioinformatics*, 7(1), p.285.

Wallace, B.A., 2009. Protein characterisation by synchrotron radiation circular dichroism spectroscopy. *Quarterly Reviews of Biophysics*, 42(4), pp.317–370.

Wallace, B.A., & Janes, R.W. (eds), 2003. Circular dichroism and synchrotron radiation circular dichroism spectroscopy: tools for drug discovery. *Biochemical Society transactions*, 31(3), pp.631–633.

Wallace, B.A. & Janes, R.W., 2009. *Modern techniques for circular dichroism and synchrotron radiation circular dichroism spectroscopy: 1*, IOS Press.

Wang, Q., Shen, J., Li, Z., Timothy, K., Vincent, G.M., Priori, S.G., Schwartz, P.J. & Keating, M.T., 1995. Cardiac sodium channel mutations in patients with long QT syndrome, an inherited cardiac arrhythmia. *Human Molecular Genetics*, 4(9), pp.1603–1607.

Wang, Q., Shen, J., Splawski, I., Atkinson, D., Li, Z., Robinson, J.L., Moss, A.J., Towbin, J. a. & Keating, M.T., 1995. SCN5A mutations associated with an inherited cardiac arrhythmia, long QT syndrome. *Cell*, 80(5), pp.805–811.

`

Ward, J.J., McGuffin, L.J., Bryson, K., Buxton, B.F. & Jones, D.T., 2004. The DISOPRED server for the prediction of protein disorder. *Bioinformatics*, 20(13), pp.2138–2139.

Weiss, J., Pyrski, M., Jacobi, E., Bufe, B., Willnecker, V., Schick, B., Zizzari, P., Gossage, S.J., Greer, C.A., Leinders-Zufall, T., Woods, C.G., Wood, J.N. & Zufall, F., 2011. Loss-of-function mutations in sodium channel Nav1.7 cause anosmia. *Nature*, 472(7342), pp.186–190.

Weiss, L.A., Escayg, A., Kearney, J.A., Trudeau, M., MacDonald, B.T., Mori, M., Reichert, J., Buxbaum, J.D. & Meisler, M.H., 2003. Sodium channels SCN1A, SCN2A and SCN3A in familial autism. *Molecular Psychiatry*, 8(2), pp.186–194.

Whitmore, L. & Wallace, B.A., 2004. DICHROWEB, an online server for protein secondary structure analyses from circular dichroism spectroscopic data. *Nucleic Acids Research*, 32, pp.W668–73.

Woodbury, D.J. & Hall, J.E., 1988. Role of channels in the fusion of vesicles with a planar bilayer. *Biophysical Journal*, 54(6), pp.1053–1063.

Woodbury, D.J. & Miller, C., 1990. Nystatin-induced liposome fusion. A versatile approach to ion channel reconstitution into planar bilayers. *Biophysical Journal*, 58(4), pp.833–839.

Wu, G., Bashir-Bello, N. & Freeland, S.J., 2006. The Synthetic Gene Designer: A flexible web platform to explore sequence manipulation for heterologous expression. *Protein Expression and Purification*, 47(2), pp.441–445.

Wu, Y., Yang, Y., Ye, S. & Jiang, Y., 2010. Structure of the gating ring from the human large-conductance Ca^{2+}-gated K^{+} channel. *Nature*, 466(7304), pp.393–397.

Xu, Y., Ramu, Y. & Lu, Z., 2008. Removal of phospho-head groups of membrane lipids immobilizes voltage sensors of K^{+} channels. *Nature*, 451(7180), pp.826–829.

Yang, Y., Wang, Y., Li, S., Xu, Z., Li, H., Ma, L., Fan, J., Bu, D., Liu, B., Fan, Z., Wu, G., Jin, J., Ding, B., Zhu, X. & Shen, Y., 2004. Mutations in SCN9A, encoding a sodium channel alpha subunit, in patients with primary erythermalgia. *Journal of Medical Genetics*, 41(3), pp.171–174.

Yarov-Yarovoy, V., DeCaen, P.G., Westenbroek, R.E., Pan, C.-Y., Scheuer, T., Baker, D. & Catterall, W.A., 2012. Structural basis for gating charge movement in the voltage sensor of a sodium channel. *Proceedings of the National Academy of Sciences of the United States of America*, 109(2), pp.E93–E102.

Yarov-Yarovoy, V.M., DeCaen, P., Scheuer, T., Baker, D. & Catterall, W.A., 2011. High-resolution structural modeling of voltage-dependent conformational changes in the voltage sensor of NaChBac. *Biophysical Journal*, 100(3), p.422a.

`

Ye, S., Li, Y., Chen, L. & Jiang, Y., 2006. Crystal structures of a ligand-free MthK gating ring: Insights into the ligand gating mechanism of K^+ channels. *Cell*, 126(6), pp.1161–1173.

Yuan, P., Leonetti, M.D., Hsiung, Y. & MacKinnon, R., 2011. Open structure of the Ca^{2+} gating ring in the high-conductance Ca2+-activated K^+ channel. *Nature*, 481(7379), pp.94–97.

Yuan, P., Leonetti, M.D., Pico, A.R., Hsiung, Y. & MacKinnon, R., 2010. Structure of the human BK channel Ca^{2+}-activation apparatus at 3.0 Å resolution. *Science*, 329(5988), pp.182–186.

Yue, L., Navarro, B., Ren, D., Ramos, A. & Clapham, D.E., 2002. The cation selectivity filter of the bacterial sodium channel, NaChBac. *The Journal of general physiology*, 120(6), pp.845–853.

Zhang, X., Ren, W., DeCaen, P., Yan, C., Tao, X., Tang, L., Wang, J., Hasegawa, K., Kumasaka, T., He, J., Wang, J., Clapham, D.E. & Yan, N., 2012. Crystal structure of an orthologue of the NaChBac voltage-gated sodium channel. *Nature*, 486(7401), pp.130–4.

Zhao, Y., Scheuer, T. & Catterall, W.A., 2004. Reversed voltage-dependent gating of a bacterial sodium channel with proline substitutions in the S6 transmembrane segment. *Proceedings of the National Academy of Sciences of the United States of America*, 101(51), pp.17873–17878.

Zhao, Y., Yarov-Yarovoy, V., Scheuer, T. & Catterall, W.A., 2004. A gating hinge in Na^+ channels: A molecular switch for electrical signaling. *Neuron*, 41(6), pp.859–865.

Zheng, H., Liu, W., Anderson, L.Y. & Jiang, Q.-X., 2011. Lipid-dependent gating of a voltage-gated potassium channel. *Nature Communications*, 2, p.250.

Zhou, Y., Morais-Cabral, J.H., Kaufman, A. & MacKinnon, R., 2001. Chemistry of ion coordination and hydration revealed by a K^+ channel-Fab complex at 2.0 Å resolution. *Nature*, 414(6859), pp.43–48.

`